Czech Technical University in Prague
Faculty of Mechanical Engineering
Department of Mechanics, Biomechanics and Mechatronics

PHENOMENOLOGICAL MODELING OF STRAIN-RANGE DEPENDENT CYCLIC HARDENING

by

Ing. Jaromír FUMFERA

A thesis submitted to
the Faculty of Mechanical Engineering, Czech Technical University in Prague,
in partial fulfillment of the requirements for the degree of Doctor.

Doctoral Study Programme: Mechanical Engineering
Study Field: Mechanics of Rigid and Deformable Bodies and Environment

Prague, July 2020

Thesis Supervisor:
doc. Ing. Miroslav Španiel, CSc.
Department of Mechanics, Biomechanics and Mechatronics
Faculty of Mechanical Engineering
Czech Technical University in Prague
Technická 4
166 07 Prague 6
Czech Republic

Abstract

This doctoral thesis deals with the phenomenological modeling of the material response of metals for large strain loading conditions. The main focus is on the phenomenon of material cyclic hardening and its dependency on the loading conditions, which was observed on the austenitic stainless steel 08Ch18N10T. The formulation of a metal plasticity constitutive model with a new cyclic hardening rule is proposed to enable correct simulation of the material response under large strain for uniaxial and torsional loading conditions. Material parameters of the presented model for 08Ch18N10T steel are identified. The constitutive model is implemented as a Fortran code in the commercial FE-software Abaqus as a material subroutine USDFLD. The extensive experimental program with 6 different specimen geometries made of 08Ch18N10T steel is presented. The results of FE simulations of all these cyclic tests are presented. A comparison of simulated and experimentally measured response shows the prediction capability of the presented material model.

Keywords:

cyclic plasticity, extremly low-cycle fatigue, strain-range dependent, finite element analysis

Abstrakt

Tato práce řeší fenomenologické modelování odezvy kovových materiálů při velkých deformacích. Zaměřuje se především na jev cyklického zpevnění materiálu a jeho závislosti na podmínkách zatěžování, což bylo pozorováno např. u austenitické nerezové oceli 08Ch18N10T. Je formulován konstitutivní model cyklické plasticity s novou definicí cyklického zpevnění materiálu, která umožňuje korektně simulovat odezvu materiálu při velkých deformacích pro jenoosé i torzní namáhání. Pro popsaný model jsou určeny materiálové parametry pro ocel 08Ch18N10T. Je popsána implementace modelu do komerčního konečně-prvkového softwaru Abaqus pomocí uživatelské subrutiny USDFLD napsané v programovacím jazyce Fortran. Jsou prezentovány výsledky zkoušek rozsáhlého experimentálního programu provedeného na 6 různých geometriích zkušebních vzorků z oceli 08Ch18N10T. Na srovnání výsledků experimentů a jejich simulací jsou demonstrovány predičkní schopnosti navrženého modelu.

Klíčová slova:

cyklická plasticita, extrémně nízko-cyklová únava, závislost na hladině deformace, metoda konečných prvků

Acknowledgements

I would like to express my gratitude to my supervisor, doc. Ing. Miroslav Španiel, CSc., who patiently lead my work throughout these seven long years.

I would like to acknowledge support from the Technology Agency of the Czech Republic, grant No. TA04020806, within which the experiments presented in this thesis were done.

I would like to thank doc. Ing. Radim Halama, PhD., who helped me to find the final direction of my work and with whom we made key publications for this thesis.

I would also like to thank Ing. Petr Tichý, PhD., for providing me the computational background for the simulations.

But most of all, I would like to thank my wife, Kate, for her endless love, support, and patience. One of the keys to success in doctoral studies is not to lose motivation, which was getting harder and harder every year. I have to admit that I lost my motivation and wanted to quit many times. But Kate always convinced me not to. Without her, I certainly wouldn't write these lines right now.

Declaration

I declare that my dissertation thesis titled *Phenomenological Modeling of Strain-Range Dependent Cyclic Hardening* and the work presented in it is the result of my own work, except as specified in the text.

Jaromír Fumfera
Prague, July 2020

Contents

List of Figures

List of Tables

Lists of Symbols

Symbol	Unit	Description
A	mm^2	cross-sectional area
A_R	MPa^{-1}	material parameter
A_∞	-	material parameter
A_ω	-	material parameter
b	-	material parameter
B_R	-	material parameter
B_∞	-	material parameter
B_ω	-	material parameter
C, C_i	MPa	material parameter
$\boldsymbol{C}$	MPa	elasticity constant matrix
$\boldsymbol{C}_{ep}$	MPa	elasto-plastic tangential stiffness matrix
C_R	MPa	material parameter
C_∞	-	material parameter
C_ω	-	material parameter
D_∞	-	material parameter
E	MPa	Young modulus
$Error$	%	error value in each cycle
f	MPa	plasticity function
F	N	force
F_a	N	amplitude of force
F_a^{exp}	N	experimental amplitude of force
F_a^{sim}	N	simulation amplitude of force
F_∞	-	material parameter
g, g_ϕ	MPa	scalar function representing memory surface
H	-	Heaviside function
I	-	unity tensor
K	-	Kronecker delta
K_{shear}	-	material parameter
$\boldsymbol{L}$, $\boldsymbol{L}_\phi$	-	unit tensor
M	-	total number of kinematic hardening rules
$MeanError$	%	mean error value
N	-	number of cycles
N_d	-	number of cycles until the force decreases
N_f	-	number of cycles to fracture

Symbol	Unit	Description
p	-	accumulated plastic strain
dp	-	accumulated plastic strain increment
Q	MPa	material parameter
R	MPa	isotropic variable
dR	MPa	isotropic variable increment
R_0	MPa	material parameter
R	mm	geometry radius
R_M, $R_{M\phi}$	MPa	memory surface size
R_M^{used}, $R_{M\phi}^{used}$	-	memory surface size used
$\dot{R}_M$	MPa^{-1}	memory surface size derivation
dR_M	MPa	increment of memory surface size
R_{M0}	MPa	limit size of memory surface
R_M^{min}, R_M^{max}	-	limit size of memory surface
$R_{M\omega}$	MPa	limit size of memory surface
$RMSE$	-	root mean square error
T_a^{exp}	Nm	experimental amplitude of torque
T_a^{sim}	Nm	simulation amplitude of torque
$TotalError$	%	total error value
Y	MPa	actual yield stress
$\boldsymbol{\alpha}$	MPa	back-stress tensor
$\boldsymbol{\alpha}'$	MPa	deviatoric part of back-stress tensor
$d\boldsymbol{\alpha}$	MPa	back-stress tensor increment
$\boldsymbol{\alpha}_{virt}$	MPa	virtual back-stress tensor
$d\boldsymbol{\alpha}_{virt}$	MPa	increment of virtual back-stress tensor
$\boldsymbol{\alpha}_{virt\phi}$	MPa	virtual backstress tensor
γ, γ_i	-	material parameter
γ_0	-	material parameter
γ_∞	-	material parameter
ϵ	-	strain
$d\boldsymbol{\epsilon}$	-	increment of strain tensor
ϵ_a	-	amplitude of strain
ϵ^e	-	elastic strain
$\boldsymbol{\epsilon}^e$	-	elastic strain tensor
ϵ^p	-	plastic strain
$d\boldsymbol{\epsilon^p}$	-	increment of plastic strain tensor
$d\lambda$	-	scalar multiplier
ν	-	Poisson ratio
σ	MPa	stress
$\boldsymbol{\sigma}$	MPa	stress tensor
$\boldsymbol{\sigma'}$	MPa	deviatoric stress tensor
$\sigma_{1,2,3}$	MPa	principal stresses 1,2,3
σ_a	MPa	amplitude of stress
$\sigma_{i,j}$	MPa	stress tensor component
σ_e	MPa	equivalent stress
σ_y	MPa	yield strength

Symbol	Unit	Description
ϕ	-	ϕ function, Marquis parameter
ϕ_0	-	initial value of Marquis parameter
ϕ_∞	-	Marquis parameter in the end of the fatigue life
ϕ_{cyc}	-	cyclic part of Marquis parameter
$d\phi_{cyc}$	-	increment of cyclic part of Marquis parameter
ω	-	ω function

Chapter 1

Introduction

Low-cycle fatigue (LCF) is a part of the fatigue phenomenon, where loading implies higher nominal stresses than the yield strength. The maximum number of cycles to failure for common steel-like materials is usually less than thousands of cycles [1].

The prediction of LCF on real mechanical components consists of two key features - modeling of material response and choosing the appropriate criterion of failure. The appropriate criterion of failure predicts when a failure occurs in a mechanical component depending on loading conditions and its history. Loading conditions are stress and strain tensor fields. In high-cycle fatigue (HCF), where elastic deformations are completely dominant (except very small areas at crack tips in the phase of crack propagation phase), the extended Hooke's law can determines the linear relationship between stress and strain and modeling of material response can be very accurate. The inputs for the failure criterion (stress and strain fields and their history) can be calculated or simulated very precisely and setting or choosing the right failure criterion is the key to the fatigue prediction.

In low-cycle fatigue, the yield strength is exceeded in a large volume of material, the plastic deformations occur and the relationship between stress and strain is no longer linear - on the contrary, it can be very complex. For the uniaxial loading, it can depends on a number of parameters like loading level applied, history of loading, and its sequence, the ratcheting or relaxation of material can occurs. For multiaxial loading, the whole phenomenon can become about the order more complex. Consequently, even if a perfect criterion for low-cycle fatigue exists, the fatigue prediction can fail if inputs for the criterion are incorrect because of badly determined material response modeling in general, mainly the badly determined relationship between stress and strain. This makes the modeling of material response at least as important as setting the appropriate failure criterion for the low-cycle fatigue.

In material response modeling in LCF, there are several main areas currently being researched, for example, LCF in combination with thermo-mechanical fatigue, ratcheting and creep, LCF combined with radiation, each field focusing as well on uniaxial and multiaxial loading conditions. Professor J.L. Chaboche summarized most of the prominent models dealing with these phenomena in his great review published in [2].

Low-cycle fatigue, where only few dozens of cycles to failure is reached [3, 4] is usually called extremely-low-cycle fatigue (ELCF) [5, 3, 4] or according to some

authors ultra-low-cycle fatigue [6] or very-low-cycle fatigue [7]. Between LCF and ELCF, there are some notable differences as has been nicely summarized in [3]:

- Different microstructure evolution in the ELCF regime due to extremely large strain amplitude and huge accumulated plastic strain. This was also observed by Ye in [8] for austenitic stainless steel SUS304-HP. "Microstructure observations using optical and transmission electron microscopy (TEM) revealed that with increasing total strain amplitudes, the slip band density increased and the dislocation structure changed from a planar array to a more cellular-like structure. Cyclic deformation-induced austenite/martensite transformation was observed at higher cyclic strain amplitudes. The change in microstructures during cycling is responsible for the fatigue hardening/softening behaviour of the material." [8]

- Different hardening/softening behavior - due to extremely short cyclic life, the proportion of stabilized cycles is smaller or there can be no stabilization at all and material just cyclically hardens/softens until the crack occurs.

Material models based on cyclically stable material, without correct reflection of cyclic hardening/softening, is unable to make an accurate prediction in the ELCF regime. This generates one more area currently being researched in conjunction with the LCF phenomenon, which is a material response for high-loading conditions, for example on the transition between LCF and ELCF regime.

For example, austenitic stainless steel 08Ch18N10T shows so called strain-range dependent cyclic hardening, as can be seen in Figure 1.1. For this material it means that it shows almost no cyclic hardening for low-loading conditions, a saturation of material response occurs under constant cyclic loading conditions and material is cyclically stable. But it shows continuous cyclic hardening with no saturation of material response under high-loading conditions. This phenomenon has to be somehow reflected in the material model if the fatigue prediction should give a satisfactory result.

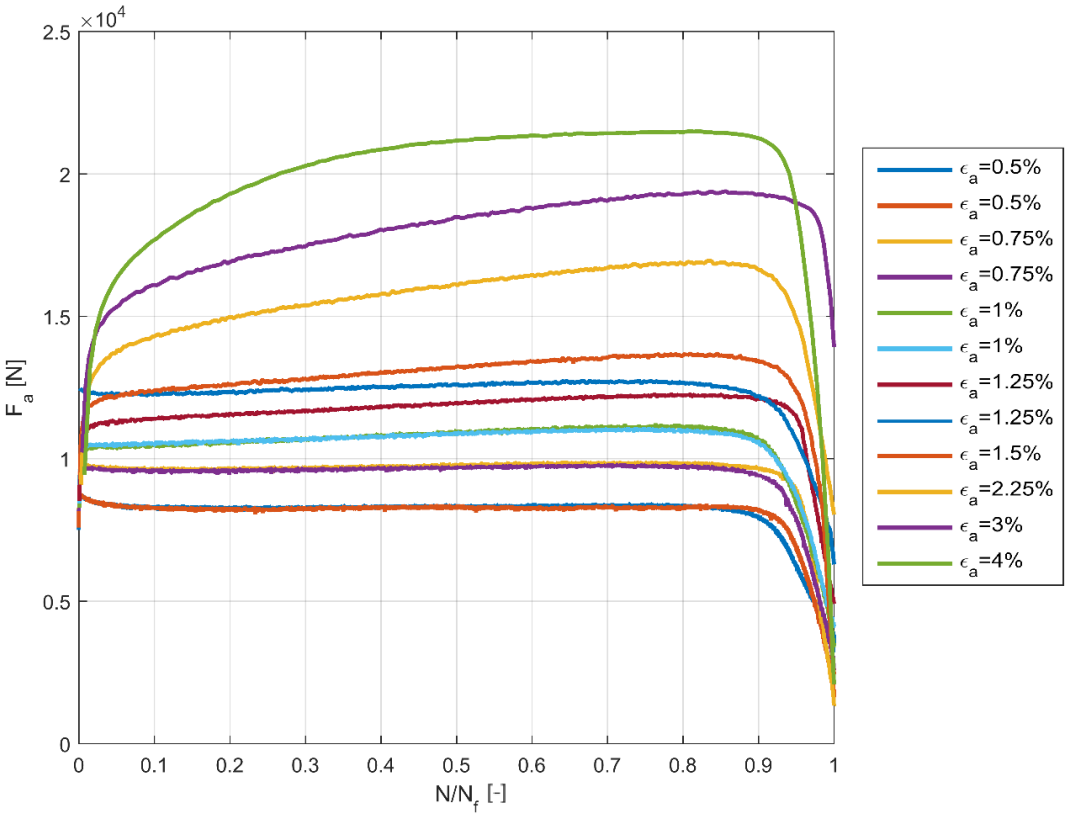

Figure 1.1: Illustration of strain-range dependent cyclic hardening of 08Ch18N10T stainless steel. [A5]

Chapter 2

State of the Art

2.1 Brief Introduction to the Theory of Plasticity

At first, it would be useful to review some generally know constitutive relationships and equations of continuum mechanics, specifically the elasto-plasticity. Some equations will be referred to in subsequent chapters of this thesis.

2.1.1 Plastic Strain

If the load is applied to common steel-like material, for example during the tensile test, the relationship between stress and strain can be simply illustrated by the static stress-strain curve, see Figure 2.1.1. If the stress applied to the specimen is lower than a yield strength σ_y, the total strain ϵ is only elastic and after unloading, the specimen returns to its initial shape. If the stress applied is higher than the yield strength, plastic strain appears and after unloading, the specimens remains permanently deformed and total strain is given as

$$\epsilon = \epsilon^e + \epsilon^p, \tag{2.1}$$

where ϵ^e is elastic strain and ϵ^p is plastic strain.

Using Hooke's law, it can be formulated as

$$\sigma = E\epsilon^e = E(\epsilon - \epsilon^p), \tag{2.2}$$

where σ is stress and E is the Young modulus.

This simple uniaxial problem can be generalized for multiaxial loading conditions and can be expressed using tensor notation as

$$\boldsymbol{\sigma} = \boldsymbol{C}\boldsymbol{\epsilon}^{\boldsymbol{e}}, \tag{2.3}$$

where $\boldsymbol{\sigma}$ is elastic stress tensor, $\boldsymbol{\epsilon}^{\boldsymbol{e}}$ is elastic strain tensor and $\boldsymbol{C}$ is the elastic stiffness matrix. For example, the stress tensor $\boldsymbol{\sigma}$ is formulated as

$$\boldsymbol{\sigma} = \begin{pmatrix} \sigma_{11} & \sigma_{12} & \sigma_{13} \\ \sigma_{21} & \sigma_{22} & \sigma_{23} \\ \sigma_{31} & \sigma_{32} & \sigma_{33} \end{pmatrix}. \tag{2.4}$$

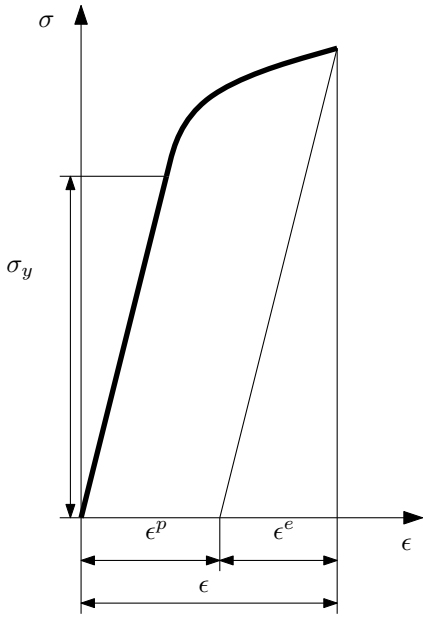

Figure 2.1: Static stress-strain curve.

Elastic strain tensor is defined analogously as the stress tensor.

When metals are exposed to plastic strain, they do not change in volume, which is called the condition of incompressibility and it can be expressed as

$$d\boldsymbol{\epsilon}_x^p + d\boldsymbol{\epsilon}_y^p + d\boldsymbol{\epsilon}_z^p = 0, \tag{2.5}$$

where symbol d stands for an increment and x, y and z are Cartesian coordinates.

For multiaxial loading, it is necessary to choose an appropriate criterion for determining the equivalent (sometimes also called effective) stress σ_e. For the plasticity of metals, the von Mises criterion is the most commonly used, mainly because of advantages when implementing in numerical calculations (eg. smoothness of the plasticity surface ensures finding a normal at any point) and can be written as

$$\sigma_e = \frac{1}{\sqrt{2}}[(\sigma_1 - \sigma_2)^2 + (\sigma_2 - \sigma_3)^2 + (\sigma_3 - \sigma_1)^2]^{1/2}, \tag{2.6}$$

where $\sigma_{1,2,3}$ are principal stresses, and in case of expression using general stress components σ_{ij}, $i, j = 1, 2, 3$ as

$$\sigma_e = \left[\frac{3}{2}(\sigma_{11}^2 + \sigma_{22}^2 + \sigma_{33}^2 + 2\sigma_{12}^2 + 2\sigma_{23}^2 + 2\sigma_{31}^2)\right]^{1/2}. \tag{2.7}$$

Stress tensor can be decomposed to a hydrostatic and deviatoric component defined as

$$\boldsymbol{\sigma} = \frac{1}{3}\mathrm{Tr}(\boldsymbol{\sigma})\boldsymbol{I} + \boldsymbol{\sigma}', \tag{2.8}$$

where $\boldsymbol{I}$ is the unity 3 x 3 matrix and the apostrophe symbol stands for deviatoric part. The von Mises stress can then be written as

$$\sigma_e = \left(\frac{3}{2}\boldsymbol{\sigma}' : \boldsymbol{\sigma}'\right)^{\frac{1}{2}}. \tag{2.9}$$

It should be pointed out that the colon used in the equation (2.9) denotes contracted tensor product. For example, for second order tensors $\boldsymbol{A}$ and $\boldsymbol{B}$,

$$\boldsymbol{A} : \boldsymbol{B} = \sum_{i=1}^{n} \sum_{j=1}^{n} A_{ij} B_{ij}. \tag{2.10}$$

An equivalent (sometimes also called effective) increment of plastic strain is defined as

$$dp = \left(\frac{2}{3} d\boldsymbol{\epsilon}^p : d\boldsymbol{\epsilon}^p \right)^{\frac{1}{2}} \simeq \left(\frac{2}{3} d\boldsymbol{\epsilon}' : d\boldsymbol{\epsilon}' \right)^{\frac{1}{2}}. \tag{2.11}$$

Here, it is worth remembering that plastic strain is also a deviator due to the condition of incompressibility.

2.1.2 Condition of Plasticity and Normal Hypothesis

For von Mises yield criterion, the plasticity function is in general defined as

$$f = \sigma_e - Y = \left(\frac{3}{2} \boldsymbol{\sigma}' : \boldsymbol{\sigma}' \right)^{\frac{1}{2}}, \tag{2.12}$$

where Y is actual yield stress. This function defines so-called yield surface, which for the von Mises criterion takes the form of a cylinder wall in the space of the principal stresses. The plasticity condition is then given as

$$f < 0 \text{ for elastic strain,} \tag{2.13}$$

$$f = 0 \text{ for plastic strain.} \tag{2.14}$$

Graphically, this condition can be interpreted so that the point representing the load and having the components representing the coordinates in the form of the principal stresses lies either within the yield surface, when the load is elastic, or on the yield surface if the load is plastic.

If the loading is plastic, the direction of plastic strain shall be determined. For metals it is generally accepted to use the so-called associated law of plasticity considering the normal hypothesis, ie that the resulting direction of plastic strain is perpendicular to the normal to the yield surface. This can be mathematically written as

$$d\boldsymbol{\epsilon}^p = d\lambda \frac{\partial f}{\partial \boldsymbol{\sigma}}. \tag{2.15}$$

Here, the symbols ∂ stands for partial derivative, $d\lambda$ is a lambda multiplier and it can be deduced that for the von Mises criterion it can be written that

$$\frac{\partial f}{\partial \boldsymbol{\sigma}} = \frac{\boldsymbol{\sigma}'}{\sigma_e}. \tag{2.16}$$

Furthermore, a relationship can be derived (and for metal materials and von Mises plasticity is generally accepted)

$$dp = d\lambda, \tag{2.17}$$

from which we can write the resulting relation for the calculation of plastic strain tensor as

$$d\boldsymbol{\epsilon}^p = \frac{3}{2} dp \frac{\boldsymbol{\sigma}'}{\sigma_e}. \tag{2.18}$$

2.1.3 The Consistency Condition

In the case of plastic loading, it is necessary to meet the so-called consistency condition, which can be interpreted so that the point representing the load must remain on the yield surface. This condition is given by the equation

$$f = \sigma_e - Y = 0. \tag{2.19}$$

In case of material hardening or softening (the size of the yield surface or its shape changes), it is necessary to consider the dependence of the function f on some cumulative quantity, most often by accumulated plastic strain p, ie

$$f = \sigma_e(\boldsymbol{\sigma}) - Y(p) = 0. \tag{2.20}$$

This relationship can be expressed by an incremental form and modified into a general expression

$$d\lambda = \frac{\frac{\partial f}{\partial \boldsymbol{\sigma}} \cdot \boldsymbol{C} \cdot d\boldsymbol{\epsilon}}{\frac{\partial f}{\partial \boldsymbol{\sigma}} \cdot \boldsymbol{C} \cdot \frac{\partial f}{\partial \boldsymbol{\sigma}} - \frac{\partial f}{\partial p} \left(\frac{2}{3} \frac{\partial f}{\partial \boldsymbol{\sigma}} \frac{\partial f}{\partial \boldsymbol{\sigma}} \right)^{\frac{1}{2}}}, \tag{2.21}$$

which can be further customized as

$$d\boldsymbol{\sigma} = \left(\boldsymbol{C} - \boldsymbol{C} \frac{\partial f}{\partial \boldsymbol{\sigma}} \cdot \frac{\frac{\partial f}{\partial \boldsymbol{\sigma}} \cdot \boldsymbol{C} \cdot d\boldsymbol{\epsilon}}{\frac{\partial f}{\partial \boldsymbol{\sigma}} \cdot \boldsymbol{C} \cdot \frac{\partial f}{\partial \boldsymbol{\sigma}} - \frac{\partial f}{\partial p} \left(\frac{2}{3} \frac{\partial f}{\partial \boldsymbol{\sigma}} \frac{\partial f}{\partial \boldsymbol{\sigma}} \right)^{\frac{1}{2}}} \right) d\boldsymbol{\epsilon} = \boldsymbol{C}_{ep} d\boldsymbol{\epsilon}, \tag{2.22}$$

where $\boldsymbol{C}_{ep}$ is an elasto-plastic tangential stiffness matrix (sometimes called Jacobian) that determines the relationship between stress and strain [9]. However, it is not constant and depends on the current material state and load history. It is also worth noting that the consistency condition is necessary to resolve constitutive relations.

2.1.4 Cyclic Stress-Strain Curve

If the common steel-like material is exposed to the uniaxial cyclic loading, the response of the material changes due to changes in microstructure. The intensity of these changes usually decreases with increasing number of cycles and after that, the response stabilizes [10]. The stabilized state can be illustrated by the hysteresis loop. The cyclic stress-strain curve (CSSC) is created by interposing the vertices of hysteresis loops for different amplitudes of strain ϵ_a, see Figure 2.1.4 for illustration.

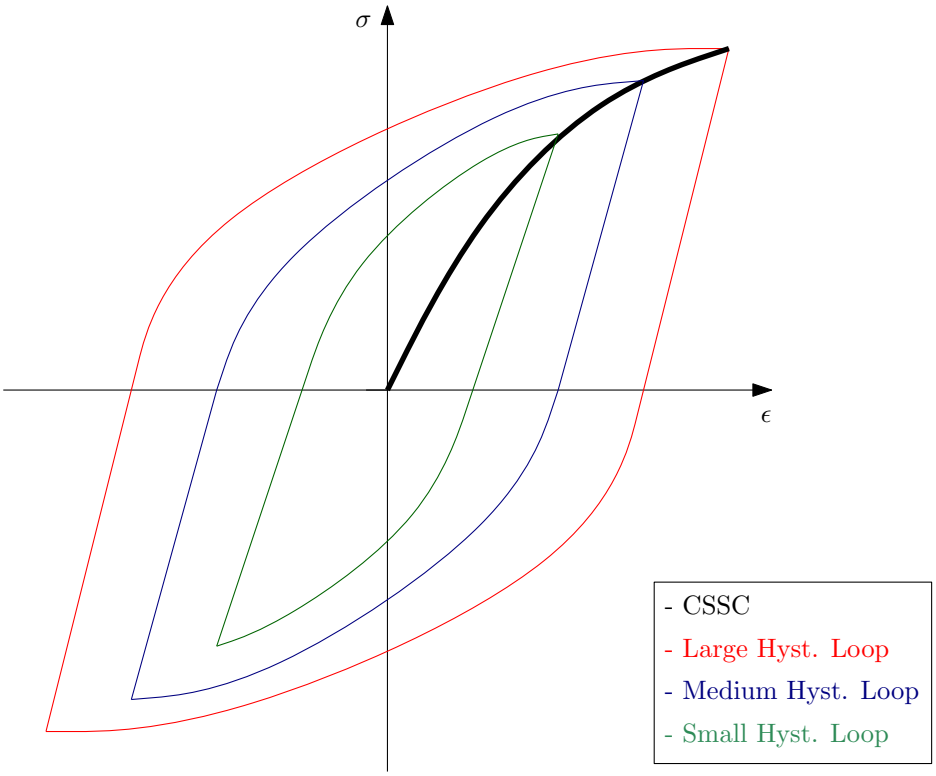

Figure 2.2: Illustration of cyclic stress-strain curve.

2.1.5 Isotropic Hardening

Most materials show material hardening under plastic loading conditions. Usually, the hardening function is mathematically written as a function of the accumulated plastic strain p. In the case of isotropic hardening, the plasticity area expands and therefore Y changes as a function of p and the plasticity condition can be written as

$$f = \sigma_e - Y(p) = \sigma_e - (\sigma_y + R(p)) \,, \tag{2.23}$$

where σ_y is yield strength and $R(p)$ is the isotropic variable. $R(p)$ can take various forms, for example, in commercial FE software Abaqus 6.14, the non-linear isotropic hardening model is defined as

$$R(p) = Q(1 - e^{-bp}), \tag{2.24}$$

where Q and b are material parameters [11].

The illustration of yield surface expansion in principal stress space for isotropic hardening model is shown in the Figure 2.3. The index 0 denotes the initial state and the actual state is without index.

2.1.6 Kinematic Hardening

The isotropic hardening model is sufficient and widely used in the modeling of monotonic loading, for example, ductile fracture. However, it is not able to capture

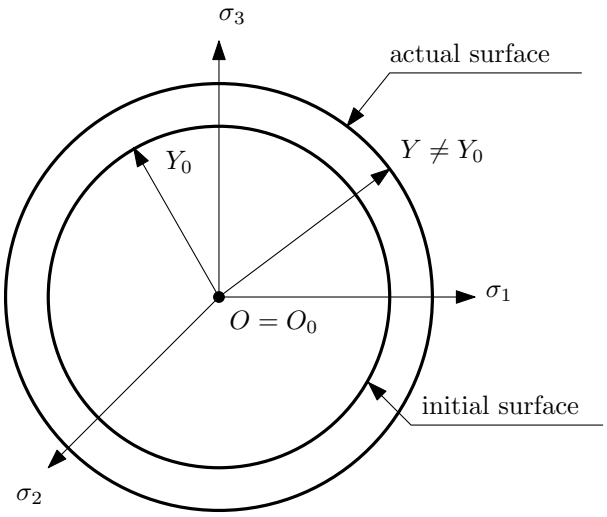

Figure 2.3: Isotropic hardening.

the Bauchinger effect during reversal loading. This is possible with the kinematic hardening model which describes the displacement of the yield surface in the space of the principal stresses. Its size remains the same in the case of a pure kinematic hardening model, ie $dY = 0$.

The plasticity condition from the equation (2.12) then takes form

$$f = \sigma_e - Y = \left(\frac{3}{2}(\boldsymbol{\sigma}' - \boldsymbol{\alpha}') : (\boldsymbol{\sigma}' - \boldsymbol{\alpha}')\right)^{\frac{1}{2}} - Y = 0, \tag{2.25}$$

where $\boldsymbol{\alpha}$ is the so-called back-stress, which is a tensor describing the position of the center of the yield surface relative to the origin of the coordinate system in the space of the principal stresses.

The simplest model that attempted to describe the kinematic hardening of the material is Prager's linear kinematic hardening model [12], where the back-stress increment is a linear function of the plastic strain tensor

$$d\boldsymbol{\alpha} = \frac{2}{3} C d\boldsymbol{\epsilon}^p, \tag{2.26}$$

where C is a material parameter. Armstrong-Frederick model [13] already considers nonlinear hardening under plastic loading, where the increment of the back-stress is given by the equation

$$d\boldsymbol{\alpha} = \frac{2}{3} C d\boldsymbol{\epsilon}^p - \gamma \boldsymbol{\alpha} dp, \tag{2.27}$$

where γ is material parameter.

The simple non-linear kinematic hardening model can be further upgraded. For example Chaboche [14] superpose the back-stress from m parts as

$$\boldsymbol{\alpha} = \sum_{i}^{m} \boldsymbol{\alpha}_i, \tag{2.28}$$

$$d\boldsymbol{\alpha}_i = \frac{2}{3} C_i d\boldsymbol{\epsilon}^p - \gamma_i \boldsymbol{\alpha} dp, \tag{2.29}$$

where m is usually equal to 2 or 3. The back-stress component i is calculated in the same way as in the default Armstrong-Frederick model [13], and with proper selection of C_i and γ_i, it allows a much better description of the steady-state hysteresis loop shape. The extension of the kinematic model by isotropic hardening, given by the equation (2.34), makes it possible to capture the pre-saturation phase, ie the transition from the initial cycles to the saturated cycles. It is not necessary to model the cyclic hardening using only the isotropic hardening model. Marquis [15] came with a modification of the Armstrong-Frederick based models using an evolutionary rule for the kinematic hardening for its non-linear term as

$$d\boldsymbol{\alpha} = \frac{2}{3} C \; d\boldsymbol{\epsilon}^p - \gamma(p) \boldsymbol{\alpha} dp \tag{2.30}$$

$$\gamma(p) = \gamma_\infty - (\gamma_\infty - \gamma_0)\, e^{-\omega p}, \tag{2.31}$$

where γ_0 is the initial value of γ, which gradually turns into a stabilized value of γ_∞, ω is the stabilization rate, and $p = \sum dp$, which can also be overridden assuming $\gamma(p) = \phi \cdot \gamma_\infty$ into shape

$$d\boldsymbol{\alpha} = \frac{2}{3} C d\boldsymbol{\epsilon}^p - \phi \gamma_\infty \boldsymbol{\alpha} dp, \tag{2.32}$$

where

$$\phi = 1 - \left(1 - \frac{\gamma_0}{\gamma_\infty}\right) e^{-\omega p} \tag{2.33}$$

and is called Marquis parameter [10] or the ϕ function. Various forms of the ϕ function are often used to modify a non-linear kinematic hardening rule.

The illustration of the yield surface translation in principal stress space for kinematic hardening model is shown in Figure 2.4, where $\boldsymbol{\alpha}$ denotes the back-stress, index 0 denotes the initial state, and the actual state is without index.

2.1.7 Combined Hardening Model

Although a saturated hysteresis loop can be modeled for a variety of materials only with the kinematic hardening model, a combination of the kinematic hardening model and the isotropic hardening model must be used to capture the process before saturation or cyclic hardening in general. Thus, the yield surface can shift in the space of the principal stresses and it can also change its size. The plasticity condition then has the form

$$f = \left(\frac{3}{2}(\boldsymbol{\sigma}' - \boldsymbol{\alpha}') : (\boldsymbol{\sigma}' - \boldsymbol{\alpha}')\right)^{\frac{1}{2}} - \sigma_y + R(p). \tag{2.34}$$

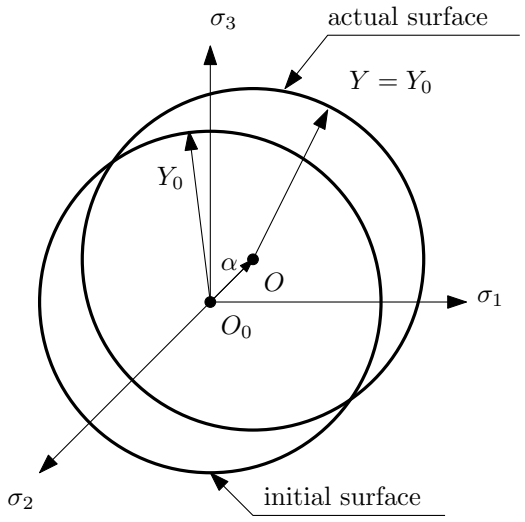

Figure 2.4: Kinematic hardening.

The illustration of yield surface expansion and translation for combined hardening model is shown in Figure 2.5.

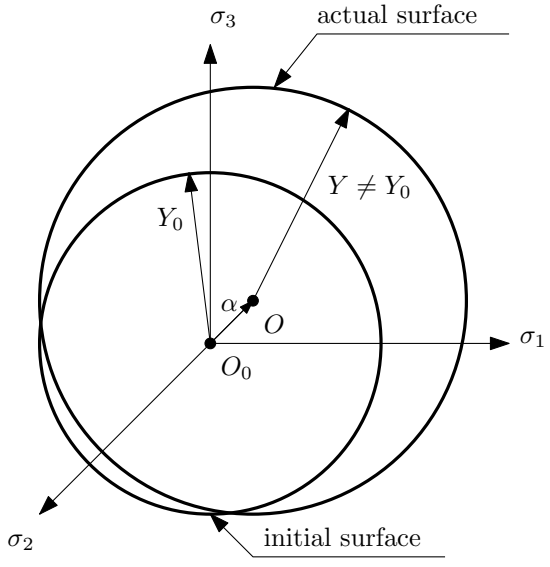

Figure 2.5: Combined hardening.

2.1.8 Strain-Range Dependent Cyclic Hardening

Some construction materials shows saturation of the material response to a certain limited load range under cyclic loading. For example, the response for a strain controlled loading at a constant amplitude of the total strain stabilizes after a few cycles and hysteresis loops of saturated cycles differ only slightly. In this case, a simple combination of kinematic hardening together with isotropic hardening is sufficient and as it is now quite commonly implemented in commercial FE software, such as Abaqus or ANSYS.

E.g. the austenitic stainless steel 08Ch18N10T shows a saturation of the cyclic response up to a load level of approximately $\epsilon_a = 0.75\%$ (see Figure 1.1). At higher load levels, however, the material cyclic hardening appears, and, for example, at a load level of $\epsilon_a = 3\%$, the saturation of material response does not appear.

The first attempt to include the influence of the load amplitude into constitutive relations came from Chaboche in [14] with the so-called *Memory Surface* concept. It is an extension of the basic single-surface model by the memory surface model. In this particular model, the memory surface is defined in the principal strain space, taking into account the influence of the achieved load level during loading. The cyclic hardening is then a function of the size of the memory surface and it is realized by means of an isotropic hardening mechanism. Ohno [16] added a so-called non-hardening region, an area in which isotropic hardening does not apply and thus there is no cyclical hardening of the material. Above this area (ie for higher load levels) isotropic hardening is applied and the material cyclically hardens.

In general, the memory surface can change its position and size depending on the achieved load level in a similar way as the yield surface. Its size may vary (increase or decrease) depending on the load achieved and its history. E.g. its current size can then be a parameter of the functions describing the dependence of cyclic hardening on the load level.

[17] points out that the isotropic hardening mechanism can simulate the amplitude values of cyclic hardening, but it is not sufficient to describe the shape of the hysteresis loop. For this reason, it is necessary to extend the kinematic model of cyclic hardening using the concept of memory surface. [18] mentions the possibility to modify the C parameter in the equation (2.29), but it is much more common to modify the γ parameter using differently defined ϕ function in equation (2.32), see eg. [19], [17] or [20].

The memory surface does not need to be defined in the strain space, but it can be also defined in the deviatoric stress space. This approach can be found, for example, in [21]. The introduction of the memory surface in the deviatoric stress space is mainly advantageous due to the effort to better predict ratcheting and disproportionate hardening.

Adjusting the plasticity equations (2.32) and (2.34), taking into account the load level and using the memory surface concept, the plasticity function can be written as:

$$f = \left(\frac{3}{2}\left(\boldsymbol{\sigma}' - \boldsymbol{\alpha}'(p, R_M)\right) : \left(\boldsymbol{\sigma}' - \boldsymbol{\alpha}'(p, R_M)\right)\right)^{\frac{1}{2}} - \sigma_y + R(p, R_M), \quad (2.35)$$

$$d\boldsymbol{\alpha} = \frac{2}{3}Cd\boldsymbol{\epsilon}^p - \phi(p, R_M) \cdot \gamma_\infty \boldsymbol{\alpha} dp, \tag{2.36}$$

where R_M is the size of the memory surface.

2.2 Some Important Publications Related to Strain-Range Dependent Cyclic Plasticity

Most of this chapter is directly cited from the article [A1].

"Austenitic stainless steel 08Ch18N10T is a chrome-nickel steel that is stabilized by titanium. This steel is widely used in the nuclear industry for piping systems and reactor internals in the Russian-designed VVER water-water power reactors for nuclear power plants (NPP). Reactor internals are the part of an NPP that provides support, guidance and protection for the reactor core and for the control elements. The block of guided tubes, the core barrel, the core barrel bottom and the core shroud are some of the internal components that are exposed to very harsh operating regimes. The operating regime, e.g. heating and shut-downs, has a significant influence on the service life of the components. The vibration and pressure pulsation of the water pumps also have to be taken into account. These regimes expose the reactor internals to cyclic loading.

In practice, cyclic loading of structural parts can lead to the formation and propagation of cracks through the process referred to as fatigue. In all areas of industry, the operational safety of machinery depends on an appropriate design process, which includes an analysis of all possible critical states. In the low-cycle fatigue domain, seismic analysis and the simulation of operational tests of the piping systems of NPPs may be used as an example. In these cases, it is crucial to have an accurate description of the stress-strain behavior of the material that is being considered.

Phenomenological models [22] are the most widely-used models in practical applications. Their goal is to provide as accurate as possible description of the stress-strain behavior of the material, which is found on the basis of experiments [23]. The stress-strain behavior of structural materials under cyclic loading is very diverse, and a case-by-case approach is required [24].

The most progressive group of cyclic plasticity models, which are commonly encountered in commercial finite element method programs, are single yield surface models based on differential equations. Their development is closely linked to the creation of a nonlinear kinematic hardening rule with a memory term, introduced by Armstrong and Frederick in 1966 for the evolution of back-stress [13], and the discovery by Chaboche [14] of the vast possibilities offered by the superposition of several back-stress parts.

Developments in the field of non-linear kinematic hardening rules were mapped in detail in [22]. In the current paper, we will mention only the most important theories. In 1993, Ohno and Wang [25] proposed two nonlinear kinematic hardening rules. For both models, it is considered that each part of the back-stress has a certain critical state of dynamic recovery. Ohno-Wang Model I leads to plastic shakedown under uniaxial loading with a nonzero mean axial stress value (no ratch-

eting), and under multiaxial loading it gives lower accumulated plastic strain values than have been observed in experiments. The memory term of Ohno-Wang Model II [25] is partially active before reaching the critical state of dynamic recovery, which allows a good prediction of ratcheting under uniaxial loading and also under multiaxial loading. The Abdel-Karim-Ohno nonlinear kinematic hardening rule [26] was published in 2000. This rule is in fact a superposition of the Ohno-Wang I and Armstrong-Frederick rules. The proposed model was designed to predict the behavior of materials that exhibit a constant increment of plastic strain during ratcheting. Other modifications to this kinematic hardening rule, leading to a better prediction of uniaxial ratcheting and also multiaxial ratcheting, were proposed by one of the authors of paper [27]. In order to capture the additional effects of cyclic plasticity, the concept of kinematic and isotropic hardening has been further modified. Basically, the available theories can be divided into two approaches. The first approach is related to the actual distortion of the yield surface [28, 29, 30], while the second approach is related to the memory effect of the material [14], [16]. The effect of cyclic hardening as a function of the size of the strain amplitude is usually assumed in the second approach.

The first comprehensive model of cyclic plasticity with a memory surface was proposed by Chaboche and co-authors in [14]. Chaboche's memory surface was established in the principal plastic strain space and captures the influence of plastic strain amplitude and also the mean value of the plastic strain. The memory surface is associated with a non-hardening strain region in a material point, as is explained by Ohno [16] for the general case of variable amplitude loading. Memory surfaces established in the stress space have also been developed. Their main advantage is that they enable more accurate ratcheting strain prediction to be achieved, as presented by Jiang and Sehitoglu in their robust cyclic plasticity model [21].

It should be mentioned that both of these memory surface concepts lead to an increase in the number of material parameters and in the number of evolution equations, which complicates their use in engineering practice.

The original application of the memory surface, introduced by Jiang and Sehitoglu, was extended by some authors of the present paper to capture the memory effect of ST52 material, in [31]. Uniaxial experiments indicate that, in the case of a cyclically softening/hardening material, larger strain amplitudes cause a significant change in the shape of the hysteresis loops. Only a very small number of researchers in the field of cyclic plasticity have investigated the influence of strain amplitude on the cyclic hardening effect. Good agreement with experiments has been achieved in the case of steel SS304 [32], but at the cost of defining more than 70 material parameters.

Some of the material models have been used to capture cyclic material behavior. To describe the cyclic behavior of SAE 4150 martensitic steel [33], Schäfer et al considered three kinematic hardening models, i.e. the Chaboche [14], Armstrong Frederick [13] and Ohno-Wang [25] models. They used these kinematic approaches to simulate the micromechanical behavior of the selected material. Moeini et al [34] used the Chaboche model [14] to predict the low-cyclic behavior of dual-phase steel. Selected kinematic hardening model provides good agreement with experimental results. Msolli used the unified viscoplastic model [35] developed by Chaboche

when modeling the elastoviscoplastic behavior of JLF-1 steel at higher temperatures (400 °C and 600 °C). In this study, the Chaboche model was slightly modified to capture cyclic hardening followed by cyclic softening. The material model also falls into the category of coupled damage models. The material model shows good agreement with the experimental results. The effect of torsional pre-strain on low-cycle fatigue performance of SS304 was studied in [36]. Kang et al [37], used the visco-plastic constitutive model with the extended Abdel-Karim-Ohno nonlinear kinematic hardening rule with some temperature-dependent terms. This constitutive model was verified on uniaxial and non-proportional multiaxial ratcheting experimental results at room temperature and at elevated temperatures. Another visco-plastic constitutive model was used by Kang, Gao and Yang [38] in their study to simulate uniaxial and multiaxial ratcheting of cyclically hardening materials. They used the Ohno-Wang kinematic hardening rule with critical state of dynamic recovery. The effect of loading history was also considered by introducing a fading memorization function for the maximum plastic strain amplitude." [A1]

Of recently published works, Halama et al [A1] developed a new cyclic plasticity model suitable for predicting strain-range dependent cyclic hardening of austenitic steels. This model uses the idea of memory surface defined in the principal stress space established by Jiang and Sehitoglu [21], the kinematic hardening rule based on Chaboche model, and takes into account a new internal variable referred to as virtual back-stress, corresponding to a cyclically stable material. The model is capable of capturing the cyclic hardening with strain-range dependency as for example Kang advanced model [32], but with a considerably lower number of material parameters, as has been demonstrated in [A1].

2.3 Material Parameters Identification

Young modulus E, Poisson ration ν and yield strength σ_y are usually determined from the tensile test according to [39] or other equivalent standard. Material parameters of the Chaboche model C_i and γ_i from (2.29) can be determined from the cyclic stress-strain curve or from the large hysteresis loop [40]. It is commonly used for fitting hysteresis loop parameters, as can be seen for example in [40, 10, 41, 42, 20, 22, A1].

In [41], Bari and Hassan propose to use a simplified analytical relation defining the loading part of the stabilized hysteresis loop from the stress – plastic strain diagram as

$$\sigma_x = \sigma_y + \frac{C_1}{\gamma_1}\left(1 - 2e^{-\gamma_1(\epsilon^p - \epsilon^{pL}))}\right) + \frac{C_2}{\gamma_2}\left(1 - 2e^{-\gamma_2(\epsilon^p - \epsilon^{pL}))}\right) + C_3\epsilon_p, \qquad (2.37)$$

where σ_x is the axial stress, ϵ^{pL} is the plastic strain corresponding to the compressive strain amplitude, it is assumed $\gamma_3 = 0$. A least square method is usually used for fitting material parameters C_i and γ_i [22].

For strain-range dependent hardening materials, material parameters fitted from large hysteresis loop usually does not predict well the shape of smaller hysteresis loops. This is usually corrected by determining the Marquis parameter ϕ and

isotropic variable R as a function of accumulated plastic strain p and memory surface R_M [A1].

The reflection of the static strain curve, while simulating for example the monotonic tensile test, is made by combination of (2.37) and (2.36) into expression

$$\sigma = \sigma_y + \frac{C_1}{\gamma_1\phi_0}\left(1 - 2e^{-\gamma_1\phi_0\epsilon^p}\right) + \frac{C_2}{\gamma_2\phi_0}\left(1 - 2e^{-\gamma_2\phi_0\epsilon^p}\right) + C_3\epsilon_p, \tag{2.38}$$

where ϕ_0 is initial value of Marquis parameter and it is a constant.

For fitting the cyclic stress-strain curve, the relation between σ_a and ϵ_a^p can be expressed as [40]

$$\sigma_a = \sigma_y + \frac{C_1}{\gamma_1}\tanh(\gamma_1\epsilon_a^p) + \frac{C_2}{\gamma_2}\tanh(\gamma_2\epsilon_a^p) + C_3\epsilon_a^p. \tag{2.39}$$

Combining with equations (2.39) and (2.36) it can be written as

$$\sigma_a = Y + \frac{C_1}{\gamma_1\phi}\tanh(\gamma_1\phi\epsilon_a^p) + \frac{C_2}{\gamma_2\phi}\tanh(\gamma_2\phi\epsilon_a^p) + C_3\epsilon_a^p. \tag{2.40}$$

Here, $\phi = \phi(p, R_M)$ and isotropic variable $Y = Y(p, R_M)$ are functions and can be fitted from this equation.

Chapter 3

Motivation

In the framework of the grant project of Czech Technological Agency TA04020806, on which the author participates, extensive experimental research program of the LCF of austenitic stainless steel 08Ch18N10T has been done. This material is used in the internals of VVER pressurized water nuclear reactors and shows significant strain-range dependent cyclic hardening, as has been demonstrated in Figure 1.1.

The illustration of austenitic stainless steel 08Ch18N10T significant strain-range dependent cyclic hardening can be seen in Figure 1.1. The most advanced suitable model, that can predict this behavior, while still holding back the number of material parameters, turns out to model of cyclic plasticity developed by Halama et al [A1]. In this thesis, it will continue to be referred to as the original model.

The material parameters of this model for 08Ch18N10T were identified by the author and published in [A1]. The model shows excellent prediction capability for uniaxial loading conditions, as can be seen for illustration on the following Figures 3.1 and 3.2, where the amplitude of force F_a of the experiments is compared with results of FE simulations using the original model with an accetable error up to 5 %.

The model also predicts well the response of notched specimens on all three notched geometries as can be seen in Figures 3.3, 3.4, 3.5, 3.6, 3.7 and 3.8. The stress-strain field in notched specimens is no longer uniaxial, but the axial component of stress and strain is still dominant.

Under torsional loading conditions, the original model does predict the material response well only for lower loading levels as can be seen, for example, in Figure 3.9 for $\epsilon_a = 1.5\,\%$. However, the original model (as, of course, it's predecessors) over-predicts cyclic hardening of 08Ch18N10T steel for higher loading levels [A9]. This can be seen, for example, in Figure 3.10 for $\epsilon_a = 2.5\,\%$, where the over-prediction is most evident.

In order to minimize the observed over-prediction under torsional loading conditions, a new formulation of material model is needed.

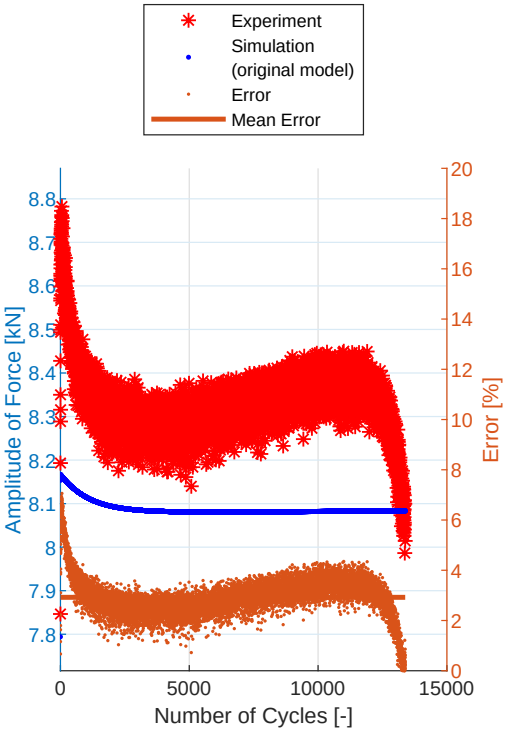

Figure 3.1: Experiment vs. simulation of the original model, specimen E9-1. [A1]

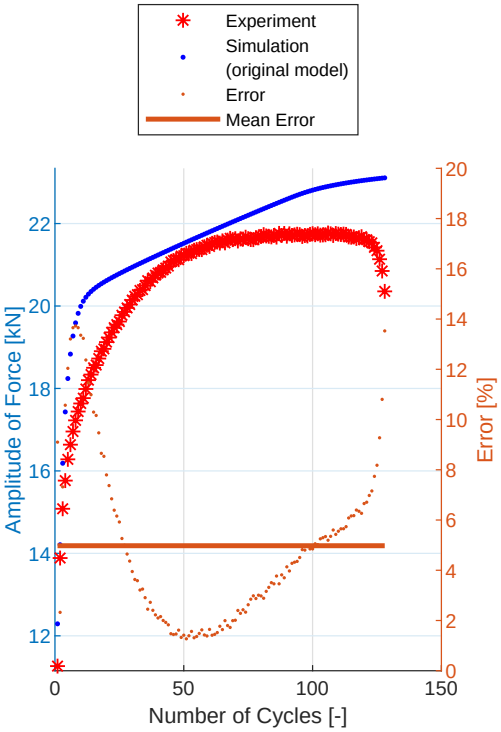

Figure 3.2: Experiment vs. simulation of the original model, specimen E9-17. [A1]

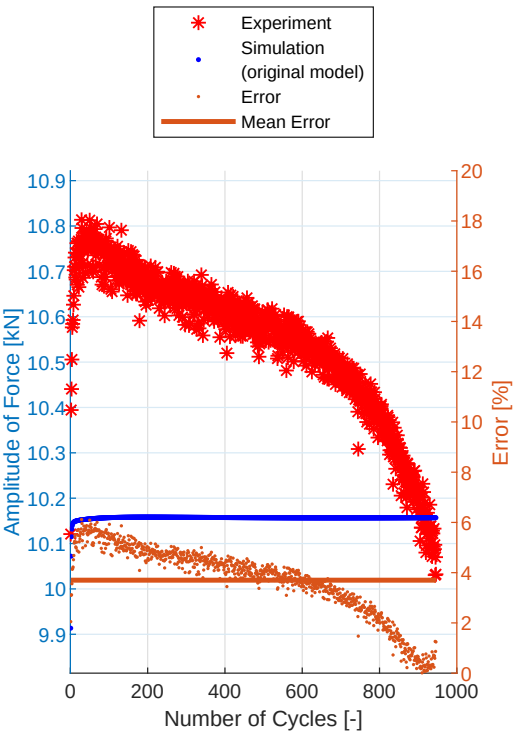

Figure 3.3: Experiment vs. simulation of the original model, specimen R1.2-2.

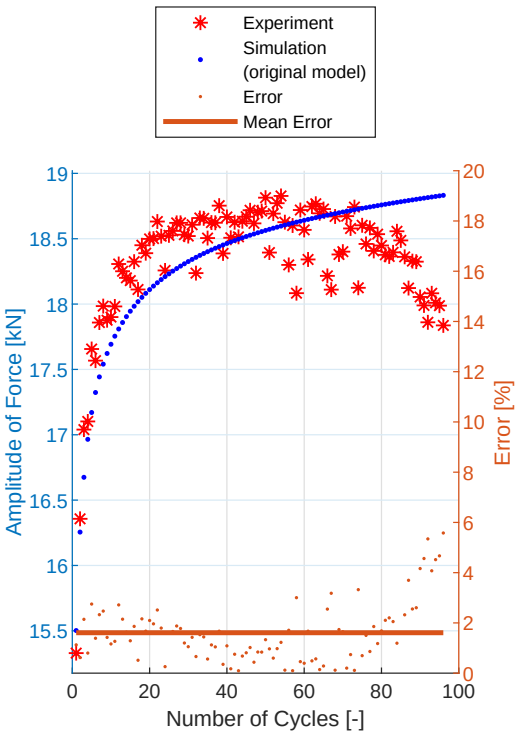

Figure 3.4: Experiment vs. simulation of the original model, specimen R1.2-17.

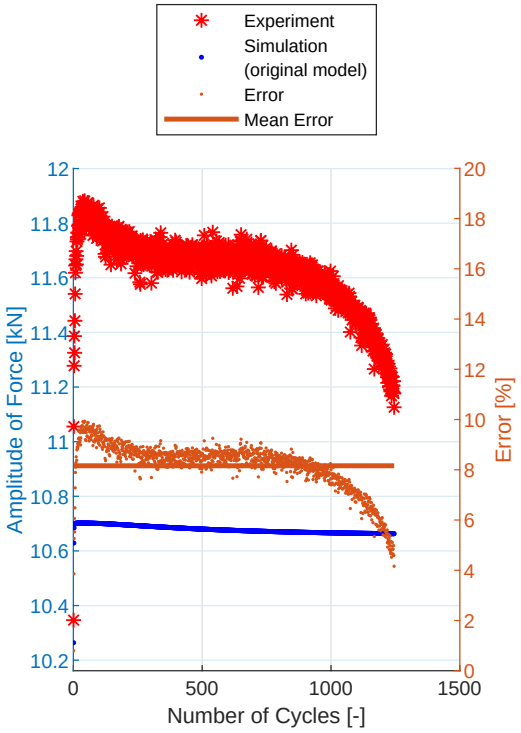

Figure 3.5: Experiment vs. simulation of the original model, specimen R2.5-2.

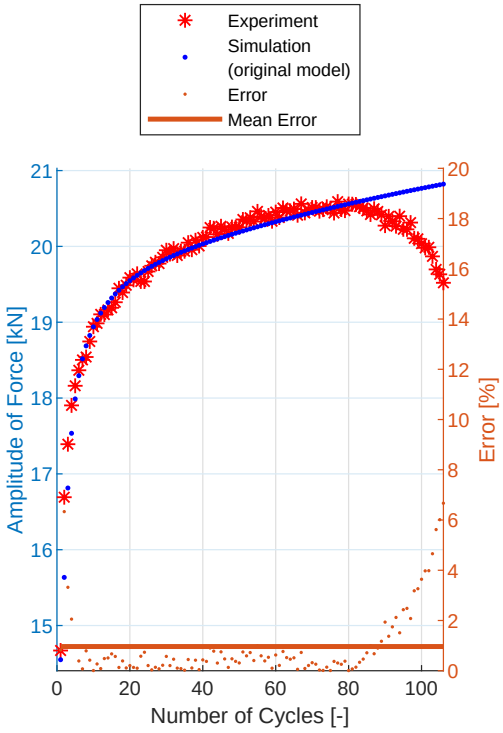

Figure 3.6: Experiment vs. simulation of the original model, specimen R2.5-20.

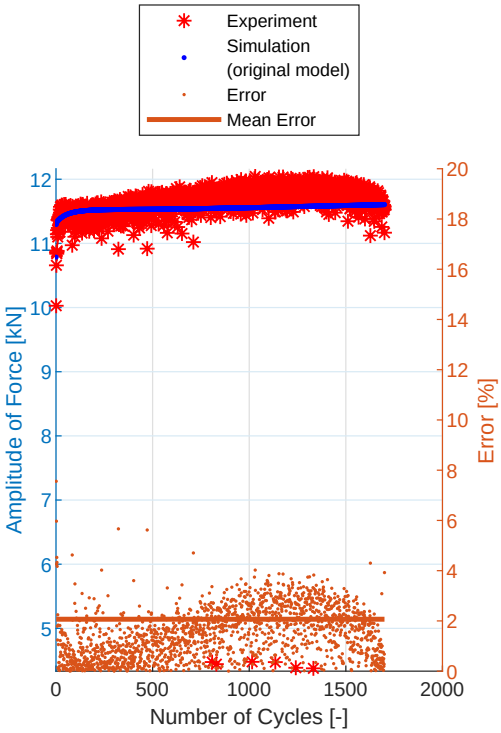

Figure 3.7: Experiment vs. simulation of the original model, specimen R5-2.

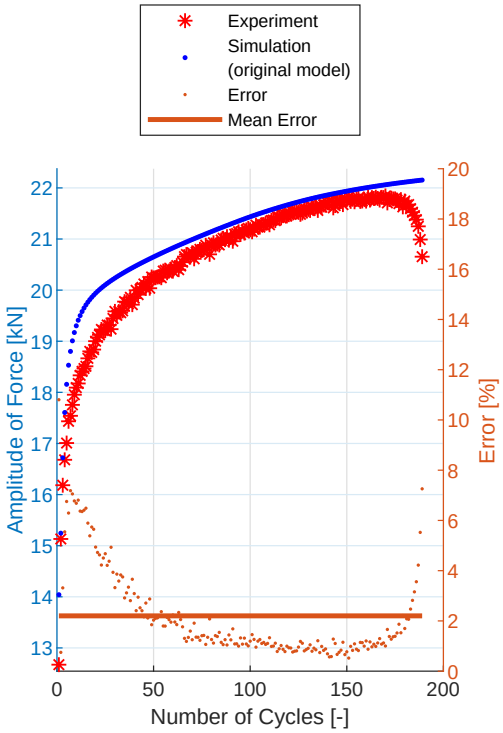

Figure 3.8: Experiment vs. simulation of the original model, specimen R5-23.

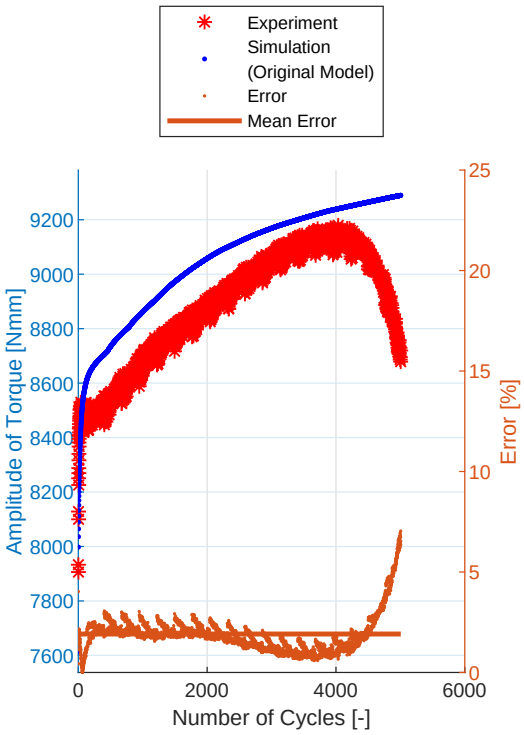

Figure 3.9: Experiment and simulation of the original model, specimen NT-1. [A9]

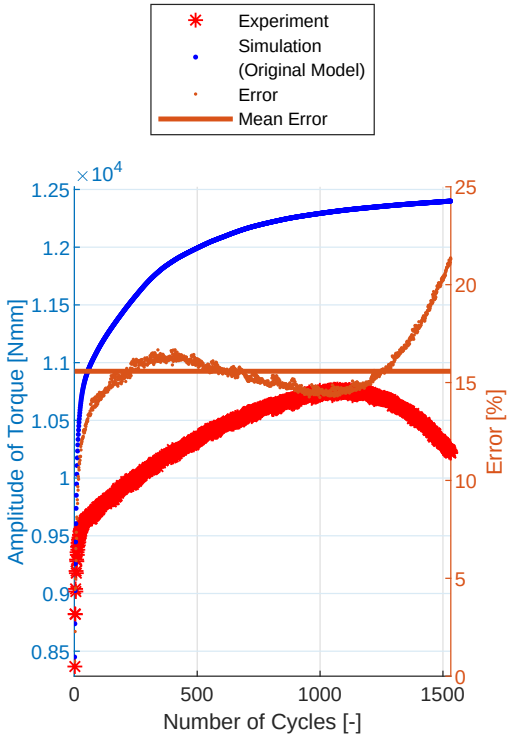

Figure 3.10: Experiment and simulation of the original model, specimen NT-6. [A9]

Chapter 4

Objectives of the Doctoral Thesis

From the literature review presented in Chapter 2, it was found that there is no published cyclic plasticity material model that is capable of good prediction of strain-range dependent cyclic hardening of 08Ch18N10T steel under uniaxial and torsional loading conditions, as has been presented in Chapter 3.

The original model [A1], which has been used for the illustration in Chapter 3, has been chosen by the author as the model to start with. It is one of the most recent and most advanced material model that deals with strain-range dependent cyclic hardening of material and it still uses a minimalistic number of material parameters at the same time.

The main objective of the thesis is to propose a new formulation of a constitutive model that can predict the response of the material for uniaxial loading conditions as well as for the torsional loading conditions. The key steps to achieve this goal are:

1. **The proposition of modification:**

   Modifications of the original model will be proposed and new constitutive relations will be described.

2. **Calibration of material parameters:**

   The material parameters of the newly proposed model will be identified for 08Ch18N10T austenitic stainless steel. The identification process will be described step by step, the new set of material parameters for 08Ch18N10T steel will be presented.

3. **Implementation into FE:**

   Building FE models of specimens, that have been used for experiments (presented in Chapter 3) will be described. The newly proposed model will be implemented into commercial FE software Abaqus as a user subroutine USDFLD. The algorithm of the subroutine as well as the full Fortran code of the subroutine will be presented.

To demonstrate the prediction capability, all the experiments mentioned in Chapter 3 will be simulated using the newly proposed model and its implementation into FE. The results of simulations of the newly proposed model compared with the original model will be presented.

Chapter 5

Experimental Program

The experimental program mentioned in Chapter 3 has been focused on LCF of austenitic stainless steel 08Ch18N10T. The experimental setup enables to record hysteresis loops during the fatigue life and is described more in detail in [A2].

"The experimental program consists of 6 series of specimens. The first series is used for the material parameter identification process. According to the ASTM E606 standard [43], the classic uniform-gage geometry of a specimen is limited to a total strain amplitude of $\epsilon_a = 0.5\,\%$. For higher strain levels, non-uniform hour-glass type geometry is required in order to prevent buckling. The material parameters identification series (IDF) was therefore compiled from uniform-gage (UG) specimens (see Figure 5.1) and non-uniform-gage specimens with an elliptical longitudinal section (E9, see Figure 5.2).

To identify the material parameters (described in detail in [A1]), it is necessary to know the stress-strain curves in the cycles. For UG specimen geometry, tested according to [43], this can be calculated directly from the elongation of the extensometer and from the force measured during the experiment. For E9 specimen geometry, the strain was measured by the DIC (due to the experimental setup, the strain cannot be calculated directly from the elongation of the extensometer for non-uniform gage geometries)." [A2]

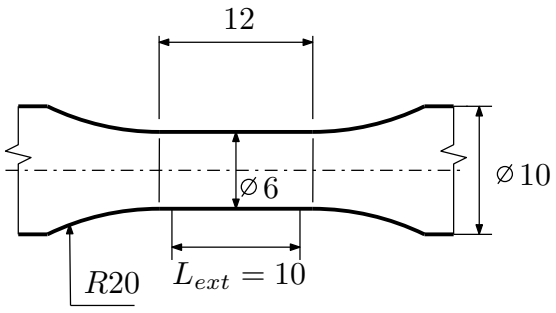

Figure 5.1: Sketch of UG geometry. [A2]

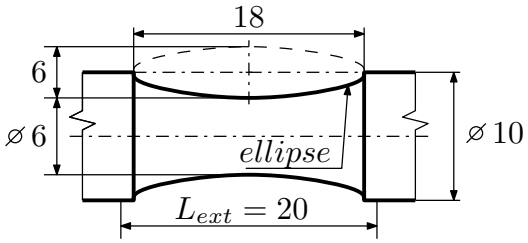

Figure 5.2: Sketch of E9 geometry. [A2]

"The next series consists of E9 geometry (see Figure 5.2), notch geometry with an $R = 1.2\,\text{mm}$ (R1.2, see Figure 5.3), geometry with an $R = 2.5\,\text{mm}$ notch (R2.5,

see Figure 5.4) and geometry with an $R = 5\,\text{mm}$ notch (R5, see Figure 5.5). The last series is the notched tube geometry (NT, see Figure 5.6), which was exposed to torsional loading." [A2]

Boundary conditions of the experiments are listed in Appendix A.

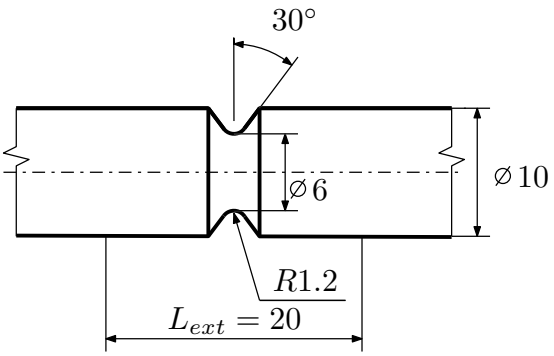

Figure 5.3: Sketch of R1.2 geometry. [A2]

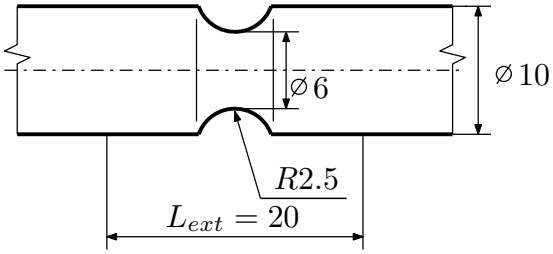

Figure 5.4: Sketch of R2.5 geometry. [A2]

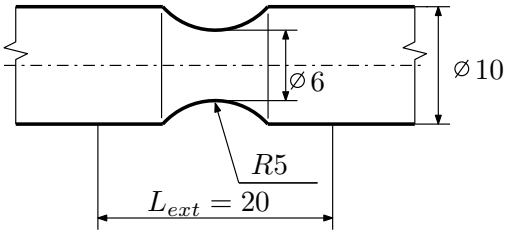

Figure 5.5: Sketch of R5 geometry. [A2]

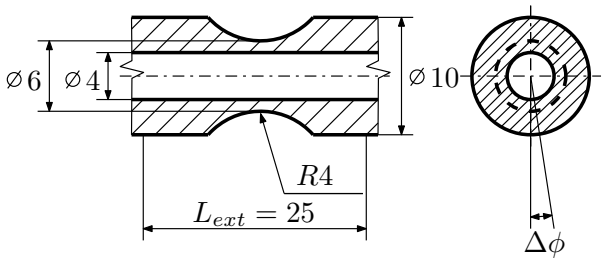

Figure 5.6: Sketch of NT geometry. [A2]

Chapter 6

Constitutive Model of Cyclic Plasticity

A cyclic plasticity model tries to capture the response of the material to the applied load as precisely as possible. The objective is usually to capture the relationship between stress and strain variables. For uniaxial loading, this relationship can be illustrated for example by the hysteresis loop.

To capture the material response, the combined hardening model with memory surface is being used and this has been defined in section 2.1. The kinematic and isotropic hardening rules are then controlled by the size of the memory surface. This allows to control the cyclic hardening (isotropic and kinematic) depending on a strain-range applied to the material and it's history.

In this thesis, the influence of the strain-rate is neglected and only isothermal conditions, at room temperature, are considered.

6.1 The Original Model

6.1.1 Yield Surface and Flow Rule

The single yield surface concept for the metallic materials, based on the von Mises yield criterion, is used. The plasticity function is defined as in equation (2.12)

$$f = \sqrt{\frac{2}{3}(\boldsymbol{\sigma'} - \boldsymbol{\alpha'}) : (\boldsymbol{\sigma'} - \boldsymbol{\alpha'})} - Y = 0, \tag{6.1}$$

where $\boldsymbol{\sigma'}$ is the deviatoric part of the stress tensor $\boldsymbol{\sigma}$, $\boldsymbol{\alpha'}$ is the deviatoric part of the back-stress $\boldsymbol{\alpha}$ and Y is the actual yield stress. The actual yield stress Y is defined as

$$Y = \sigma_Y + R, \tag{6.2}$$

where R is the isotropic variable and σ_y is the yield strength.

"The associative plasticity is considered, so the normality flow rule is considered in the case of active loading

$$d\boldsymbol{\epsilon}^p = d\lambda \frac{\partial f}{\partial \boldsymbol{\sigma}}. \tag{6.3}$$

This expresses mathematically that the plastic strain increment $d\boldsymbol{\epsilon}^p$ is collinear with the exterior normal to the yield surface for the current stress state. In associative plasticity, the scalar multiplier $d\lambda$ is equal to the accumulated plastic strain increment dp, which is defined as

$$dp = \sqrt{\frac{2}{3} d\boldsymbol{\epsilon}^p : d\boldsymbol{\epsilon}^p}." \text{ [A1]} \tag{6.4}$$

The accumulated plastic strain is generally defined as

$$p = \int dp \tag{6.5}$$

6.1.2 Virtual Back-Stress

"A new internal variable is established to provide an easy way to calibrate the model. The variable is the back-stress of a cyclically stable material corresponding to the response of the material investigated under a large strain range. It will be referred to as the virtual back-stress. The Chaboche superposition of the back stress parts is used in the following form

$$\boldsymbol{\alpha}_{virt} = \sum_{i=1}^{M} \boldsymbol{\alpha}^i_{virt} \tag{6.6}$$

taking into consideration the nonlinear kinematic hardening rule of Armstrong and Frederick [13] for each part

$$d\boldsymbol{\alpha}^i_{virt} = \frac{2}{3} C_i d\boldsymbol{\epsilon}_p - \gamma_i \boldsymbol{\alpha}^i_{virt} dp, \tag{6.7}$$

where C_i and γ_i are material parameters. For all calculations in this paper the superposition of three kinematic hardening rules ($M = 3$) will be used." [A1]

"It should be mentioned that the virtual back-stress is used only in the definition of the memory surface, which will be described in the next section. Zero components of the virtual back-stress are considered in the initial state. The increment of the virtual back-stress is calculated according to equations (6.6) and (6.7) assuming the current increment of accumulated plastic strain dp and the current increment of plastic strain tensor $d\epsilon_p$ in each iteration of the local problem. Further details of the implementation algorithm that is used can be found in [44], where a more complex model with the memory surface of Jiang and Sehitoglu [21] was considered." [A1]

6.1.3 Memory Surface

"To provide a correct description of the cyclic hardening for various strain ranges, a memory surface in the stress space is established. The concept is analogous to the theory of Jiang and Sehitoglu [21]. A scalar function is introduced to represent the memory surface in the deviatoric stress space

$$g = \|\boldsymbol{\alpha}_{virt}\| - R_M \leq 0, \tag{6.8}$$

where R_M is the size of the memory surface and $\|\boldsymbol{\alpha}_{virt}\|$ is the magnitude of the total virtual back-stress, which is defined as $\|\boldsymbol{\alpha}_{virt}\| = \sqrt{\boldsymbol{\alpha}_{virt} : \boldsymbol{\alpha}_{virt}}$. The evolution equation ensuring the possibility of memory surface expansion, Figure 6.1, is therefore

$$dR_M = H(g) \left\langle \boldsymbol{L} : d\boldsymbol{\alpha}_{virt} \right\rangle , \tag{6.9}$$

where

$$\boldsymbol{L} = \frac{\boldsymbol{\alpha}_{virt}}{\|\boldsymbol{\alpha}_{virt}\|}." \text{ [A1]} \tag{6.10}$$

The angle brackets in equation (6.9) stands for Macaulay brackets, defined as $\langle x \rangle = x$ for $x \geq 0$ and $\langle x \rangle = 0$ for $x < 0$.

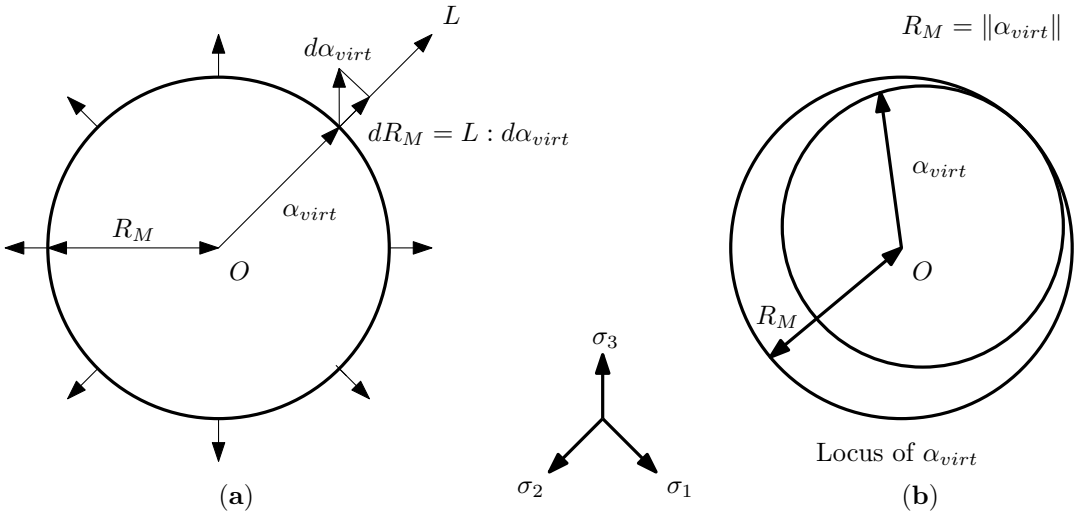

Figure 6.1: Expansion of the memory surface and the stabilized memory surface: (**a**) Equation (6.14) is not active ($\dot{R}_M > 0$); (**b**) Equation (6.14) is active ($\dot{R}_M = 0$). [A1]

6.1.4 Kinematic Hardening Rule

"Consistent with the previous sections, the back-stress is composed of M parts

$$\boldsymbol{\alpha} = \sum_{i=1}^{M} \boldsymbol{\alpha}_i, \tag{6.11}$$

but the memory term is dependent on the size of memory surface R_M and accumulated plastic strain p, thus

$$d\boldsymbol{\alpha}_i = \frac{2}{3} C_i d\boldsymbol{\epsilon}_p - \gamma_i \phi(p, R_M) \boldsymbol{\alpha}_i dp, \tag{6.12}$$

where C_i and γ_i are the same as in equation (6.7). The multiplier ϕ of parameters γ_i is composed of a static part and a cyclic part

$$\phi(p, R_M) = \phi_0 + \phi_{cyc}(p, R_M), \tag{6.13}$$

where ϕ_0 has the meaning of a material parameter, while the cyclic part is variable and can change only in the case of $\dot{R}_M = 0$. In this case, the evolution equation is defined in the following way

$$d\phi_{cyc} = \omega(R_M) \cdot (\phi_\infty + \phi_{cyc}(p, R_M))\, dp, \tag{6.14}$$

$$\phi_\infty(R_M) = A_\infty R_M^4 + B_\infty R_M^3 + C_\infty R_M^2 + D_\infty R_M + F_\infty, \tag{6.15}$$

$$\omega(R_M) = A_\omega + B_\omega R_M^{-C_\omega} \text{ for } R_M \geq R_{M\omega}, \tag{6.16}$$

$$\omega(R_M) = A_\omega + B_\omega R_{M\omega}^{-C_\omega} \text{ otherwise}, \tag{6.17}$$

where A_∞, B_∞, C_∞, D_∞, F_∞, A_ω, B_ω, C_ω, $R_{M\omega}$ and R_{M0} are additional parameters to Chaboche's material parameters C_i and γ_i. The evolution parameter ω directs the rate of cyclic hardening behavior according to the current size of memory surface R_M." [A1]

6.1.5 Isotropic Hardening Rule

"Continuous cyclic hardening has been observed for austenitic stainless steels for a large strain range under uniaxial loading [32]. To capture this behavior, we introduce the linear isotropic hardening rule

$$dR = R_0(R_M)dp, \tag{6.18}$$

where parameter R_0 is dependent on the size of the memory surface

$$R_0(R_M) = A_R R_M^2 + B_R R_M + C_R \text{ for } R_M \geq R_{M0}, \tag{6.19}$$

$$R_0(R_M) = A_R R_{M0}^2 + B_R R_{M0} + C_R \text{ otherwise}, \tag{6.20}$$

because of the strong dependence on the strain range observed in the experiments [32]." [A1]

6.2 Analysis of the Original Model

As has been mentioned in section 2.1, there are two ways to capture the relationship between stress and strain in cyclic plasticity - the isotropic and kinematic hardening. With the memory surface concept, the development of both mechanisms can be defined depending on the applied load and the number of cycles. To capture material behavior for both uniaxial and torsional loading conditions correctly, some of the principles must be revisited and modified.

Isotropic hardening, as is defined in the original model by equation (6.18), is linear function of accumulated plastic strain p. For periodic loading with constant amplitude, e.g. cyclic tests, value of accumulated plastic strain per cycle is almost

constant, which means that R and actual yield stress Y grows practically linearly with number of cycles. But as can be seen in Figure 6.2, it does not reflect how the Y evolves during the fatigue life in 08Ch08N10T steel (the determination of Y from measured experimental data will be described in Chapter 7). In fact, with many cycles, value of Y can theoretically get higher than the stress value and the computed deformation becomes only elastic. This finding offers scope for a new definition of isotropic hardening that better reflects the actual yield stress development during the fatigue life.

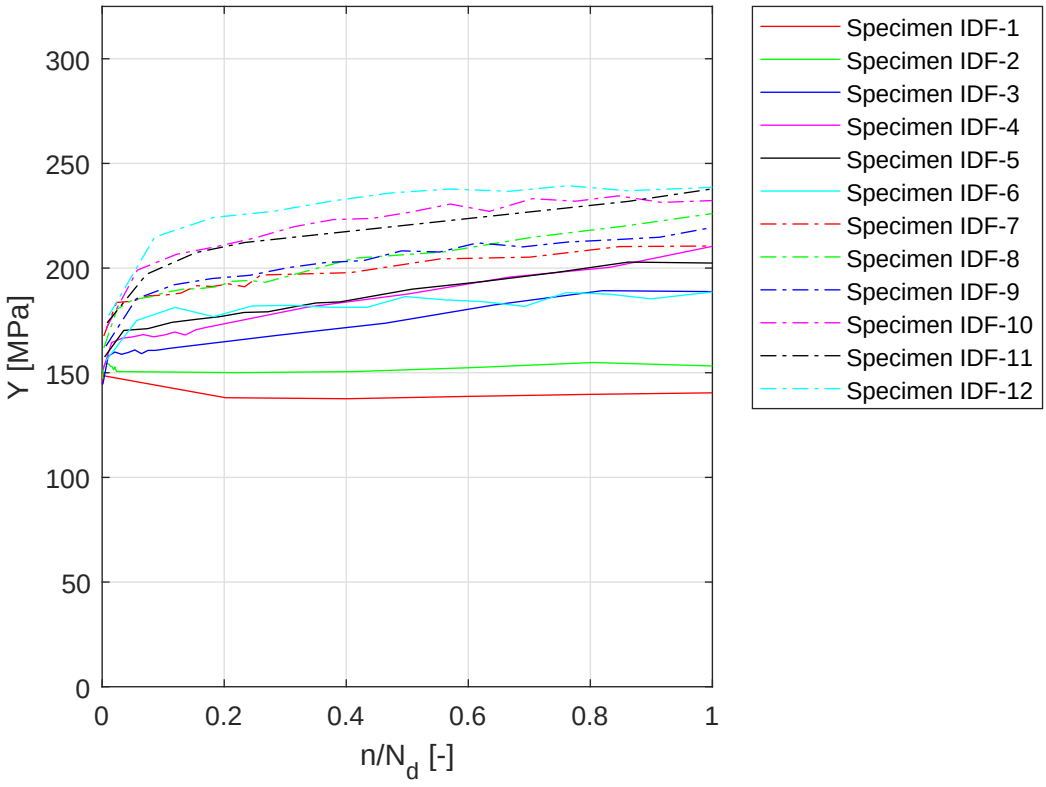

Figure 6.2: The evolution of actual yield stress Y during fatigue life for IDF specimen series.

Let's suppose that the modified isotropic hardening definition is set, new material parameters are identified, the model ability to predict the uniaxial loading is acceptable, but the prediction for torsional loading is still not satisfactory. The proposed modification has to somehow reflect the dominant shear loading. As has been mentioned in Chapter 3, the original model prediction is acceptable for lower loading levels and the over-prediction of cyclic hardening is obvious for higher loading levels. This means that the modification must be strain-range dependent and the only possible way is through the modification of the memory surface definition for shear loading.

6.3 Modification for Shear Stress

In this section, the modification of the original model published in [A1] will be proposed and the new formulation of the constitutive equations of the material model will be presented.

6.3.1 New Formulation of Memory Surface

Professor Chaboche notes in his famous paper [14], which is considered as the first publication dealing with strain-range dependency: "In the last twenty years large improvements have been done in the description of material straining with constitutive equations, including isotropic as well as kinematic hardening parameters. The introduction of such internal variables can be justified through general thermodynamical frameworks but, when identification of macroscopic processes is needed, we choose the following strategy:

- the simplest constitutive equations are used as long as they give a sufficiently good description,
- when a poor modelization is observed (even with an optimized choice of coefficients) we consider that a new macroscopic process is identified and look after new internal variable or new flow equation with more degrees of freedom." [14]

Following this strategy, the author decided to modify the flow[1] equation of memory surface to improve the poor prediction capabilities of the current model under torsional loading conditions.

For functionality and mathematics, the actual size of the memory surface defined in [A1] controls the cyclic hardening for both isotropic and kinematic hardening. As the most effective way to deal with the problem of shear loading conditions, the author choose to define two memory surfaces - the first one to control the isotropic hardening, the second one to control the kinematic hardening. This concept was published in [A2].

The definition of the memory surface for isotropic hardening R_M remains the same as the original one in [A1] defined by the set of equations (6.6-6.10). The definition of the memory surface for the kinematic hardening $R_{M\phi}$ is newly modified. The basic equations remain almost the same as for the isotropic model, but using one extra material parameter, K_{shear}, the evolution equations are modified to capture the torsional loading conditions as well as the uniaxial ones.

"The new memory surface $R_{M\phi}$ for the kinematic hardening part is modified and is defined by analogy as

$$\boldsymbol{\alpha}_{virt\phi} = \sum_{i=1}^{M} \boldsymbol{\alpha}^i_{virt\phi} \tag{6.21}$$

$$d\boldsymbol{\alpha}^i_{virt\phi} = \frac{2}{3} C_i d\boldsymbol{\epsilon}_p - \gamma_i K \boldsymbol{\alpha}^i_{virt\phi} dp \tag{6.22}$$

[1] The meaning of *flow* is in sense of equation (6.3)

where

$$K = (\delta_{IJ} + (1 - \delta_{IJ})K_{shear}) \tag{6.23}$$

where δ_{IJ} is Kronecker delta, I, J are indexes of stress tensor $\boldsymbol{\sigma}$ and K_{shear} is a new material parameter." [A2] Mathematical analysis of equation 6.23 can be easily summarized as $K = 1$ for tensile components of tensor $\boldsymbol{\sigma}$ and $K = K_{shear}$ for the shear components of the tensor $\boldsymbol{\sigma}$.

"The rest of the equations for defining the memory surface of the kinematic hardening part remain analogous to the original model [A1]:

$$dR_{M\phi} = H(g_\phi) \left\langle \boldsymbol{L}_\phi : d\boldsymbol{\alpha}_{virt\phi} \right\rangle \tag{6.24}$$

where

$$g_\phi = \|\boldsymbol{\alpha}_{virt\phi}\| - R_{M\phi} <= 0 \tag{6.25}$$

and

$$\boldsymbol{L}_\phi = \frac{\boldsymbol{\alpha}_{virt\phi}}{\|\boldsymbol{\alpha}_{virt\phi}\|}" \text{ [A2].} \tag{6.26}$$

"A quick analysis of this modified formulation shows that it provides practically the same prediction in uniaxial loading conditions (because $R_{M\phi} \simeq R_M$) as the original formulation. However, depending on the value of K_{shear}, it can give a different prediction under shear loading conditions: it is more effective for higher loading levels than for lower loading levels, and it can reduce the over prediction of the model for $K_{shear} > 1$." [A2]

"The second modification to the original model [A1], also associated with the memory surface, is to omit limits $R_{M\omega}$ and R_{M0} and to set boundaries of the memory surfaces instead: R_M^{min} and R_M^{max}. The value of the memory surface R_M and $R_{M\phi}$ used for controlling the isotropic and kinematic hardening part can lie only between these two bounds. For simplification, and for mathematically correct expression, the memory surface size that is used, R_M^{used}, is defined as

$$R_M^{used} = R_M^{min} \text{ for } R_M < R_M^{min} \tag{6.27}$$

$$R_M^{used} = R_M \text{ for } R_M^{min} < R_M < R_M^{max} \tag{6.28}$$

$$R_M^{used} = R_M^{max} \text{ for } R_M > R_M^{max} \tag{6.29}$$

and analogously for $R_{M\phi}^{used}$" [A2]:

$$R_{M\phi}^{used} = R_M^{min} \text{ for } R_{M\phi} < R_M^{min} \tag{6.30}$$

$$R_{M\phi}^{used} = R_{M\phi} \text{ for } R_M^{min} < R_{M\phi} < R_M^{max} \tag{6.31}$$

$$R_{M\phi}^{used} = R_M^{max} \text{ for } R_{M\phi} > R_M^{max}. \tag{6.32}$$

6.3.2 Kinematic Hardening

The definition of kinematic hardening remains almost the same as in the original model [A1], but now the memory surface size R_M in equations (6.12-6.17) of the original model is replaced by the variable $R_{M\phi}^{used}$. The kinematic hardening equations is now defined as

$$d\boldsymbol{\alpha}_i = \frac{2}{3} C_i d\boldsymbol{\epsilon}_p - \gamma_i \phi(p, R_{M\phi}^{used}) \boldsymbol{\alpha}_i dp \tag{6.33}$$

$$\phi(p, R_{M\phi}^{used}) = \phi_0 + \phi_{cyc}(p, R_{M\phi}^{used}) \tag{6.34}$$

$$d\phi_{cyc} = \omega(R_{M\phi}^{used}) \cdot \left(\phi_\infty + \phi_{cyc}(p, R_{M\phi}^{used})\right) dp \tag{6.35}$$

$$\phi_\infty(R_{M\phi}^{used}) = A_\infty (R_{M\phi}^{used})^4 + B_\infty (R_{M\phi}^{used})^3 + C_\infty (R_{M\phi}^{used})^2 + D_\infty R_{M\phi}^{used} + E_\infty \tag{6.36}$$

$$\omega(R_{M\phi}^{used}) = A_\omega + B_\omega (R_{M\phi}^{used})^{-C_\omega}. \tag{6.37}$$

This modification has been published in [A2].

6.3.3 New Formulation of Isotropic Haredning

As can be seen in Figure 6.2, for higher levels of loading, the actual yield stress Y is a non-linear function of N. For periodic loading with approximately constant amplitude, $N \approx p$, so Y also must be a non-linear function of p. For this reason, the isotropic hardening is newly defined as a non-linear function in p (instead of a linear definition in the original model [A1]) as

$$dR = A_R \cdot \exp(B_R \cdot R_M^{used}) \cdot p^{C_R}, \tag{6.38}$$

where A_R, B_R and C_R are material parameters. This modification has been published in [A2].

Chapter 7

Material Parameters Identification

The material parameters of the proposed material model have been identified for the original experimental data of austenitic stainless steel 08Ch18N10T using the Matlab software. As has been reviewed in section 2.3, the usual way of material parameters identification is throug fitting the parameters on static and cyclic stress strain curve.

Due to complexity of the strain-range dependent cyclic hardening of 08Ch18N10T steel, the author decided to modify the existing approaches and to develop the new calibration method. This method is based on direct simulation of the material response using the incremental material model of cyclic plasticity in the same way as is used in FEA simulations. No analytical simplification in the sense of (2.37-2.40) has been used, all the material parameters have been identified using multiple optimizations process to match the hysteresis loop shape or amplitude between experiment and simulation.

This process requires complete records of the experiments including the hysteresis loops data in good resolution during the whole fatigue life and for all specimens used for the calibration process. This process is also very demanding on computing power and in a reasonable amount of time, it can only be performed on high performance computers. On the other hand, this approach should lead to a better results for more complex material behavior, because it simulates the behavior of the material in the same way as the subsequent FEM computations, so, for same inputs, it leads to the same results as the simulation. The material parameters identification process has been published in [A1], [A2], [A3] and [A7].

7.1 Chaboche Material Parameters

The material parameters for uniaxial loading has been identified using 12 specimens, marked by the abbreviation IDF in the following text, each specimen representing a different level of loading. "According to the ASTM standard [43], the classic uniform-gage geometry of the specimen is limited up to the amplitude of the total strain $\epsilon_a = 0.5\,\%$. For higher strain levels, an hour-glass type geometry is required. According to this standard, the IDF specimens were compiled from uniform-gage geometry (specimens IDF1-IDF5) and hourglass geometry (specimens IDF6-IDF12), see Figures 5.1 and 5.2 in Chapter 3." [A1].

The design of the hourglass geometry has been found in order to prevent buckling during the testing. The process of finding the optimal design of the hourglass geometry is described in detail in [A5] and [A11].

Following text is directly cited from [A1]. "The loading force F applied to the IDF specimen was known, as was the strain field of the surface of the specimen. The strain field was measured by the extensometer in the case of uniform-gage geometry, or by the digital image correlation method in the case of hourglass geometry. Considering the uniaxial stress field in the cross-section of a specimen, the stress can be determined as

$$\sigma = \frac{F}{A}, \tag{7.1}$$

where A is the cross-section surface of the specimen. This allows the use of a different calibration process, based on knowledge of the shape of the stress-strain hysteresis loops in all cycles during the experiment to failure.

Let us select one hysteresis stress-strain loop of a point on the specimen representing one loading cycle. This can be optimally simulated by a set of material parameters C_1, γ_1, C_2, γ_2, C_3, γ_3 and σ_y. However, in the next cycle, the optimal set of these parameters can be slightly different, as can the set of parameters of a specimen with different loading conditions. This material model uses the memory surface concept by setting these material parameters as functions of R_M and making these coefficients dependent on the loading history and the loading level conditions.

The material model did not include a simulation of the material damage process, so only experimental data up to damage were used for the calibration. The number of cycles used is N_d, and this number corresponded with the drop in the loading force during the experiment by 2 %, due to crack initiation and propagation leading to failure.

First, the fatigue life is divided into about 10 evenly spaced parts by selecting hysteresis loops (SHLs), and the cycle number of each selected hysteresis loop (SHL) is given as $N \simeq N_d/k$, where $k = 1, 2, \ldots, 10$. The Young modulus E, the Poisson ratio ν and the yield strength σ_y were determined from tensile test according to ISO standard [39].

σ_y can be interpreted as the point where the linear part of the static stress-strain curve turns into the non-linear part (see Figure 7.1). The root mean squared error method ($RMSE$) can be applied to find the point. In the tensile test (or in the first cycle of the cyclic test), the yield strength σ_y corresponded to $RMSE \approx 8$. Applying $RMSE = 8$ to each SHL, the actual yield stress Y was found. This shows the development of the actual yield stress Y during the fatigue life, see Figure 6.2 in Chapter 6.

Two SHLs were chosen, the bigger one and the smaller one, each with cycle number $N = N_d$ (the last cycle). The Chaboche material model parameters C_1, γ_1, C_2, γ_2, C_3, γ_3 were found using an optimization process. The target function is set to the optimal shape match between simulation and experiment of the two SHLs." [A1] The shape match of hysteresis loops is compared in discrete points, the least square method is used to calculate the error between experiment and simulation. This discrete comparison can be done because of the simulation of hysteresis loop is controlled by the same discrete values of strain ϵ as the experiment

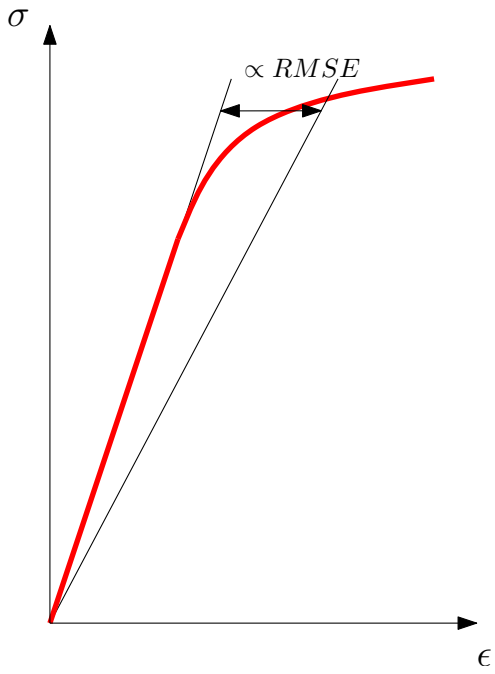

Figure 7.1: Actual yield stress determination. [A1]

and only the computed values of stress σ are different. The experimental data are centered in strain axis for the purpose of this calibration step. The basic algorithm of Chaboche parameters identification process has been taken from [A12]. The results of calibration process for optimal Chaboche parameters are shown in Figure 7.2.

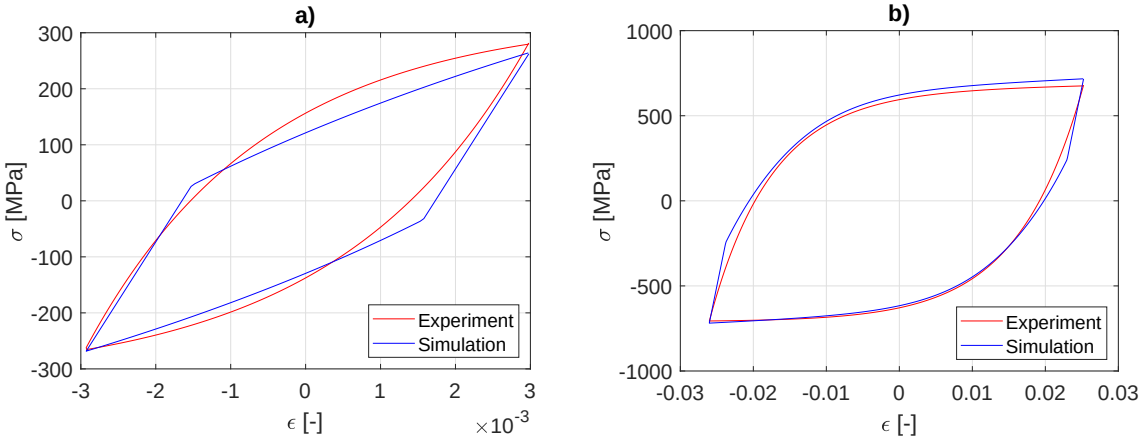

Figure 7.2: Chaboche material parameters fitting: (**a**) small hysteresis loop, (**b**) large hysteresis loop. [A1]

7.2 Cyclic Hardening Parameters

"Knowing the Chaboche material parameters, a first guess of the memory surface size for each specimen was determined, using equations (6.22-6.26). The formulation of R_M and the constant amplitude of the loading conditions resulted in fast saturation

of the R_M value for each specimen (after the first cycle), which makes the calibration process easier." [A1]

"It is assumed here that $R_{M\phi} \simeq R_M$. Boundary parameters R_M^{min} and R_M^{max} are simply the maximum and minimum values of R_M computed in the identification process." [A2] The illustration of memory surface size fitting for loading level given by the amplitude of strain ϵ_a is in Figure 7.3. Due to the experimental setup and the method of controlling the cyclic test, ϵ_a is almost, but not completely constant during the whole fatigue life for hourglass specimens, so the mean value of ϵ_a has been calculated. Details of determining the mean value can be found in [A8].

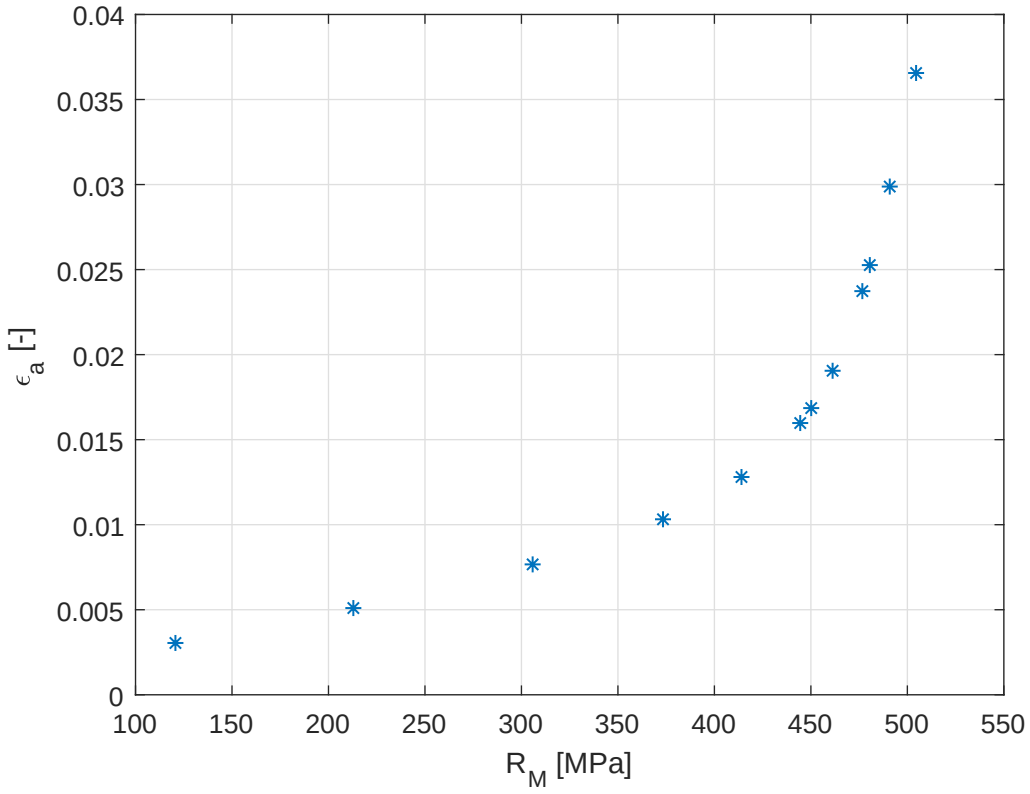

Figure 7.3: R_M for given ϵ_a.

"The yield stress is now fitted as a function of R_M, using equation (6.38), by finding the material parameters A_R, B_R and C_R." [A1] For illustration of actual yield stress fitting, see Figure 7.4.

"Using the static stress-strain curve experimental data and performing a simulation of this curve, parameter ϕ_0 was found using equation (6.33) as an optimal value of ϕ for the static stress-strain curve simulation." [A1] The error between experimental static stress-strain curve and the simulation is calculated discretely using the least square method. The illustration of fitting the material parameter ϕ_0 and the discretization is in Figure 7.5.

"The value of function ϕ from equation (6.33) was found for SHLs, using a similar optimization process as for determining the Chaboche material parameters." [A1] This step defines the ideal value of the Marquis parameter ϕ for each SHL. "ϕ_∞ was the value of ϕ for $N = N_d$ and, from equation (6.36), ϕ_∞ was then set as a function of R_M by finding the material parameters A_∞, B_∞, C_∞,D_∞ and F_∞. The function

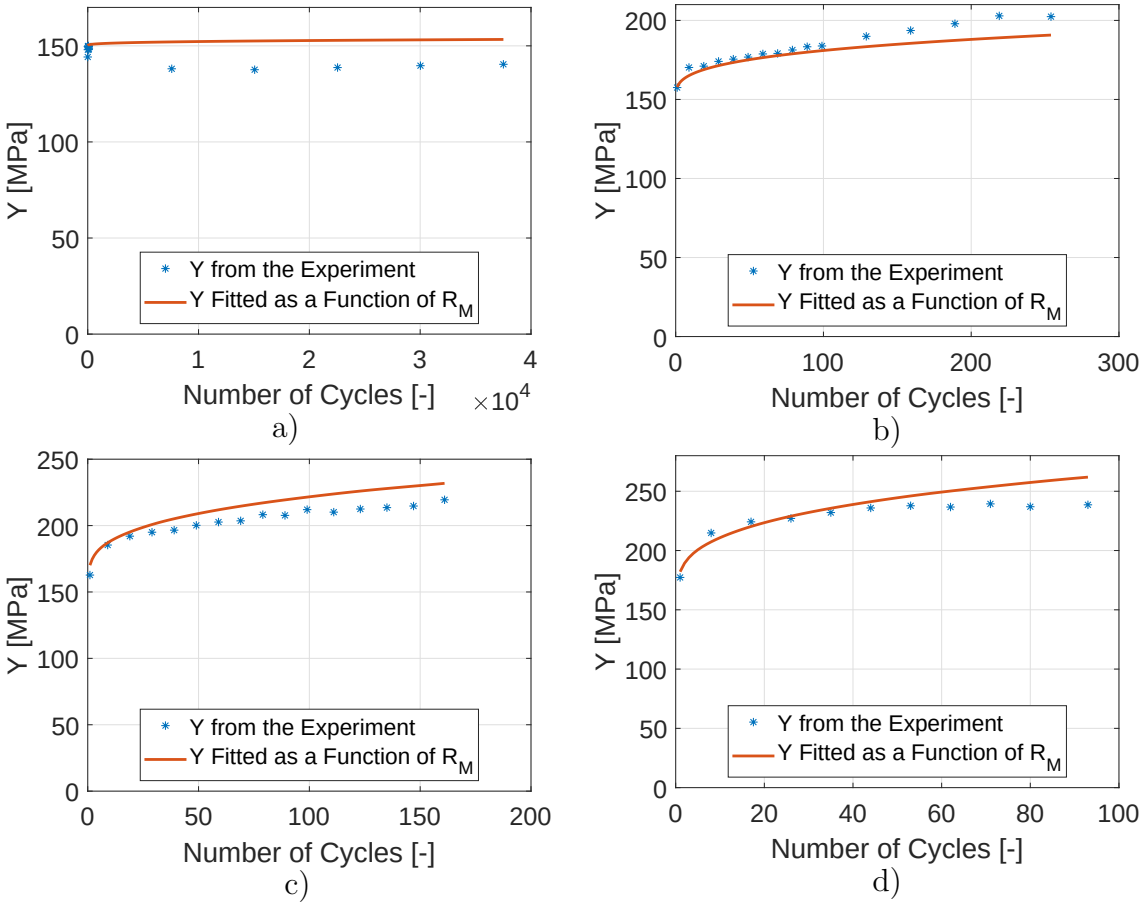

Figure 7.4: Example of Y fitting: (**a**) specimen IDF1, (**b**) specimen IDF5, (**c**) specimen IDF9, (**d**) specimen IDF12.

ω determined the transition of the function ϕ between its border values ϕ_0 and ϕ_∞. Knowing the course of function ϕ during the fatigue life, ω was determined as a function of R_M by finding the material parameters A_ω, B_ω and C_ω from equation (6.37). This result was not necessarily optimal, so one more optimization was performed to find better ϕ_∞ and ω material parameters. The target function was set to the best possible match of the amplitude stress response between simulation and experiment during the whole fatigue life (not only SHLs)."[A1] The match is also calculated using the incremental hysteresis loop simulation. The illustration of fitting ϕ_∞ and ω as a function of R_M is in Figures 7.6 and 7.7. Results of final fit (after iteration process) of the Marquis parameter ϕ during the fatigue life of selected IDF specimens are in Figure 7.8. Simulation results after the final process of material parameter identification is compared with the experimental data on Figure 7.9.

"The R_M value for each specimen was determined only as a first guess, so a number of iterations of the whole calibration process had to be carried out to find the final and optimal set of material parameters." [A1] The complete code of the material model, that will be presented in section 8.2.3, is used for this optimization (here only converted from Fortran to Matlab programming language).

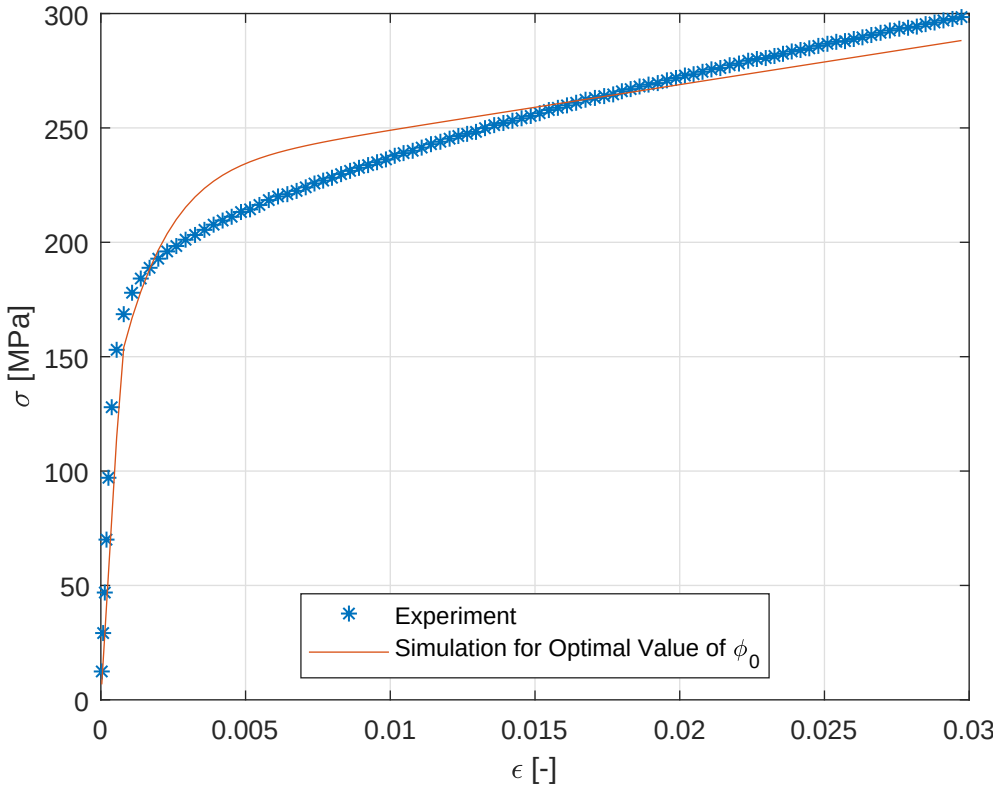

Figure 7.5: Fitting the material parameter ϕ_0 from static stress-strain curve.

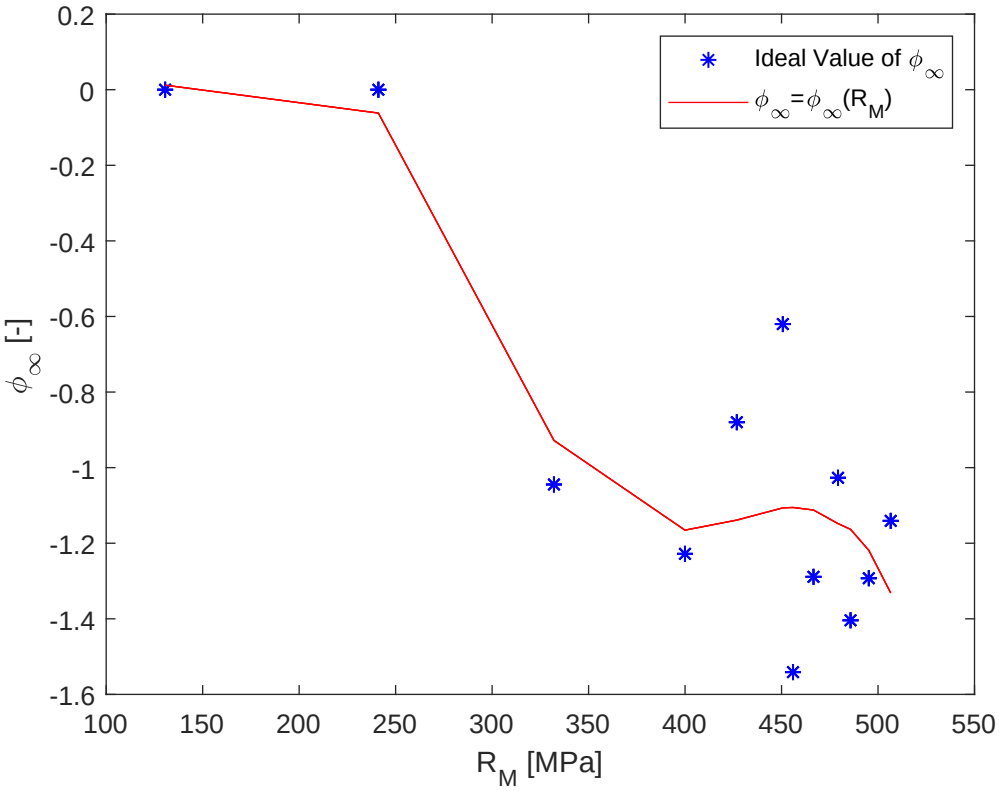

Figure 7.6: Fitting the ϕ_∞ as a function of R_M.

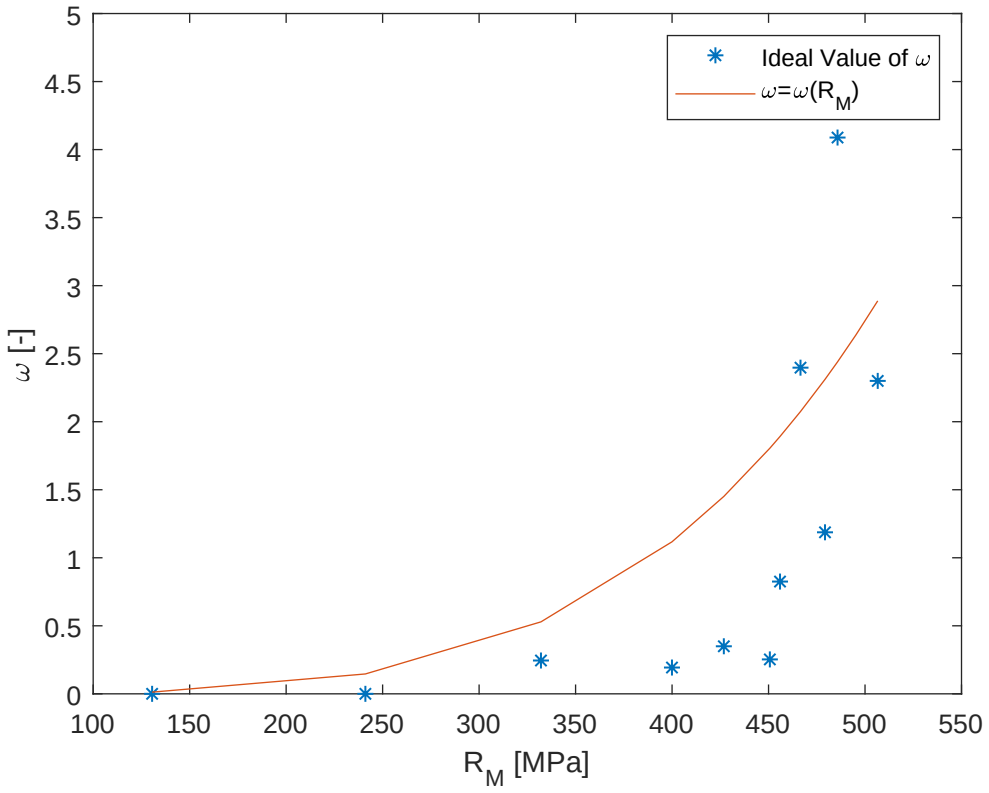

Figure 7.7: Fitting the ω as a function of R_M.

7.3 Torsional Loading

"For each NT geometry specimen tested, the *Error* value in each cycle between the experimental amplitude of torque T_a^{exp} and the simulation amplitude of torque T_a^{sim} can be defined as

$$Error = (T_a^{exp} - T_a^{sim})/T_a^{exp} \cdot 100\,[\%]. \tag{7.2}$$

The $MeanError$ over all cycles is calculated as

$$MeanError = \frac{1}{N_d} \sum_{N=1}^{N_d} Error_n, \tag{7.3}$$

where index N is the number of cycles. The total error over all NT geometry specimens tested is defined as

$$TotalError = \frac{1}{S} \sum_{s=1}^{S} MeanError_s \tag{7.4}$$

where s is the NT specimen index and $S = 8$ is the total number of NT specimens tested (see Table A.3 in Appendix A for details)." [A2]

"For the different K_{shear} from equation (6.23), the $TotalError$ value is captured in Figure 7.10. The final K_{shear} material parameter is identified as the optimal value of K_{shear} where the $TotalError$ is minimal. The material value parameters are presented in Table 7.1." [A2]

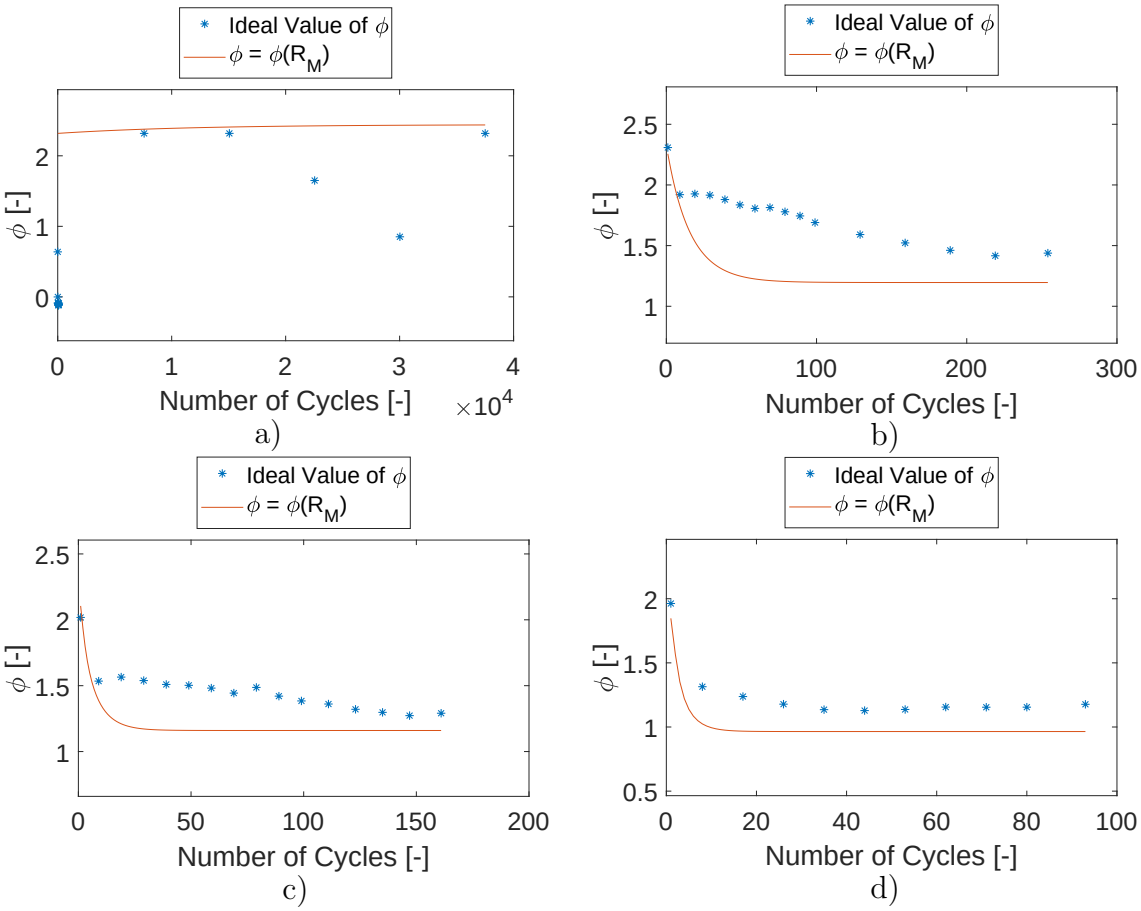

Figure 7.8: Example of the ϕ function fitting for SHLs: (**a**) specimen IDF1, (**b**) specimen IDF5, (**c**) specimen IDF9, (**d**) specimen IDF12.

Table 7.1: Material parameters of the new proposed model for 08Ch18N10T. [A2]

$\boldsymbol{E}$ [MPa]	$\boldsymbol{\nu}$	$\boldsymbol{\sigma_y}$ [MPa]	$\boldsymbol{C_1}$ [MPa]	$\boldsymbol{\gamma_1}$
210,000	0.3	150	63,400	148.6
$\boldsymbol{C_2}$ [MPa]	$\boldsymbol{\gamma_2}$	$\boldsymbol{C_3}$ [MPa]	$\boldsymbol{\gamma_3}$	$\boldsymbol{A_\infty}$
10,000	911.4	2000	0	-1.3127×10^{-9}
$\boldsymbol{B_\infty}$	$\boldsymbol{C_\infty}$	$\boldsymbol{D_\infty}$	$\boldsymbol{F_\infty}$	$\boldsymbol{A_R}$ [MPa^{-1}]
1.7981×10^{-6}	-8.6705×10^{-4}	1.6678×10^{-1}	-10.600	3.0113×10^{-1}
$\boldsymbol{B_R}$	$\boldsymbol{C_R}$ [MPa]	$\boldsymbol{R_M^{min}}$ [MPa]	$\boldsymbol{A_\omega}$	$\boldsymbol{B_\omega}$
1.4865×10^{-1}	1.1818×10^{-2}	130.54	0	2.0024×10^{-13}
$\boldsymbol{C_\omega}$	$\boldsymbol{R_M^{max}}$ [MPa]	$\boldsymbol{\phi_0}$	$\boldsymbol{K_{shear}}$	
-4.8591	506.59	2.3178	1.5	

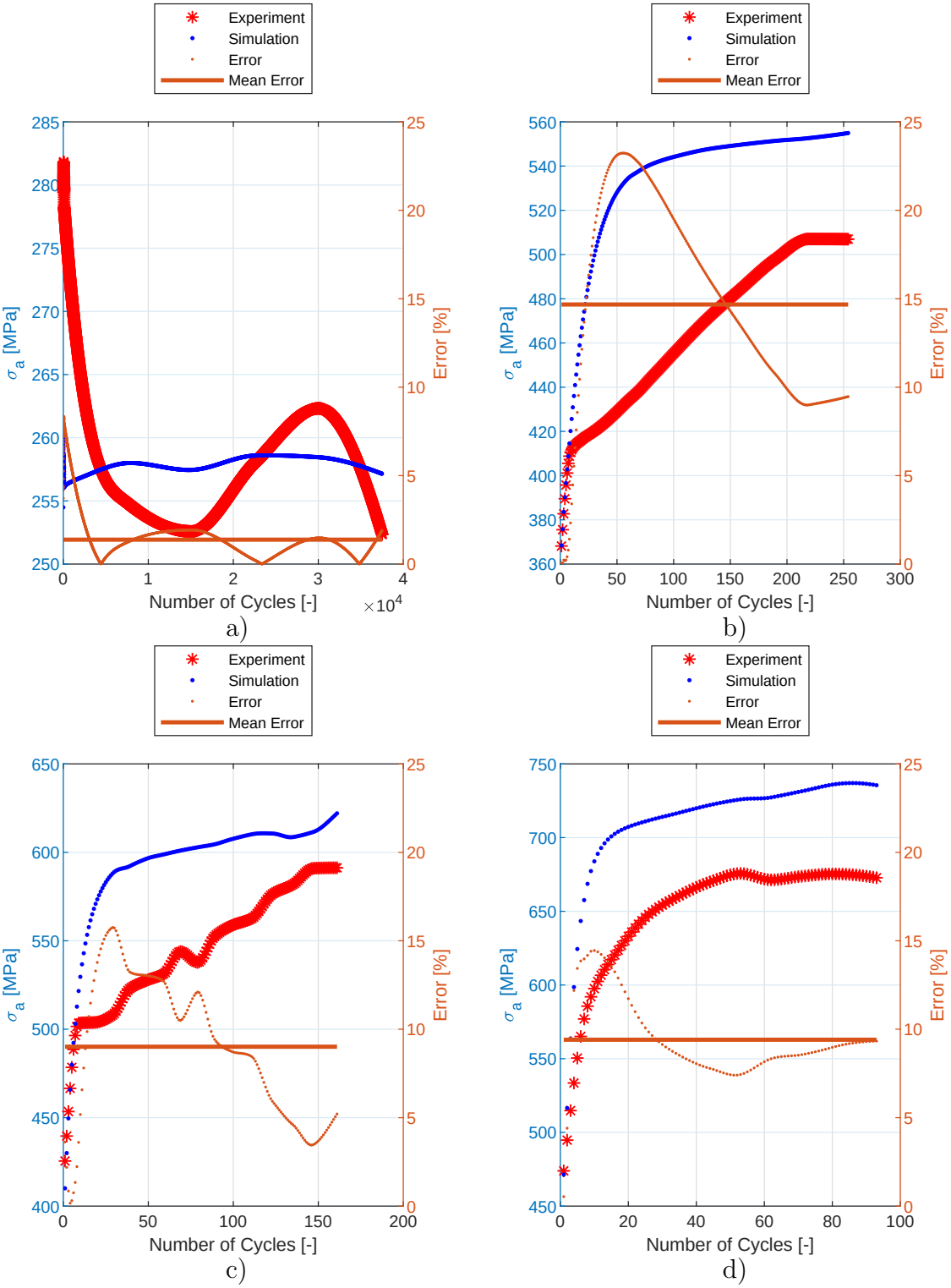

Figure 7.9: Experiment vs. simulations for selected IDF specimens: (**a**) specimen IDF1, (**b**) specimen IDF5, (**c**) specimen IDF9, (**d**) specimen IDF12.

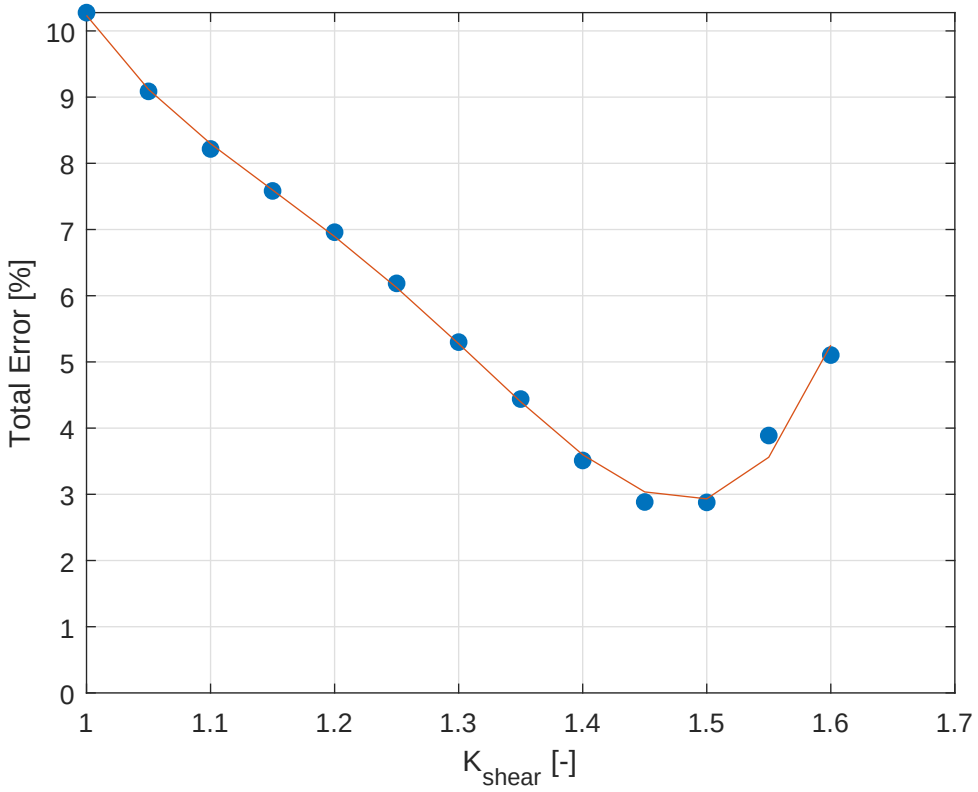

Figure 7.10: Identification of the K_{shear} material parameter. [A2]

Chapter 8

Implementation of Proposed Model into Finite Element Analysis

"The geometry of most specimens is not uniform, so the non-uniform stress and strain field in their cross-section are expected and FEA must be used for simulations." [A2] In this chapter, the FE model is described as well as the implementation of presented material model into commercial FE software Abaqus using the USDFLD subroutine. "This subroutine makes possible to use the material model presented here in engineering computations. Combined with the material parameters identification process described in Chapter 7, it can also be used for other materials." [A2] The example of practical use can be found in [A6], where the proposed material model is used to simulate the pipe flange load.

8.1 FE Model

FE models of each of the tested geometries were created, see Figures 8.1-8.6. The UG, E9, and notched geometries R1.2, R2.5, and R5 are modeled as an axisymmetric model, the NT geometry is modeled as a 3D model using cyclic symmetry. "The symmetry boundary condition is defined on the right edge of the model. The left edge of the model always corresponds with the cross-section where the extensometer is attached to the body of the specimen during the experiment. The displacement boundary condition on the left edge of the FE model is created with the same amplitude value as was recorded from the extensometer during the experiment. Abaqus CAX8R mesh elements are used for the axisymmetric models and C3D8R elements are used for the NT geometry." [A2]. Using sensitivity study, the element size in fine mesh areas has been determined to be 0.1 mm except for the UG geometry, where the element size is 0.5 mm for the whole model.

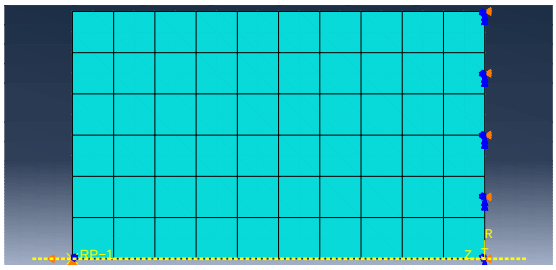

Figure 8.1: FE model of UG specimen. [A2]

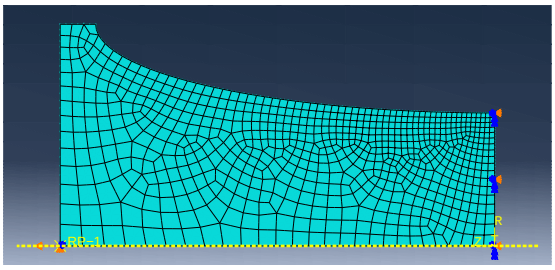

Figure 8.2: FE model of E9 specimen. [A2]

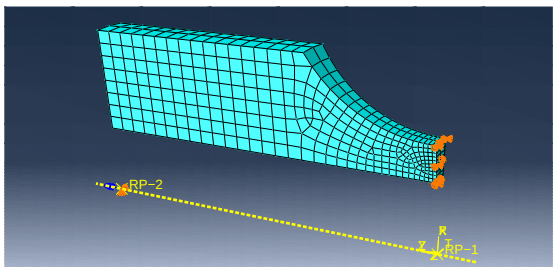

Figure 8.3: FE model of NT specimen. [A2]

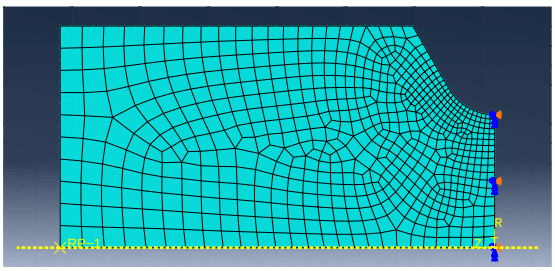

Figure 8.4: FE model of R1.2 specimen. [A2]

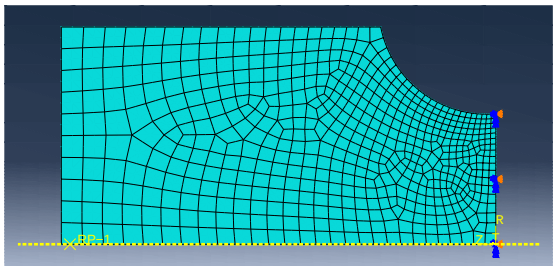

Figure 8.5: FE model of R2.5 specimen. [A2]

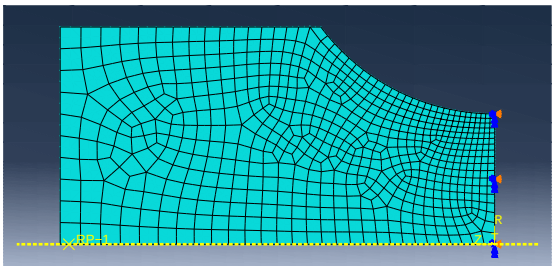

Figure 8.6: FE model of R5 specimen. [A2]

8.2 Implementation of Material Model Using USDFLD Subroutine

8.2.1 A general description of USDFLD Subroutine

There are several ways how to implement proposed material model into commercial FE software Abaqus. One possible way is the UMAT (User MATerial) subroutine, where the material behavior must be fully programmed by the user. For a given increment of the strain tensor, the user must program the constitutive equations to define the internal variables, stress tensor, and the consistent Jacobian matrix. The coding of non-linear plasticity model is lengthy, laborious and the definition of consistent Jacobian matrix (see equation (2.22)) is very complicated and requires considerable mathematical skills.

The easier way is to use USDFLD (USer Defined FieLD) subroutine. In this

subroutine, the user must define the array called $FIELD$, which can contain one or more components. The combined hardening model of plasticity, as defined in equation (2.34), is already implemented in Abaqus. The material parameters C_i, γ_i, and Y can be defined as constants or as a function of the $FIELD$ array, so the material parameters may change during the simulation as the $FIELD$ values changes. In USDFLD subroutine, the user has to define the calculation of $FIELD$ components and it can be defined as a function of some input variables. The choice of inputs is up to the user. The values of material parameters C_i, γ_i, and Y, for a specific value of $FIELD$ components, is then defined by the user in the Abaqus input file in the form of the text table.

For example, if the user choose the $FIELD$ array to contain 2 components, $FIELD(1)$ and $FIELD(2)$, the user must define a table row values of C_i, γ_i, and Y for some values $FIELD(1)$ and $FIELD(2)$ and then on the next row values of C_i, γ_i, and Y for different values $FIELD(1)$ and $FIELD(2)$. Abaqus uses the linear interpolation (or extrapolation) between the data in the table for given values of $FIELD$ array to find the exact values of the material parameters.

A very clear way to select variables, to be the $FIELD$ array variables, is to select $FIELD(1) = Y$ and $FIELD(2) = \phi$. The material parameters are then calculated as $C_i = C_i$, $\gamma_i = \gamma_i \cdot \phi$, and $Y = Y$.

There are several advantages of using USDFLD instead of UMAT:

- Abaqus has already implemented a combined model of plasticity, which has been already optimized by Abaqus developers for speed and effectiveness, so it is way faster than UMAT.
- The user does not have to define a complete constitutive model of cyclic plasticity, only the definition of $FIELD$ array, the code is several times shorter.
- The user does not have to define a consistent Jacobian matrix, which is complicated and advanced mathematical skill demanding process. Also, with even minor modification of constitutive equations of plasticity, a consistent Jacobian matrix has to be redefined in case of using the UMAT subroutine.

The disadvantage of USDFLD compared to UMAT is that all input variables, for the current increment, are taken from the end of the previous increment and they are not updated during the current increment. Due to this limitation, the USDFLD is sensitive to maximal increment size, therefore, for the given model, material parameters, and loading conditions, the sensitivity study has to be done to determine the highest applicable increment. But there is a convergence in increment size in a similar way as in the element size of the mesh.

8.2.2 Building the USDFLD Subroutine of Proposed Model

As has been mentioned in section 8.2.1, the result of the USDFLD subroutine code for the proposed material model is the definition of $FIELD(1) = Y$ and $FIELD(2) = \phi$. The brief logic of building the USDFLD subroutine can be summerized in following points:

- Variables and material parameters are defined.

- Vector[1] of plastic strain $\boldsymbol{\epsilon^p}$ and accumulated plastic strain p are obtained from previous increment.
- Flow vector from equation (6.3) is calculated.
- Vectors $\boldsymbol{\alpha_{virt}}$ and $\boldsymbol{\alpha_{virt\phi}}$ from equations (6.6-6.7) and (6.21-6.22) are calculated.
- The equations (6.8-6.10), (6.25-6.26) and (6.27-6.32) leading to determining the size of memory surfaces R_M^{used} and $R_{M\phi}^{used}$ are calculated.
- The isotropic variable R from equation (6.38) is calculated, actual yield stress is determined as $Y = \sigma_y + R$.
- Variables ϕ_∞, ω, and ϕ_{cyc} from equations (6.36), (6.37) and (6.35) are calculated.
- Variable ϕ from equation (6.34) is calculated.
- Some variables are stored to user defined state variable output $STATEV$ (for control purposes only).
- $FIELD$ array values for current increment are defined as $FIELD(1) = Y$, $FIELD(2) = \phi$.

8.2.3 USDFLD Subroutine Code

The full Abaqus USDFLD subroutine code written in Fortran programming language is presented including the material parameters definition in the Abaqus input file. The Fortran code of the subroutine has been published in [A2].

Full Fortran Code of Abaqus USDFLD Subroutine [A2]

```
CCCCCCCCCCCCCCCCCCCCCCCCCCCCCCCCCCCCCC
C Material model by Miro Fumfera C
C        version 2019-11-10        C
CCCCCCCCCCCCCCCCCCCCCCCCCCCCCCCCCCCCCC
C      USDFLD Subroutine for 08Ch18N10T Austenitic Stainless Steel
C      Original modely by Radim Halama
C      modified by Miro Fumfera for 08Ch18N10T
       SUBROUTINE USDFLD(FIELD,STATEV,PNEWDT,DIRECT,T,CELENT,
      1 TIME,DTIME,CMNAME,ORNAME,NFIELD,NSTATV,NOEL,NPT,LAYER,
      2 KSPT,KSTEP,KINC,NDI,NSHR,COORD,JMAC,JMATYP,MATLAYO,LACCFLA)
       INCLUDE 'ABA_PARAM.INC'
       CHARACTER*80 CMNAME,ORNAME
       CHARACTER*3  FLGRAY(15)
       DIMENSION FIELD(NFIELD),STATEV(NSTATV),DIRECT(3,3),T(3,3),TIME(2)
       DIMENSION ARRAY(15),JARRAY(15),JMAC(*),JMATYP(*),COORD(*)
       parameter ZERO=0D0,ONE=1D0,TWO=2D0,THREE=3D0,TOLER=1D-12,
```

[1] Abaqus (and other FE softwares) uses Voigt 6 component vector notation for 3x3 symmetric tensor.

```
     + NTENS=6 !NTENS=4 for Axisymetric, NTENS=6 for 3D
       real*8 RMused,RM,RMmax,RMmin,oRM,dRM, RMRused,RMR,oRMR,dRMR,
     + heavisideG,DDP,G,DirVec(NTENS),DirVecR(NTENS)
       real*8 ALPHAv(NTENS),dALPHA1v(NTENS),ALPHA1v(NTENS),
     + dALPHA2v(NTENS),ALPHA2v(NTENS),dALPHA3v(NTENS),ALPHA3v(NTENS),
     + dALPHAv(NTENS),oALPHAv(NTENS),magALPHAv
       real*8 ALPHAr(NTENS),dALPHA1r(NTENS),ALPHA1r(NTENS),
     + dALPHA2r(NTENS),ALPHA2r(NTENS),dALPHA3r(NTENS),ALPHA3r(NTENS),
     + dALPHAr(NTENS),oALPHAr(NTENS),magALPHAr
       real*8 EPLAS(NTENS),oEPLAS(NTENS),dEPLAS(NTENS),EQPLAS,oEQPLAS,
     + dEQPLAS,FLOW(NTENS)
       real*8 R,oR,dR,AR,BR,CR,ER
       real*8 PhiInfty,dPHIcyc,PHIcyc,oPHIcyc,PHI0,PHI
       real*8 AInfty,BInfty,CInfty,DInfty,EInfty
       real*8 AOmega,BOmega,COmega
       real*8 KShear
       real*8 C1,GAMMA1,C2,GAMMA2,C3,GAMMA3
       integer K1,iEPLAS,iALPHA1v,iALPHA2v,iALPHA3v,iEQPLAS,iRM,iPHI,
     + iPHIcyc,iALPHAv,iR,iFIELD1,iFIELD2,iALPHA1r,iALPHA2r,iALPHA3r,
     + iRMR,iALPHAr
       parameter(iEPLAS=7,iALPHA1v=31,iALPHA2v=37,iALPHA3v=43,iEQPLAS=49,
     + iR=50,iRM=51,iPHI=52,iPHIcyc=53,iPhiInfty=54,iRMR=61,iALPHA1r=71,
     + iALPHA2r=77,iALPHA3r=83,iRMRused=95,iRMused=96,iALPHAv=97,
     + iALPHAr=94,iFIELD1=98,iFIELD2=99)
C      Material parameters
       C1 = 6.339971e+04
       GAMMA1 = 1.485569e+02
       C2 = 9.999778e+03
       GAMMA2 = 9.113512e+02
       C3 = 2000
       GAMMA3 = 0
       SYIELD = 150
       PHI0 = 2.317802e+00
       AInfty = -1.312737e-09
       BInfty = 1.798138e-06
       CInfty = -8.670490e-04
       DInfty = 1.667770e-01
       EInfty = -1.060028e+01
       RMmin = 1.305410e+02
       RMmax = 5.065918e+02
       BR = 3.011316e-01
       CR = 1.486489e-01
       ER = 1.181843e-02
       AOmega = 0
       BOmega = 2.002387e-13
       COmega = -4.859126e+00
       KShear = 1.50
C      get PE components
       call GETVRM('PE',ARRAY,JARRAY,FLGRAY,JRCD,JMAC,JMATYP,
     +  MATLAYO,LACCFLA)
C      EQPLAS
       EQPLAS = ARRAY(7)
       oEQPLAS = STATEV(iEQPLAS)
       dEQPLAS = EQPLAS - oEQPLAS
C      get PE
       do K1=1,NTENS
```

```
        oEPLAS(K1) = STATEV(iEPLAS-1+K1)
        EPLAS(K1) = ARRAY(K1)
        dEPLAS(K1) = EPLAS(K1) - oEPLAS(K1)
      enddo
C     get ALPHAv
      do K1=1,NTENS
        ALPHA1v(K1) = STATEV(iALPHA1v-1+K1)
        ALPHA2v(K1) = STATEV(iALPHA2v-1+K1)
        ALPHA3v(K1) = STATEV(iALPHA3v-1+K1)
        oALPHAv(K1) = STATEV(iALPHAv-1+K1)

        ALPHA1r(K1) = STATEV(iALPHA1r-1+K1)
        ALPHA2r(K1) = STATEV(iALPHA2r-1+K1)
        ALPHA3r(K1) = STATEV(iALPHA3r-1+K1)
        oALPHAr(K1) = STATEV(iALPHAr-1+K1)
      enddo
C     get FLOW vector
      if(dEQPLAS.gt.ZERO) then
        do K1=1,NDI
          FLOW(K1) = dEPLAS(K1)/dEQPLAS
        enddo
        do K1=NDI+1,NTENS
          FLOW(K1) = dEPLAS(K1)/TWO/dEQPLAS
        enddo
      else
        do K1=1,NTENS
          FLOW(K1) = ZERO
        enddo
      endif
C     RM
      RM = STATEV(iRM)
      oRM = RM
C     dALPHAv
      do K1=1, NDI
        dALPHA1v(K1) = (TWO/THREE*C1*dEQPLAS*FLOW(K1) -
     +    GAMMA1*ALPHA1v(K1)*dEQPLAS)/(ONE+GAMMA1*dEQPLAS)
        dALPHA2v(K1) = (TWO/THREE*C2*dEQPLAS*FLOW(K1) -
     +    GAMMA2*ALPHA2v(K1)*dEQPLAS)/(ONE+GAMMA2*dEQPLAS)
        dALPHA3v(K1) = (TWO/THREE*C3*dEQPLAS*FLOW(K1) -
     +    GAMMA3*ALPHA3v(K1)*dEQPLAS)/(ONE+GAMMA3*dEQPLAS)
        ALPHAv(K1) = (ALPHA1v(K1)+dALPHA1v(K1)) +
     +    (ALPHA2v(K1)+dALPHA2v(K1)) + (ALPHA3v(K1)+dALPHA3v(K1))
        !dALPHAv(K1) = ALPHAv(K1)-oALPHAv(K1)
        dALPHAv(K1) = dALPHA1v(K1) + dALPHA2v(K1) + dALPHA3v(K1)
      enddo
      do K1=NDI+1, NTENS
        dALPHA1v(K1) = (TWO/THREE*C1*dEQPLAS*FLOW(K1) -
     +    GAMMA1*KShear*ALPHA1v(K1)*dEQPLAS)/(ONE+GAMMA1*dEQPLAS)
        dALPHA2v(K1) = (TWO/THREE*C2*dEQPLAS*FLOW(K1) -
     +    GAMMA2*KShear*ALPHA2v(K1)*dEQPLAS)/(ONE+GAMMA2*dEQPLAS)
        dALPHA3v(K1) = (TWO/THREE*C3*dEQPLAS*FLOW(K1) -
     +    GAMMA3*KShear*ALPHA3v(K1)*dEQPLAS)/(ONE+GAMMA3*dEQPLAS)
        ALPHAv(K1) = (ALPHA1v(K1)+dALPHA1v(K1)) +
     +    (ALPHA2v(K1)+dALPHA2v(K1)) + (ALPHA3v(K1)+dALPHA3v(K1))
        !dALPHAv(K1) = ALPHAv(K1)-oALPHAv(K1)
        dALPHAv(K1) = dALPHA1v(K1) + dALPHA2v(K1) + dALPHA3v(K1)
```

```
      enddo
      do K1=1, NTENS
        ALPHA1v(K1) = ALPHA1v(K1) + dALPHA1v(K1)
        ALPHA2v(K1) = ALPHA2v(K1) + dALPHA2v(K1)
        ALPHA3v(K1) = ALPHA3v(K1) + dALPHA3v(K1)
        ALPHAv(K1) = ALPHA1v(K1) + ALPHA2v(K1) + ALPHA3v(K1)
      enddo
C     magALPHAv
      magALPHAv = ZERO
      do K1=1, NDI
        magALPHAv = magALPHAv + ALPHAv(K1)**2
      enddo
      do K1=NDI+1, NTENS
        magALPHAv = magALPHAv + TWO*ALPHAv(K1)**2
      enddo
      magALPHAv = sqrt(THREE/TWO*magALPHAv)
C     G function
      G = magALPHAv - RM
      if(magALPHAv.gt.ZERO) then
        do K1 = 1, NTENS
          DirVec(K1)=ALPHAv(K1)/magALPHAv
        enddo
      else
        do K1 = 1, NTENS
          DirVec(K1) = ZERO
        enddo
      endif
C     double dot product DDP
      DDP = ZERO
      do K1 = 1, NDI
        DDP = DDP+DirVec(K1)*dALPHAv(K1)
      enddo
      do K1 = NDI+1, NTENS
        DDP = DDP+TWO*DirVec(K1)*dALPHAv(K1)
      enddo
C     heaviside function of G
      if (G.gt.ZERO) then
        heavisideG = ONE
      elseif (abs(G).lt.TOLER) then
        heavisideG = ONE/TWO
      else
        heavisideG = ZERO
      endif
C     memory surface RM
      dRM = heavisideG*abs(DDP)
      RM = oRM + dRM
      if (RM.lt.RMmin) then
        RMused = RMmin
      elseif (RM.gt.RMmax) then
        RMused = RMmax
      else
        RMused = RM
      endif
C     RMR
      RMR = STATEV(iRMR)
      oRMR = RMR
```

```
      do K1=1, NDI
        dALPHA1r(K1) = (TWO/THREE*C1*dEQPLAS*FLOW(K1) -
     +    GAMMA1*ALPHA1r(K1)*dEQPLAS)/(ONE+GAMMA1*dEQPLAS)
        dALPHA2r(K1) = (TWO/THREE*C2*dEQPLAS*FLOW(K1) -
     +    GAMMA2*ALPHA2r(K1)*dEQPLAS)/(ONE+GAMMA2*dEQPLAS)
        dALPHA3r(K1) = (TWO/THREE*C3*dEQPLAS*FLOW(K1) -
     +    GAMMA3*ALPHA3r(K1)*dEQPLAS)/(ONE+GAMMA3*dEQPLAS)
        ALPHAr(K1) = (ALPHA1r(K1)+dALPHA1r(K1)) +
     +    (ALPHA2r(K1)+dALPHA2r(K1)) + (ALPHA3r(K1)+dALPHA3r(K1))
        !dALPHAr(K1) = ALPHAr(K1)-oALPHAr(K1)
        dALPHAr(K1) = dALPHA1r(K1) + dALPHA2r(K1) + dALPHA3r(K1)
      enddo
      do K1=NDI+1, NTENS
        dALPHA1r(K1) = (TWO/THREE*C1*dEQPLAS*FLOW(K1) -
     +    GAMMA1*KShear*ALPHA1r(K1)*dEQPLAS)/(ONE+GAMMA1*dEQPLAS)
        dALPHA2r(K1) = (TWO/THREE*C2*dEQPLAS*FLOW(K1) -
     +    GAMMA2*KShear*ALPHA2r(K1)*dEQPLAS)/(ONE+GAMMA2*dEQPLAS)
        dALPHA3r(K1) = (TWO/THREE*C3*dEQPLAS*FLOW(K1) -
     +    GAMMA3*KShear*ALPHA3r(K1)*dEQPLAS)/(ONE+GAMMA3*dEQPLAS)
        ALPHAr(K1) = (ALPHA1r(K1)+dALPHA1r(K1)) +
     +    (ALPHA2r(K1)+dALPHA2r(K1)) + (ALPHA3r(K1)+dALPHA3r(K1))
        !dALPHAr(K1) = ALPHAr(K1)-oALPHAr(K1)
        dALPHAr(K1) = dALPHA1r(K1) + dALPHA2r(K1) + dALPHA3r(K1)
      enddo
      do K1=1, NTENS
        ALPHA1r(K1) = ALPHA1r(K1) + dALPHA1r(K1)
        ALPHA2r(K1) = ALPHA2r(K1) + dALPHA2r(K1)
        ALPHA3r(K1) = ALPHA3r(K1) + dALPHA3r(K1)
        ALPHAr(K1) = ALPHA1r(K1) + ALPHA2r(K1) + ALPHA3r(K1)
      enddo
C     magALPHAr
      magALPHAr = ZERO
      do K1=1, NDI
        magALPHAr = magALPHAr + ALPHAr(K1)**2
      enddo
      do K1=NDI+1, NTENS
        magALPHAr = magALPHAr + TWO*ALPHAr(K1)**2
      enddo
      magALPHAr = sqrt(THREE/TWO*magALPHAr)
C     G function
      G = magALPHAr - RMR
      if(magALPHAr.gt.ZERO) then
        do K1 = 1, NTENS
          DirVecR(K1)=ALPHAr(K1)/magALPHAr
        enddo
      else
        do K1 = 1, NTENS
          DirVecR(K1) = ZERO
        enddo
      endif
C     double dot product DDP
      DDP = ZERO
      do K1 = 1, NDI
        DDP = DDP+DirVecR(K1)*dALPHAr(K1)
      enddo
      do K1 = NDI+1, NTENS
```

```
          DDP = DDP+TWO*DirVecR(K1)*dALPHAr(K1)
        enddo
C       heaviside function of G
        if (G.gt.ZERO) then
          heavisideG = ONE
        elseif (abs(G).lt.TOLER) then
          heavisideG = ONE/TWO
        else
          heavisideG = ZERO
        endif
C       memory surface RMR
        dRMR = heavisideG*abs(DDP)
        RMR = oRMR + dRMR
        if (RMR.lt.RMmin) then
          RMRused = RMmin
        elseif (RMR.gt.RMmax) then
          RMRused = RMmax
        else
          RMRused = RMR
        endif
C       R
        oR = STATEV(iR)
        AR = CR*exp(ER*RMRused)
        dR = AR*((EQPLAS+dEQPLAS)**BR-EQPLAS**BR)
        R = oR + dR;
C       PHIinfty
        PhiInfty = AInfty*RMused**4 + BInfty*RMused**3 +
     +   CInfty*RMused**2 + DInfty*RMused + EInfty
C       Omega
        OMEGA = AOmega+BOmega*(RMused)**-COmega
C       PHIcyc
        oPHIcyc = STATEV(iPHIcyc)
        dPHIcyc = OMEGA*(PhiInfty-oPHIcyc)*DEQPLAS
        PHIcyc = oPHIcyc + dPHIcyc
C       PHI
        PHI = PHI0 + PHIcyc
C       save STATEV
        STATEV(iEQPLAS) = EQPLAS
        do K1=1,NTENS
          STATEV(iEPLAS-1+K1) = EPLAS(K1)
          STATEV(iALPHA1v-1+K1) = ALPHA1v(K1)
          STATEV(iALPHA2v-1+K1) = ALPHA2v(K1)
          STATEV(iALPHA3v-1+K1) = ALPHA3v(K1)
          STATEV(iALPHAv-1+K1) = ALPHAv(K1)
          STATEV(iALPHA1r-1+K1) = ALPHA1r(K1)
          STATEV(iALPHA2r-1+K1) = ALPHA2r(K1)
          STATEV(iALPHA3r-1+K1) = ALPHA3r(K1)
          STATEV(iALPHAr-1+K1) = ALPHAr(K1)
          STATEV(120+K1) = dALPHAv(K1)
        enddo
        STATEV(iR) = R
        STATEV(iRM) = RM
        STATEV(iRMR) = RMR
        STATEV(iRMused) = RMused
        STATEV(iRMRused) = RMRused
        STATEV(iPHIcyc) = PHIcyc
```

```
      STATEV(iPHI) = PHI
      STATEV(iPhiInfty) = PhiInfty

      STATEV(127) = SYIELD+R
      STATEV(128) = DDP
C     FIELD(1)
      FIELD(1) = SYIELD+R
      STATEV(iFIELD1) = FIELD(1)
C     FIELD(2)
      FIELD(2) = PHI
      STATEV(iFIELD2) = FIELD(2)
      RETURN
      END
```

Material Parameters Definition in the Abaqus Input File [A2]

The example of material parameters definition in Abaqus input file:

```
*Material, name=Material-1
*Depvar
     128
*Elastic
210000.0,0.3
*Plastic, dependencies=2, hardening=COMBINED, datatype=PARAMETERS,
number backstresses=3
** Material data as a function of FIELD1 and FIELD2 follows:
SYIELD, C1, GAMMA1, C2, GAMMA2, C3, GAMMA3, FIDEL1, FIELD2
```

In the last material data line, the numeric values of material parameters are written. The material data line repeats for different values of variables $FIELD1$ and $FIELD2$. Variables definitions are: $SYIELD = Y$, $C1 = C_1$, $GAMMA1 = \phi \cdot \gamma_1$, $C2 = C_2$, $GAMMA2 = \phi \cdot \gamma_2$, $C3 = C_3$, $GAMMA3 = \phi \cdot \gamma_3$, $FIELD1 = Y$, $FIELD2 = \phi$. So, for presented material model, few material data lines can look like this:

```
** Material data as a function of FIELD1 and FIELD2 follows:
** ...
250.0,63399.70889,222.83539,9999.77788,1367.02686,2000.0,0.0,250.0,1.5
150.0,63399.70889,237.69108,9999.77788,1458.16199,2000.0,0.0,150.0,1.6
151.0,63399.70889,237.69108,9999.77788,1458.16199,2000.0,0.0,151.0,1.6
** ...
```

Chapter 9

Main Results

9.1 Introduction

In this part of the thesis, the results of FE simulations are presented. The experimental program presented in Chapter 3 has been completely simulated using the material model proposed in this thesis. The FE simulation results are compared with the experimental results and also with FE simulation results of the original model [A1]. The error between the prediction of both models and experimental results is quantified.

9.2 FE Simulation Results

The error between the experiment and the FE simulation in each cycle N is calculated simply as

$$Error = \frac{F_a^{exp} - F_a^{sim}}{F_a^{exp}} \cdot 100\,\% \tag{9.1}$$

The mean error and the total error are calculated using equations (7.3) and (7.4) considering the corresponding number of specimens in the series.

The Figures 9.1 and 9.2 and Table 9.1 show the experimental and simulation results of E9 geometry series representing the uniaxial loading conditions. The prediction capability of these two models is comparable. Results have been published in [A1] and [A2].

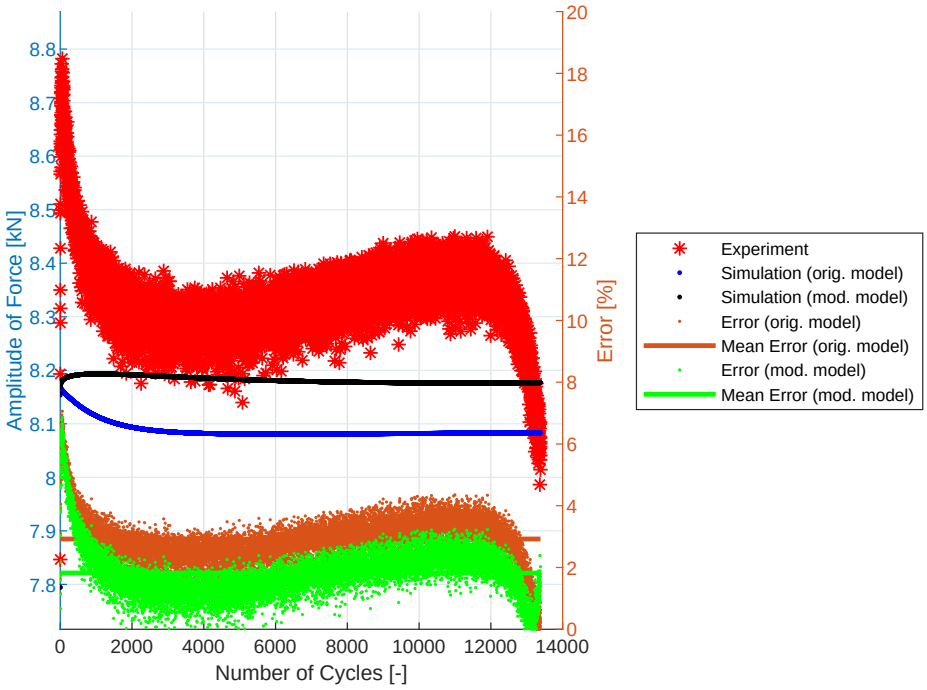

Figure 9.1: Experiment vs. simulations, specimen E9-1. [A1], [A2]

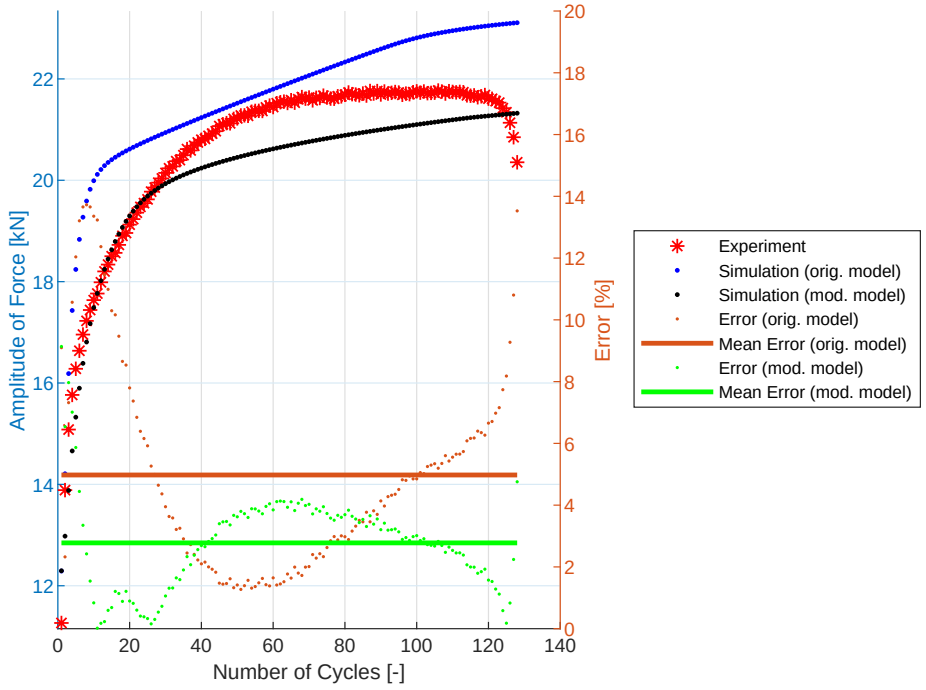

Figure 9.2: Experiment vs. simulations, specimen E9-17. [A1], [A2]

Table 9.1: Mean error of all E9 specimens tested - experiment vs. simulations. [A1], [A2].

Specimen Name	**Orig. Model Mean Err. [%]**	**Mod. Model Mean Err. [%]**
E9-1	2.9226	1.8207
E9-2	2.3311	1.2756
E9-3	2.4027	1.1938
E9-4	1.6977	0.7773
E9-5	8.0687	7.0447
E9-6	8.8658	7.4521
E9-7	11.7310	10.4229
E9-8	3.8241	3.9171
E9-9	9.8245	9.5508
E9-10	7.8144	8.8757
E9-11	2.5028	3.9003
E9-12	4.3523	6.5915
E9-13	4.0929	3.4343
E9-14	2.1610	3.8515
E9-15	2.9195	2.9485
E9-16	1.8601	2.7524
E9-17	4.9766	2.7579

The NT geometry series results are shown in Figures 9.3 and 9.4 and Table 9.2. In this case, the compared variables are the amplitudes of the torque measured during the experiment ($T_{a\ exp}$) and the amplitudes computed by the FE simulations ($T_{a\ sim}$). The errors are calculated using the equations (7.2-7.4). For this geometry, the difference in the prediction capability of the original model and the modified model is not the same - the modified model provides a better prediction of the cyclic hardening of the material under torsional loading for higher loading levels. The results have been published in [A2].

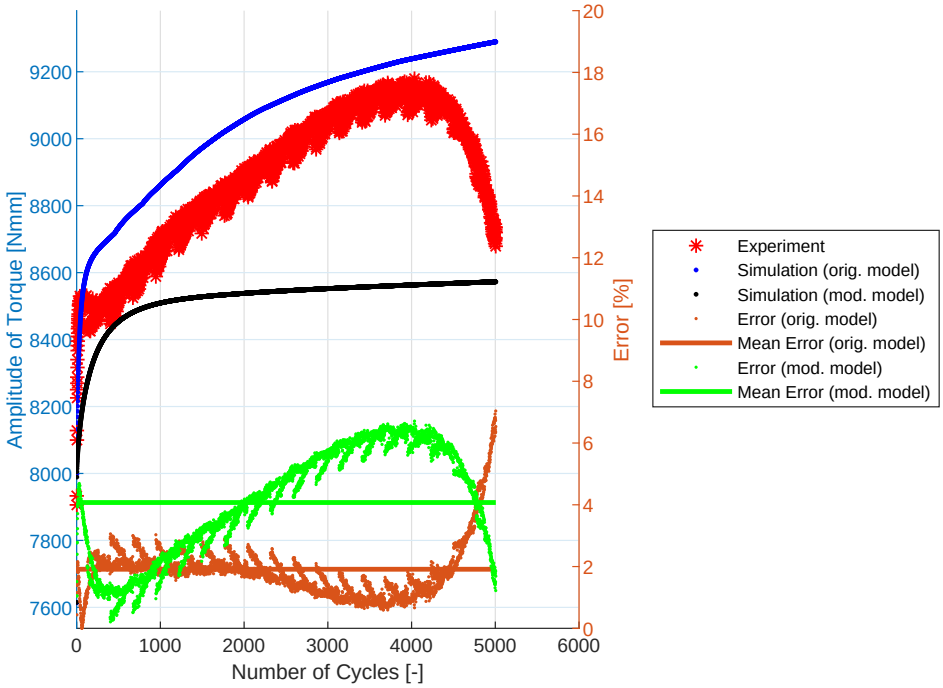

Figure 9.3: Experiment vs. simulations, specimen NT-1. [A2]

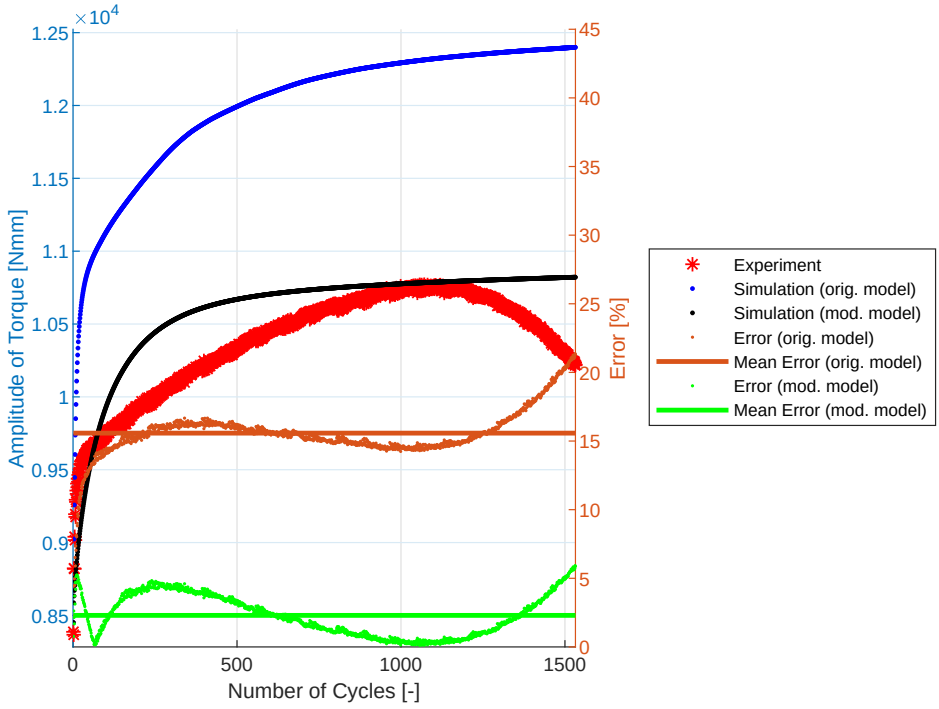

Figure 9.4: Experiment vs. simulations, specimen NT-6. [A2]

Table 9.2: Mean error of all NT specimens tested - experiment vs. simulations. [A2]

Specimen Name	**Orig. Model Mean Err. [%]**	**Mod. Model Mean Err. [%]**
NT-1	1.9100	4.0682
NT-2	0.8367	5.9823
NT-3	11.2048	1.3797
NT-4	11.1021	1.0934
NT-5	14.2137	1.3947
NT-6	15.5549	2.2815
NT-7	13.1168	1.5014
NT-8	8.8054	4.7887

Finally, the notched specimen geometry series R1.2, R2.5, and R5 are shown in Figures 9.5, 9.6, 9.7, 9.8, 9.9, and 9.10 and Tables 9.3, 9.4, and 9.5. The stress field in the cross-section of these specimens is no longer uniaxial, for more details see [A10], where the simulations of stress field in notched specimens has been presented. The prediction capabilities of both models are also comparable, the results have been published in [A2].

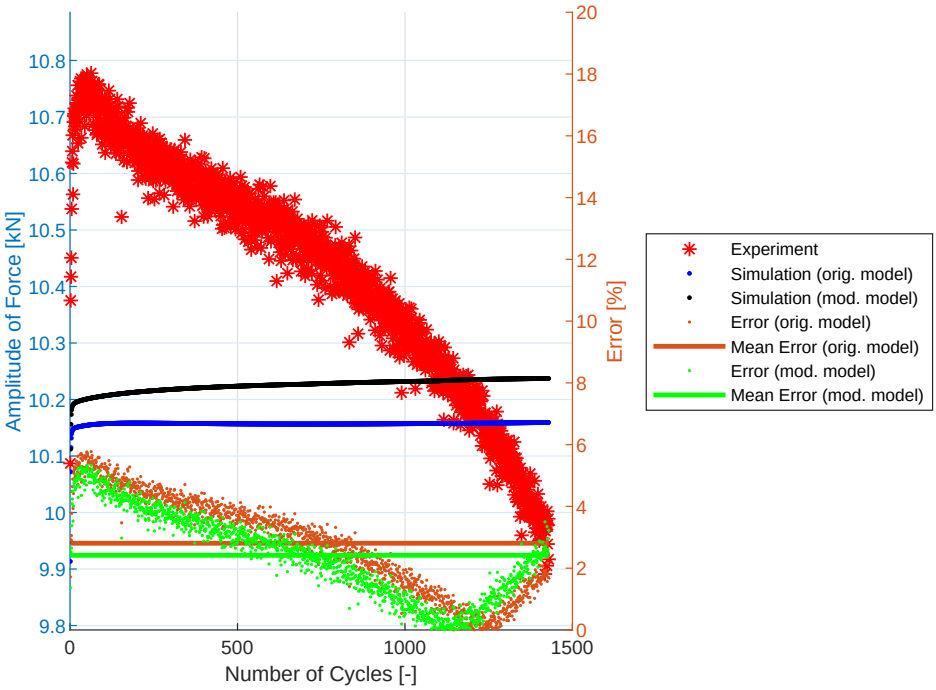

Figure 9.5: Experiment vs. simulations, specimen R1.2-1. [A2]

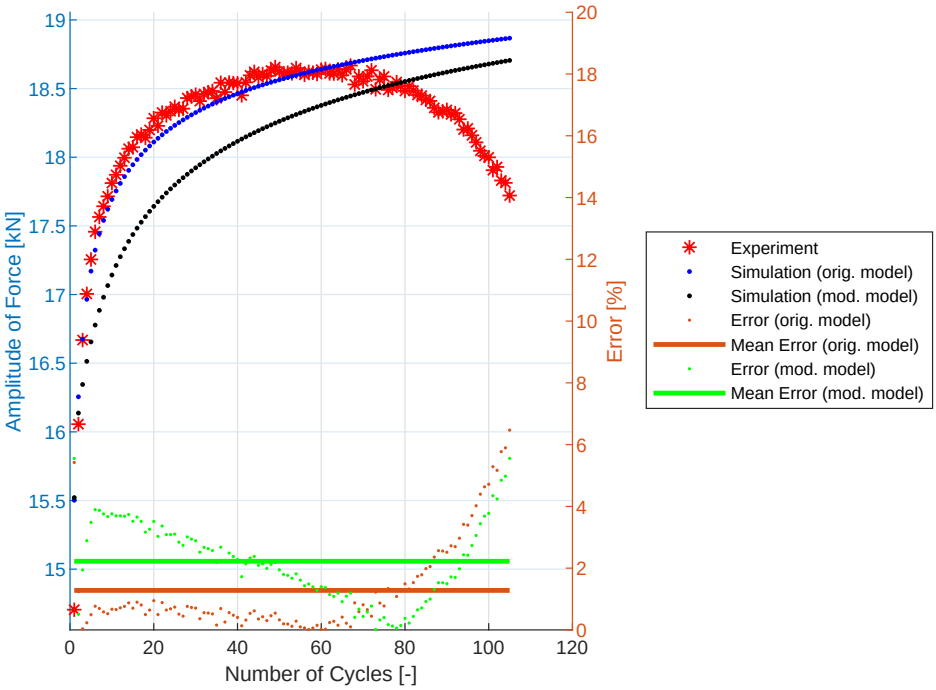

Figure 9.6: Experiment vs. simulations, specimen R1.2-18. [A2]

Table 9.3: Mean error of all R1.2 specimens tested - experiment vs. simulations. [A2]

Specimen Name	**Orig. Model Mean Err. [%]**	**Mod. Model Mean Err. [%]**
R1.2-1	2.8075	2.4172
R1.2-2	3.7011	3.1679
R1.2-3	2.2438	2.2027
R1.2-4	2.8530	2.7056
R1.2-5	2.8984	2.7105
R1.2-6	4.7877	4.4405
R1.2-7	1.4888	1.4897
R1.2-8	7.1382	6.7943
R1.2-9	2.4171	2.2355
R1.2-10	1.6518	1.7538
R1.2-11	2.0827	2.2332
R1.2-12	3.9411	3.2028
R1.2-13	2.5308	3.1540
R1.2-14	1.4521	1.8444
R1.2-15	3.6781	2.6435
R1.2-16	1.5820	1.9106
R1.2-17	1.6089	2.5930
R1.2-18	1.2789	2.2219

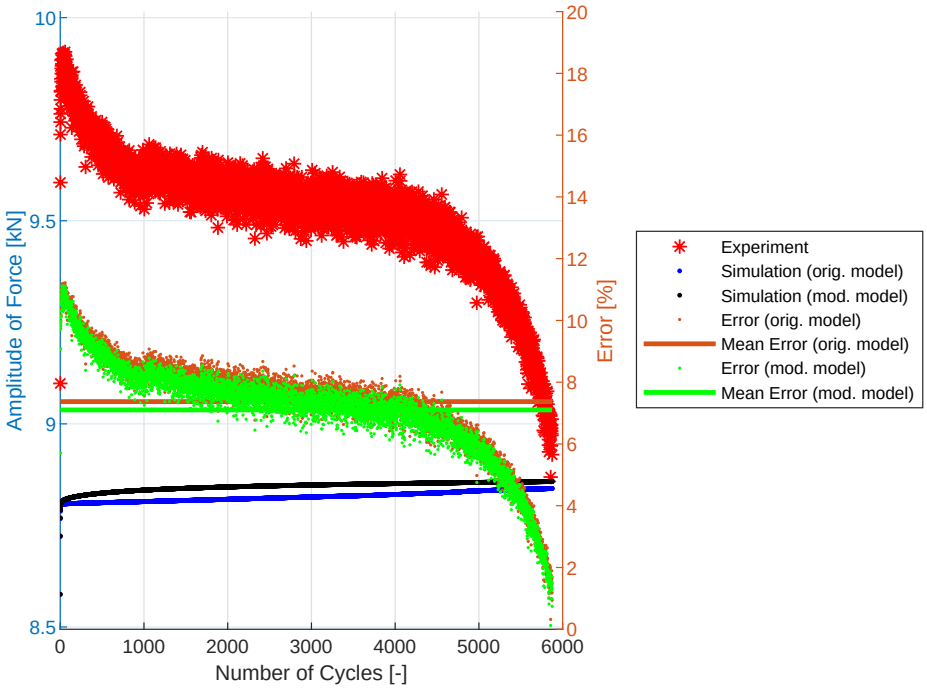

Figure 9.7: Experiment vs. simulations, specimen R2.5-1. [A2]

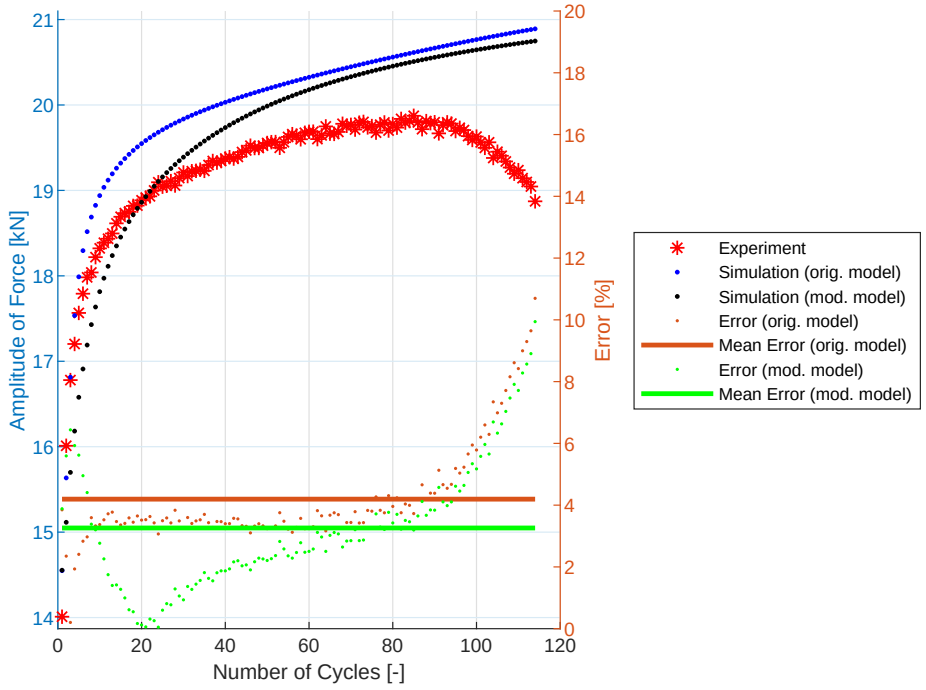

Figure 9.8: Experiment vs. simulations, specimen R2.5-21. [A2]

Table 9.4: Mean error of all R2.5 specimens tested - experiment vs. simulations. [A2]

Specimen Name	Orig. Model Mean Err. [%]	Mod. Model Mean Err. [%]
R2.5-1	7.3714	7.1025
R2.5-2	8.1586	7.6327
R2.5-3	9.1468	8.6587
R2.5-4	6.8139	6.8130
R2.5-5	6.6714	6.6118
R2.5-6	9.9838	9.1708
R2.5-7	4.3249	3.4860
R2.5-8	3.8551	3.8250
R2.5-9	1.0034	0.9027
R2.5-10	4.7921	4.9816
R2.5-11	1.9673	2.1464
R2.5-12	2.1944	1.6489
R2.5-13	1.2466	1.0057
R2.5-14	8.7778	9.1473
R2.5-15	2.6624	3.0678
R2.5-16	1.4643	1.3563
R2.5-17	0.9873	1.5697
R2.5-18	1.4020	1.4515
R2.5-19	1.6099	2.6423
R2.5-20	0.9634	2.4069
R2.5-21	4.1944	3.2605

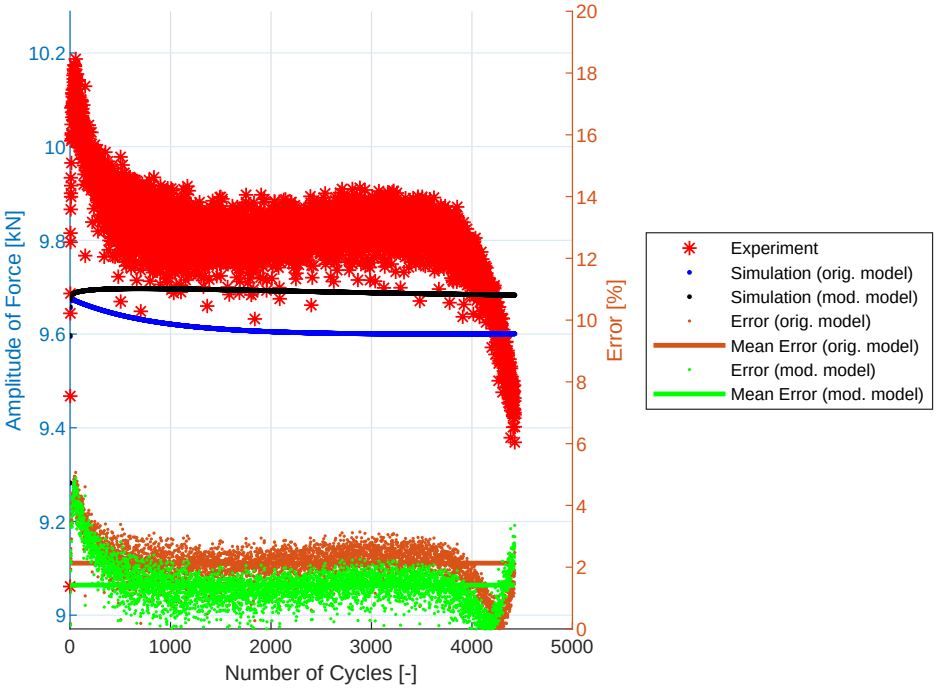

Figure 9.9: Experiment vs. simulations, specimen R5-1. [A2]

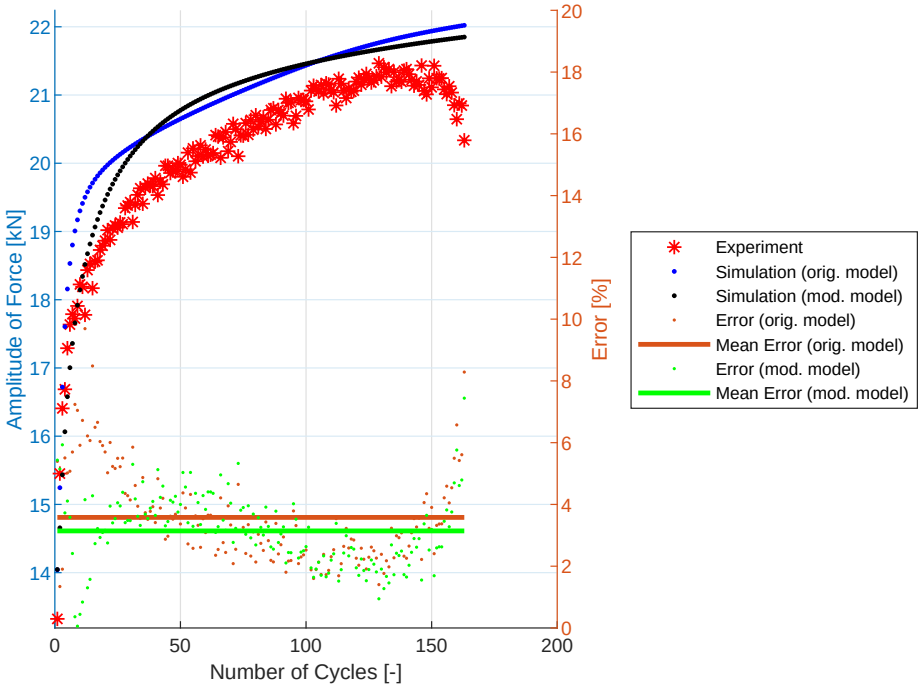

Figure 9.10: Experiment vs. simulations, specimen R5-24. [A2]

Table 9.5: Mean error of all R5 specimens tested - experiment vs. simulations. [A2]

Specimen Name	**Orig. Model Mean Err. [%]**	**Mod. Model Mean Err. [%]**
R5-1	2.1303	1.4186
R5-2	2.0673	1.8112
R5-3	0.7021	0.8284
R5-4	0.9757	0.9284
R5-5	1.4847	1.4209
R5-6	1.7435	1.6993
R5-7	2.9066	2.7548
R5-8	5.3372	5.4106
R5-9	4.9004	4.5530
R5-10	2.3623	2.6227
R5-11	7.0110	6.8065
R5-12	2.3912	3.1025
R5-13	6.7479	6.8700
R5-14	5.1055	5.4414
R5-15	1.3043	1.4251
R5-16	1.1829	1.3661
R5-17	3.6903	3.6048
R5-18	3.1399	2.9518
R5-19	6.1649	6.1226
R5-20	2.8263	2.6683
R5-21	1.0485	1.2882
R5-22	8.2167	7.6119
R5-23	2.2011	1.6441
R5-24	3.5803	3.1425

Chapter 10

Outcomes

10.1 Theoretical Outcomes

The new material model, proposed in Section 6.3, is capable of capturing strain-range dependent hardening for uniaxial and newly also for torsional loading conditions. The proposed modification shows one of the possible ways to deal with the anisotropy between tension and torsion of the memory surface-based models.

The analysis of the original model presented in Section 6.2 shows in general how to identify suitable parts of the original model that do not properly reflect the observed response of the material.

The proposed material identification process, presented in Chapter 7, shows the new, unorthodox way to identify material parameters using the incremental FEA-like simulations of material response and multiple optimization procedure to fit the material parameters as precisely as possible. The identification process is also published in [A1], [A2], [A3] and [A7].

The complete results of the experimental LCF program are presented in the extensive form in Chapter 9 and in Appendix B and most of the data are also published in [A1] and [A2].

The implementation of the proposed model (presented in Chapter 8) is in the form of the Abaqus FE software user-defined field (USDFLD) subroutine. The full Fortran code of the subroutine is presented in section 8.2.3 and is also published in [A2]. This will eventually allow other researchers to effectively modify or extend the proposed model and speed up the development of functional FE code.

10.2 Practical Outcomes

The new material model presented in the thesis is implemented into the commercial FE software Abaqus as the USDFLD subroutine. The implementation is described in Chapter 8 and also published in [A1] and [A2], the full Fortran code of the USDFLD subroutine is presented in section 8.2.3 and also published in [A2]. This allows potential users to test the proposed material model for real engineering computations, as has been demonstrated for example in [A6]. Compared with more commonly used Abaqus user material (UMAT) subroutine, the use of the USDLFD subroutine has several advantages. It uses the Abaqus default Chaboche plasticity

model computational core, which is optimized for a high computation speed and is noticeably faster than UMAT. USDFLD does not require a definition of consistent tangent modulus, which is, for a quite complex model like this one, complicated to derive. An adjustment of constitutive equations may lead to the need to re-derive the consistent tangent modulus. The disadvantage of the USDFLD subroutine is that the FIELD variables (for example, the actual size of yield surface) are constant during the computational increment, so the increment size must be chosen with caution using sensitivity study.

The material parameters identification process is described step by step in Chapter 7 and also published in [A1], [A2], [A4] and [A9]. Using the procedure, material parameters can be identified for other materials. The values of material parameters for 08Ch18N10T austenitic stainless steel are presented in Table 7.1.

Combination of presented USDFLD subroutine with material parameters for 08Ch18N10T steel, the newly proposed material model is ready for testing for engineering computations on real components.

The use of the proposed model is currently limited to the conditions for which it was developed and tested. These conditions are uniaxial loading (including non-uniaxial stress-strain field in case of notched specimens) and torsional loading (dominant shear stress-strain). The model has not been tested for combined loading conditions, for example for the proportional or non-proportional combination of tension and torsion.

Chapter 11

Conclusion and Future Work

11.1 Conclusion

In this thesis, the original material model of cyclic plasticity with strain-range dependency published in [A1] is presented in Chapter 6. The constitutive equations are analyzed, the isotropic hardening part of the model and the definition of memory surface are chosen as parts of the original model to be modified.

The fulfillment of the main objectives of the thesis, defined in Chapter 4, is summed up here:

1. **Proposition of modification:**

   The new formulation of the material model is proposed in section 6.3 and is also published in [A2]. The new formulation of isotropic hardening as a nonlinear function of accumulated plastic strain p is proposed. The original memory surface is newly split into two memory surfaces - the memory surface for isotropic hardening, which is defined in the same way as the original one, and the memory surface for kinematic hardening, which is defined by the new constitutive equations. The new memory surface limits are defined.

2. **Calibration of material parameters:**

   The new calibration procedure of material parameters is proposed in this thesis. It uses the incremental FEA-like simulations of material response for fitting material parameters and multiple optimization procedure to fit the material parameters as precisely as possible. The material parameters identification process of newly proposed model is described step by step in Chapter 7 and is also published in [A1], [A2], [A3] and [A7]. Material parameters are identified for 08Ch18N10T austenitic stainless steel.

3. **Implementation into FE:**

   The implementation of the newly proposed model into FE code is described in 8 and also published in [A2]. The implementation into commercial FE software Abaqus is in the form of the user-defined field subroutine (USDFLD) written in Fortran programming language.

The experimental program presented in Chapter 3 is completely simulated using the newly proposed model. The prediction capability of the newly proposed model and the comparison with the original one are presented in Chapter 9 and are also published in [A2]. The newly proposed model shows practically the same prediction capability as the original for uniaxial and notched specimens, but significantly better prediction capability under torsional loading.

11.2 Future Work

The presented material model extends the good prediction capabilities of the original model [A1] from uniaxial to torsional loading. The dominant tensile or torsional loading is also the limitation of model usability in the proposed form. The next logical step is to verify the proposed model for combined loading conditions, for example, a proportional combination of tension and torsion and possibly propose another modification to include these loading conditions.

After handling the proportional loading conditions, the non-proportional loading conditions are then the next step which is slowly approaching to the final goal of material response modeling - general loading conditions.

References

[1] Lemaitre, J. and Desmorat, R. *Engineering Damage Mechanics*. Springer (2005). ISBN 3-540-21503-4.

[2] Chaboche, J. L. A review of some plasticity and viscoplasticity constitutive theories. *International Journal of Plasticity*, 24(10):1642–1693 (2008). doi: 10.1016/j.ijplas.2008.03.009.

[3] Liu, R., Zhang, Z. J., Zhang, P., and Zhang, Z. F. Extremely-low-cycle fatigue behaviors of Cu and Cu–Al alloys: Damage mechanisms and life prediction. *Acta Materialia*, 83:341–356 (2015). doi:10.1016/j.actamat.2014.10.002.

[4] L., X. A unified expression for low cycle fatigue and extremely low cycle fatigue and its implication for monotonic loading. *International Journal of Fatigue*, 30:1691–1698 (2008). doi:10.1016/j.ijfatigue.2008.03.004.

[5] Kuroda, M. Extremely low cycle fatigue life prediction based on a new cumulative fatigue damage model. *International Journal of Fatigue*, 24(6):699–703 (2002).

[6] Pereira, J. C. R., de Jesus, A. M. P., Xavier, J., and Fernandes, A. A. Ultra low-cycle fatigue behaviour of a structural steel. *Engineering Structures*, 60:214–222 (2014).

[7] Park, Y. S., J., P. S., Iwai, S., and Kang, S. H. Failure and damage of steel thin-plate elements and angle members due to very-low-cycle loading. *Engineering Structures*, 26:1623–1632 (2004).

[8] Ye, D., Matsuoka, S., Nagashima, N., and Suzuki, N. The low-cycle fatigue, deformation and final fracture behavior of an austenitic stainless steel. *Mat. Scienece and Engineering*, 415:104–117 (2006).

[9] Dunne, F. and Petrinic, N. *Introduction to Computational Plasticity*. Oxford University Press (2005). ISBN 0-19-856826-6.

[10] Halama, R. Experimentální poznatky a fenomenologické modelování cyklické plasticity kovů. *Habilitační práce, VŠB – Technická univerzita Ostrava, Fakulta strojní* (2009).

[11] *ABAQUS/Standard User's Manual, Version 6.14*. Dassault Systèmes Simulia Corp, United States (2014).

[12] Prager, W. A New Method of Analysing Stresses and Strains in Work Hardening Plastic Solids. *Journal of Applied Mechanics*, 23:493–496 (1956).

[13] Armstrong, P. J. and Frederick, C. O. A Mathematical Representation of the Multiaxial Bauschinger Effect. *G.E.G.B. Report RD/B/N*, 731 (1966).

[14] Chaboche, J. L., Dang, V. K., and Cordier, G. Modelization of the Strain Memory Effect on the Cyclic Hardening of 316 Stainless Steel. *Proceedings of the 5th International Conference on Structural Mechanics in Reactor Technology, Berlin*, pages 1–10 (1979).

[15] Marquis, D. Modélisation et identification de l'écrouissage anisotrope des métaux. *Thése de 3éme cycle, Université Paris 6, France.* (1979).

[16] Ohno, N. A constitutive model of cyclic plasticity with a nonhardening strain region. *Journal of Applied Mechanics*, 49:721–727 (1982).

[17] Krishna, S., Hassan, T., Naceur, I., Saï, K., and Cailletaud, G. Macro versus micro-scale constitutive models in simulating proportional and nonproportional cyclic and ratcheting responses of stainless steel 304. *International Journal of Plasticity*, 25:1910–1949 (2009). doi:10.1016/j.ijplas.2008.12.009.

[18] Hassan, T., Taleb, L., and Krishna, S. Influence of non-proportional loading on ratcheting responses and simulations by two recent cyclic plasticity models. *International Journal of Plasticity*, 24:1863–1889 (2008).

[19] Chaboche, J. L. On some modifications of kinematic hardening to improve the description of ratcheting effects. *International Journal of Plasticity*, 7:661–678 (1991).

[20] Khutia, N., Dey, P. P., Sivaprasad, S., and Tarafder, S. Development of new cyclic plasticity model for 304LN stainless steel through simulation and experimental investigation. *Mechanics of Materials*, 78:85–101 (2014).

[21] Jiang, Y. and Sehitoglu, H. Modeling of cyclic ratchetting plasticity, part I: Development of constitutive relations. *Journal of Applied Mechanics*, 63:720–725 (1996).

[22] Halama, R., Sedlák, J., and Šofer. M. Phenomenological Modelling of Cyclic Plasticity. *Numerical Modelling Miidla, Miidla, P., Ed.; IntechOpen: London, UK*, pages 329–354 (2012).

[23] Kopas, P., Saga, M., Baniari, V., Vasko, M., and Handrik, M. A plastic strain and stress analysis of bending and torsion fatigue specimens in the low-cycle fatigue region using the finite element methods. *Procedia Engineering*, 177:526–531 (2017).

[24] Chen, X., Chen, X., Yu, D., and Gao, B. Recent progresses in experimental investigation and finite element analysis of ratcheting in pressurized piping. *International Journal of Pressure Vessels and Piping*, 101:113–142 (2013). doi: https://doi.org/10.1016/j.ijpvp.2012.10.008.

[25] Ohno, N. and Wang, J. D. Kinematic Hardening Rules with Critical State of Dynamic Recovery. Part I: Formulation and Basic Features for Ratchetting Behavior. *International Journal of Plasticity*, 9:375–390 (1993).

[26] Abdel-Karim, M. and Ohno, N. Kinematic hardening model suitable for ratchetting with steady-state. *Internation Journal of Plasticity*, 16:225–240 (2000).

[27] Halama, R., Fusek, M., Šofer, M., Poruba, Z., Matušek, P., and Fajkoš, R. Ratcheting Behavior of Class C Wheel Steel and Its Prediction by Modified AbdelKarim-Ohno Model. In *roceedings of the 10th International Conference on Contact Mechanics CM2015*. Colorado Springs, Colorado, USA (2015).

[28] Feigenbaum, H. P. and Dafalias, Y. F. Directional distortional hardening in metal plasticity within thermodynamics. *International Journal of Solids and Structures*, 44:7526–7542 (2007).

[29] Parma, S., Plešek, J., Marek, R., Hrubý, Z., Feigenbaum, H. P., and Dafalias, Y. F. Calibration of a simple directional distortional hardening model for metal plasticity. *International Journal of Solids and Structures*, 143:113–124 (2018).

[30] Sung, S. J., Liu, L. W., Hong, H. K., and Wu, H. C. Evolution of yield surface in the 2D and 3D stress spaces. *International Journal of Solids and Structures*, 48:1054–1069 (2011).

[31] Halama, R., Fojtík, F., and Markopoulos, A. Memorization and Other Transient Effects of ST52 Steel and Its FE Description. *Applied Mechanics and Materials*, 486:48–53 (2003).

[32] Kang, G. Z., Ohno, N., and Nebu, A. Constitutive modeling of strain-range dependent cyclic hardening. *International Journal of Plasticity*, 19:1801–1819 (2003).

[33] Schäfer, B. J., Song, X., Sonnweber-Ribic, P., Hassan, H., and Hartmaier, A. Micromechanical Modelling of the Cyclic Deformation Behavior of Martensitic SAE 4150—A Comparison of Different Kinematic Hardening Models. *Metals*, 9:368 (2019).

[34] Moeini, G., Ramazani, A., Myslicki, S., Sundararaghavan, V., and Könke, C. Low Cycle Fatigue Behaviour of DP Steels: Micromechanical Modelling vs. Validation. *Metals*, 7:265 (2017).

[35] Msolli, S. Thermoelastoviscoplastic modeling of RAFM steel JLF-1 using tensile and low cycle fatigue experiments. *Journal of Nuclear Materials*, 451:336–345 (2014).

[36] Ji, S., Liu, C., Li, Y., Shi, S., and Chen, X. Effect of torsional pre-strain on low cycle fatigue performance of 304 stainless steel. *Materials Science and Engineering*, 746:50–57 (2019).

[37] Kang, G., Li, Y., and Gao, Q. Non-proportionally multiaxial ratcheting of cyclic hardening materials at elevated temperatures: Experiments and simulations. *Mechanics of Materials*, 37:1101–1118 (2005).

[38] Kang, G., Gao, Q., and Yang, X. A visco–plastic constitutive model incorporated with cyclic hardening for uniaxial/multiaxial ratcheting of SS304 stainless steel at room temperature. *Mechanics of Materials*, 34:521–531 (2002).

[39] Metallic materials - Tensile testing - Part 1: Method of test at room temperature. Standard, International Organization for Standardization, CH-1214 Vernier, Geneva, Switzerland (2016).

[40] Chaboche, J. L. and Lemaitre, J. *Mechanics of Solid Materials*. Cambridge University Press, Cambridge (1990).

[41] Bari, S. and Hassan, T. Anatomy of Coupled Constitutive Models for Ratcheting Simulations. *Internation Journal of Plasticity*, 16:381–409 (2000).

[42] Khutia, N., Dey, P. P., Paul, S. K., and Tarafder, S. Development of non Masing characteristic model for LCF and ratcheting fatigue simulation of SA333 C–Mn steel. *Mechanics of Materials*, 65:88–102 (2013).

[43] Standard Practise for Strain-Controlled Fatigue Testing. Standard, ASTM International, West Conshohocken, PA, USA (1998).

[44] Halama, R., Markopoulos, A., Jančo, R., and Bartecký, M. Implementation of MAKOC Cyclic Plasticity Model with Memory. *Advances in Engineering Software*, 113:34–46 (2018).

Publications and Other Achievements of the Author Related to Topic of the Thesis

Published Papers

[A1] Halama, R., Fumfera, J., Gál, P., Kumar, T., Markopoulos, A. Modeling the Strain-Range Dependent Cyclic Hardening of SS304 and 08Ch18N10T Stainless Steel with a Memory Surface. *Metals*, 9(832):1-26 (2019).

[A2] Fumfera, J., Halama, R., Procházka, R., Gál, P., Španiel, M. Strain Range Dependent Cyclic Hardening of 08Ch18N10T Stainless Steel—Experiments and Simulations. *Materials*, 12(4243):1-28 (2019).

Conference Contributions

[A3] Fumfera, J., Halama, R., Kuželka, J., Španiel, M. Strain-Range Dependent Cyclic Plasticity Material Model Calibration for the 08Ch18N10T Steel. In: *Proceedings of the 33rd conference with international participation on Computational Mechanics 2017*. Pilsen: University of West Bohemia, p. 25-26, (2017). ISBN 978-80-261-0748-4.

[A4] Fumfera, J., Džugan, J., Kuželka, J., Procházka, R., Španiel, M. Strain-amplitude Dependent Cyclic Hardening of 08Ch18N10T Austenitic Stainless Steel. In: *4th International Conference Recent Trends in Structural Materials, COMAT 2016*. London: Institute of Physics Publishing, IOP Conference Series: Materials Science and Engineering. vol. 179 (2017). ISSN 1757-8981.

[A5] Fumfera, J., Procházka, R. Specimen design for low-cycle fatigue experiments under large strain amplitude loading. In: *Experimental Stress Analysis 2016*. Plzeň: Západočeská universita, Fakulta aplikovaných věd, (2016). ISBN 978-80-261-0624-1.

Research Reports

[A6] Fumfera, J., Kuželka, J., Španiel, M. *Simulace zatížení příruby.* 12105/17/35. [Research report]. Prague: Czech Technical University in Prague, Faculty of Mechanical Engineering, (2017). [in Czech].

[A7] Fumfera, J., Kuželka, J., Španiel, M. *Popis programového skriptu pro identifikaci parametrů Halamova modelu cyklické plasticity.* 12105/17/34. [Research report]. Prague: Czech Technical University in Prague, Faculty of Mechanical Engineering, (2017). [in Czech].

[A8] Fumfera, J., Kuželka, J., Španiel, M. *Určení deformace vzorků.* 12105/17/11. [Research report]. Prague: Czech Technical University in Prague, Faculty of Mechanical Engineering, (2017). [in Czech].

[A9] Fumfera, J., Kuželka, J., Španiel, M. *Materiálový model cyklické plasticity s cyklickým zpevněním závislým na hladině zatížení a jeho kalibrace.* 12105/17/10. [Research report]. Prague: Czech Technical University in Prague, Faculty of Mechanical Engineering, (2017). [in Czech].

[A10] Fumfera, J. *Návrh parametrů zatěžování pro vrubované vzorky.* 12105/15/17. [Research report]. Prague: Czech Technical University in Prague, Faculty of Mechanical Engineering, (2015). [in Czech].

[A11] Fumfera, J. *Návrh vzorků a parametrů zatěžování.* 12105/15/02. [Research report]. Prague: Czech Technical University in Prague, Faculty of Mechanical Engineering, (2015). [in Czech].

Software

[A12] Kuželka, J., Fumfera, J., Džugan, J., Petruška, J., Lopaur, J., Hůlka, J. Plugin pro hodnocení a identifikaci cyklické plasticity kovových materiálů. [Software]. (2015).

Appendix A

Boundary Conditions of Simulations

In this appendix, boundary conditions of all specimens tested are presented. These data have been published in [A2].

Table A.1: Boundary conditions of IDF specimens. [A2]

Specimen name	**Geometry type**	$\boldsymbol{\Delta L_{ext}}$ **[mm]**	$\boldsymbol{N_d}$
IDF-1	UG	0.030	37509
IDF-2	UG	0.050	4285
IDF-3	UG	0.075	916
IDF-4	UG	0.100	580
IDF-5	UG	0.125	254
IDF-6	E9	0.132	159
IDF-7	E9	0.154	381
IDF-8	E9	0.176	370
IDF-9	E9	0.198	161
IDF-10	E9	0.245	156
IDF-11	E9	0.264	124
IDF-12	E9	0.353	93

Table A.2: Boundary conditions of E9 specimens. [A2]

Specimen name	**Geometry type**	$\boldsymbol{\Delta L_{ext}}$ **[mm]**	$\boldsymbol{N_d}$
E9-1	E9	0.0447	13382
E9-2	E9	0.0446	15104
E9-3	E9	0.0662	4053
E9-4	E9	0.0662	3887
E9-5	E9	0.0881	1529
E9-6	E9	0.0880	1853
E9-7	E9	0.1100	1158
E9-8	E9	0.1100	631
E9-9	E9	0.1320	748
E9-10	E9	0.1540	546
E9-11	E9	0.1770	406
E9-12	E9	0.1980	332
E9-13	E9	0.2200	253
E9-14	E9	0.2420	181
E9-15	E9	0.2420	195
E9-16	E9	0.2640	220
E9-17	E9	0.3520	128

Table A.3: Boundary conditions of NT specimens. [A2]

Specimen name	**Geometry type**	$\boldsymbol{\Delta\phi_{ext}}$ [°]	$\boldsymbol{N_d}$
NT-1	NT	0.8703	5006
NT-2	NT	0.8694	6894
NT-3	NT	1.1423	2222
NT-4	NT	1.1414	2289
NT-5	NT	1.4031	2045
NT-6	NT	1.3772	1532
NT-7	NT	1.6554	1170
NT-8	NT	2.1492	925

Table A.4: Boundary conditions of R1.2 specimens. [A2]

Specimen name	**Geometry type**	ΔL_{ext} **[mm]**	N_d
R1.2-1	R1.2	0.0245	1429
R1.2-2	R1.2	0.0246	946
R1.2-3	R1.2	0.0326	715
R1.2-4	R1.2	0.0406	523
R1.2-5	R1.2	0.0407	490
R1.2-6	R1.2	0.0489	290
R1.2-7	R1.2	0.0485	356
R1.2-8	R1.2	0.0560	241
R1.2-9	R1.2	0.0563	256
R1.2-10	R1.2	0.0639	134
R1.2-11	R1.2	0.0642	202
R1.2-12	R1.2	0.0721	171
R1.2-13	R1.2	0.0718	164
R1.2-14	R1.2	0.0794	112
R1.2-15	R1.2	0.0868	145
R1.2-16	R1.2	0.0869	114
R1.2-17	R1.2	0.0945	96
R1.2-18	R1.2	0.0944	105

Table A.5: Boundary conditions of R2.5 specimens. [A2]

Specimen name	**Geometry type**	ΔL_{ext} **[mm]**	N_d
R2.5-1	R2.5	0.0228	5875
R2.5-2	R2.5	0.0341	1245
R2.5-3	R2.5	0.0340	1041
R2.5-4	R2.5	0.0454	607
R2.5-5	R2.5	0.0454	761
R2.5-6	R2.5	0.0568	378
R2.5-7	R2.5	0.0567	429
R2.5-8	R2.5	0.0718	242
R2.5-9	R2.5	0.0679	346
R2.5-10	R2.5	0.0794	265
R2.5-11	R2.5	0.0791	212
R2.5-12	R2.5	0.0904	210
R2.5-13	R2.5	0.0903	221
R2.5-14	R2.5	0.1015	205
R2.5-15	R2.5	0.1015	163
R2.5-16	R2.5	0.1126	189
R2.5-17	R2.5	0.1126	156
R2.5-18	R2.5	0.1237	132
R2.5-19	R2.5	0.1237	129
R2.5-20	R2.5	0.1419	106
R2.5-21	R2.5	0.1346	114

Table A.6: Boundary conditions of R5 specimens. [A2]

Specimen name	**Geometry type**	$\boldsymbol{\Delta L_{ext}}$ **[mm]**	$\boldsymbol{N_d}$
R5-1	R5	0.0308	4427
R5-2	R5	0.0461	1700
R5-3	R5	0.0457	1072
R5-4	R5	0.0603	733
R5-5	R5	0.0589	953
R5-6	R5	0.0727	623
R5-7	R5	0.0747	527
R5-8	R5	0.0893	342
R5-9	R5	0.0869	543
R5-10	R5	0.1050	297
R5-12	R5	0.1010	374
R5-13	R5	0.1154	264
R5-14	R5	0.1156	290
R5-15	R5	0.1146	228
R5-16	R5	0.1287	152
R5-17	R5	0.1276	272
R5-18	R5	0.1418	179
R5-19	R5	0.1467	155
R5-20	R5	0.1403	177
R5-21	R5	0.1540	163
R5-22	R5	0.1531	174
R5-23	R5	0.1663	144
R5-24	R5	0.1685	189
R5-25	R5	0.1652	163

Appendix B

Remaining Results of Simulations

In this appendix, remaining results of simulations of proposed model are presented in the graphical form. The following figures show the amplitude of loading (force or torque) of the experiment and simulations for both presented model - the original and the modified one. Error of both models between both simulations and the experiment is also presented in the figure.

B.1 E9 Geometry

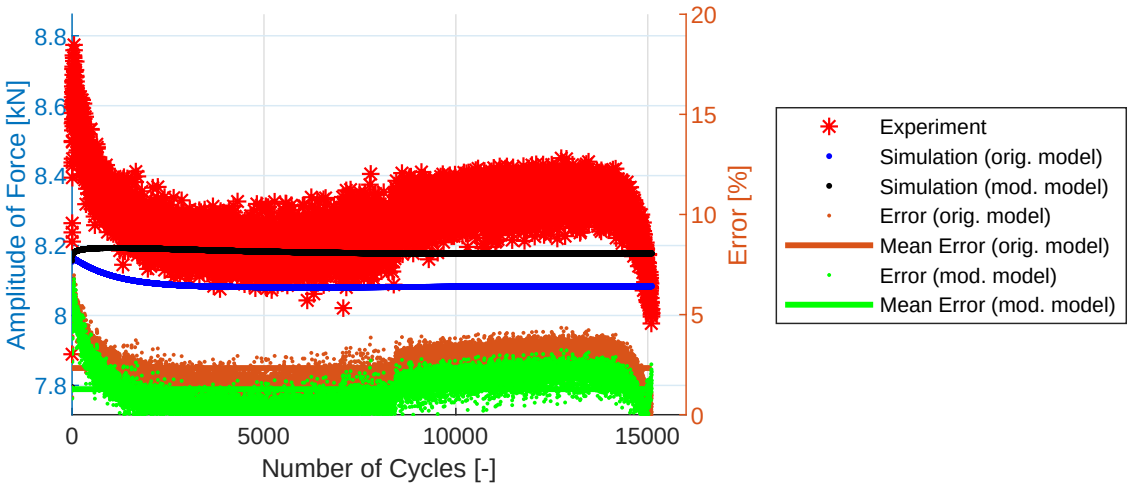

Figure B.1: Experiment vs. simulations, specimen E9-2. [A1]

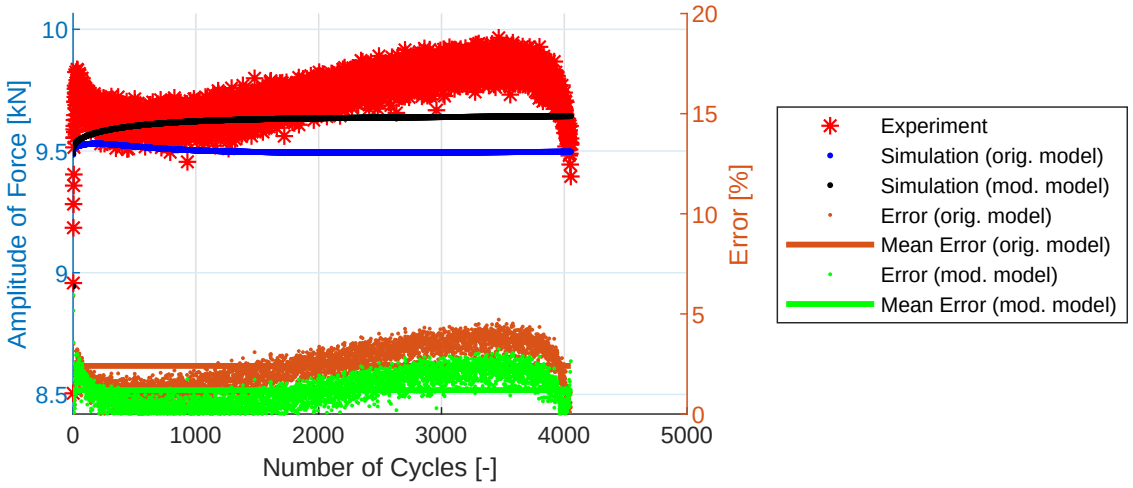

Figure B.2: Experiment vs. simulations, specimen E9-3. [A1]

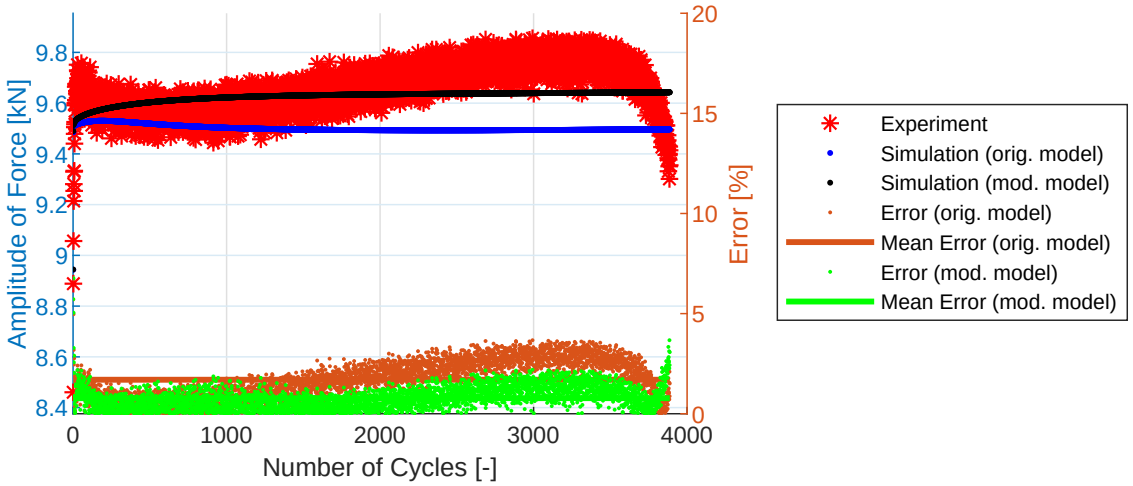

Figure B.3: Experiment vs. simulations, specimen E9-4. [A1]

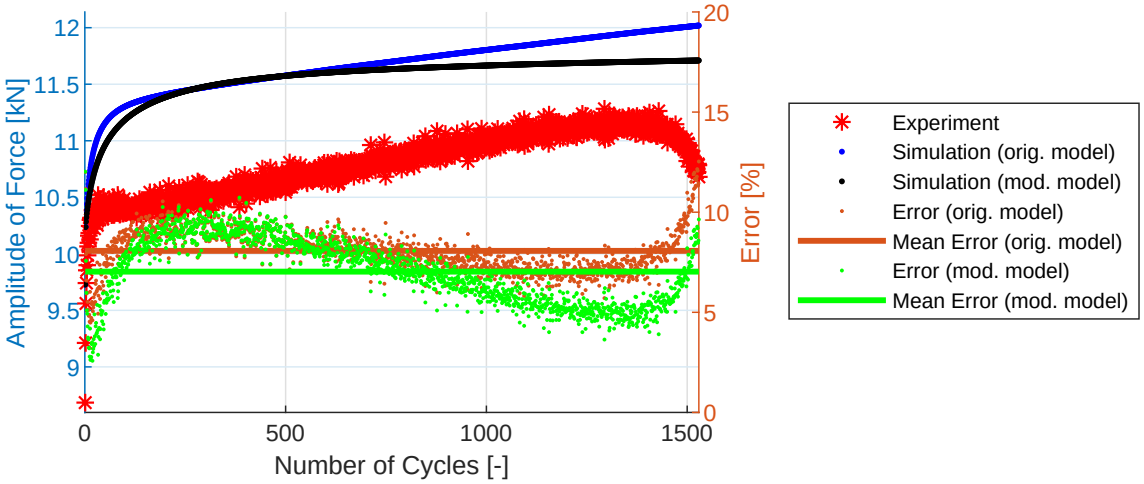

Figure B.4: Experiment vs. simulations, specimen E9-5. [A1]

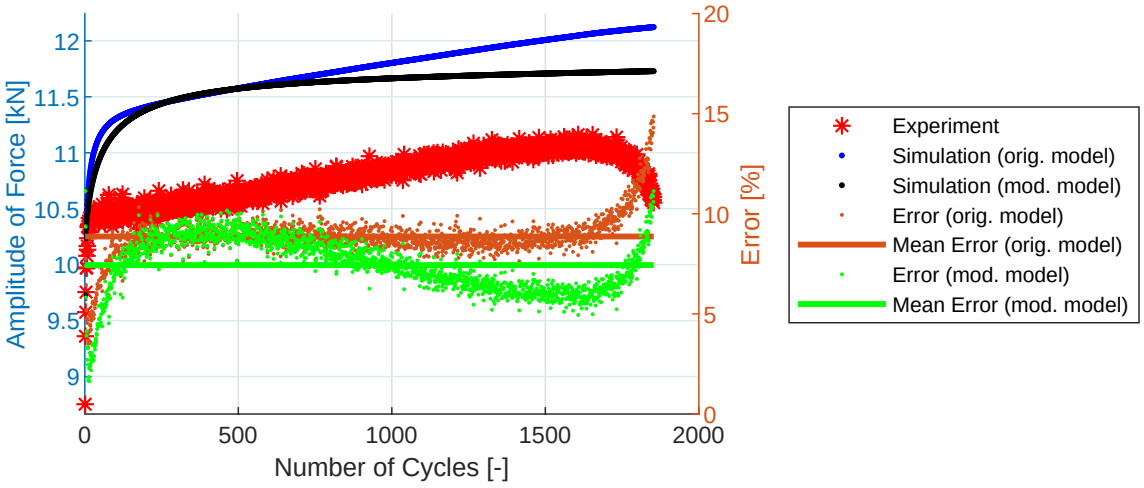

Figure B.5: Experiment vs. simulations, specimen E9-6. [A1]

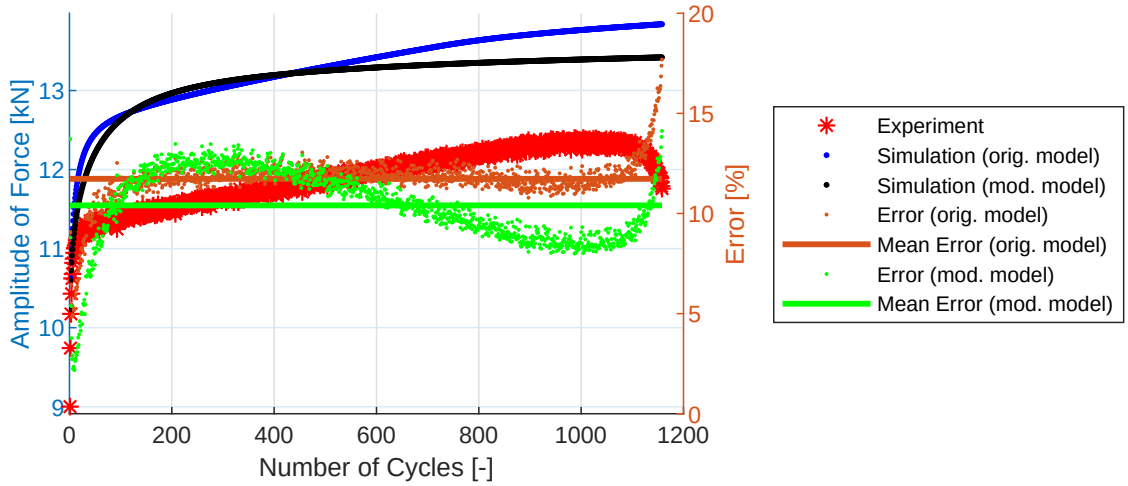

Figure B.6: Experiment vs. simulations, specimen E9-7. [A1]

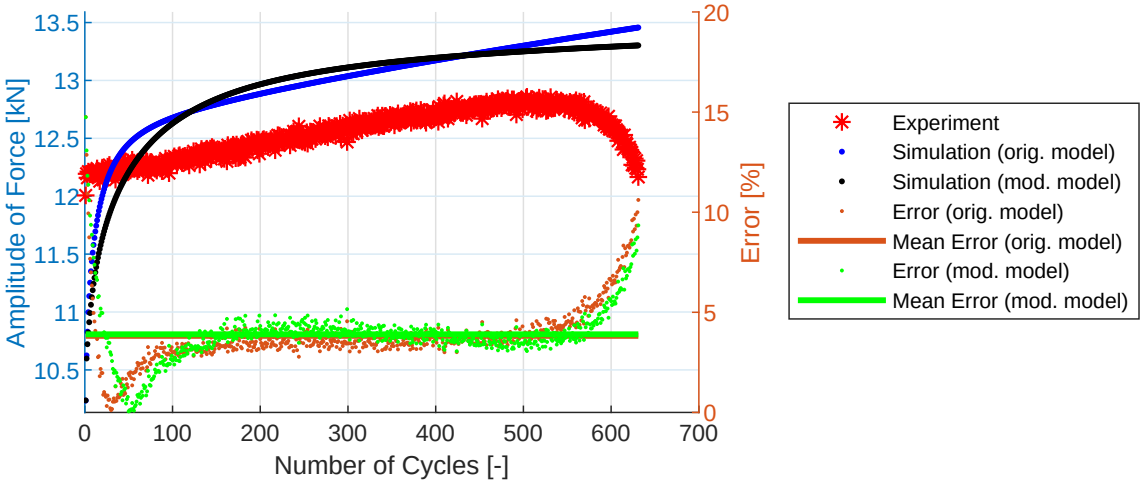

Figure B.7: Experiment vs. simulations, specimen E9-8. [A1]

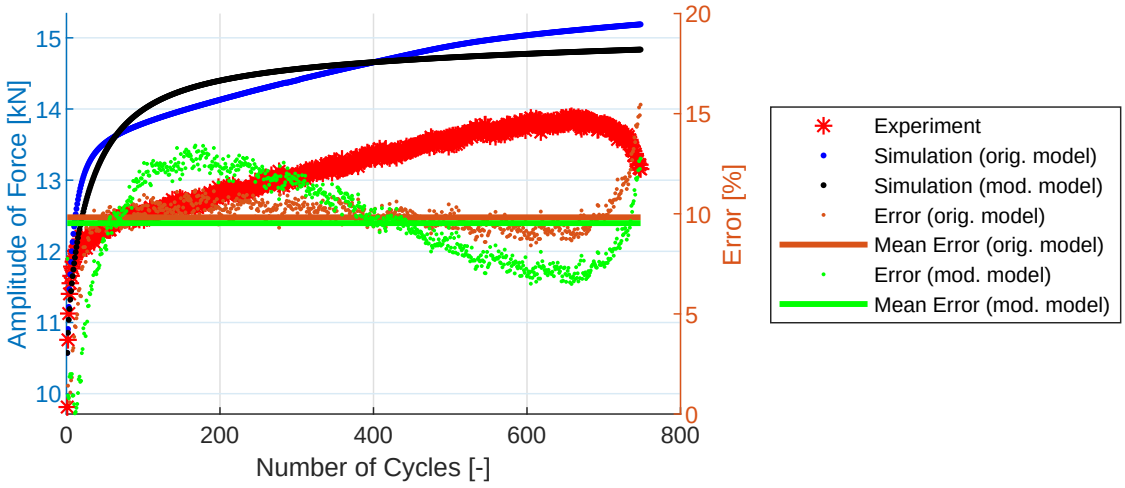

Figure B.8: Experiment vs. simulations, specimen E9-9. [A1]

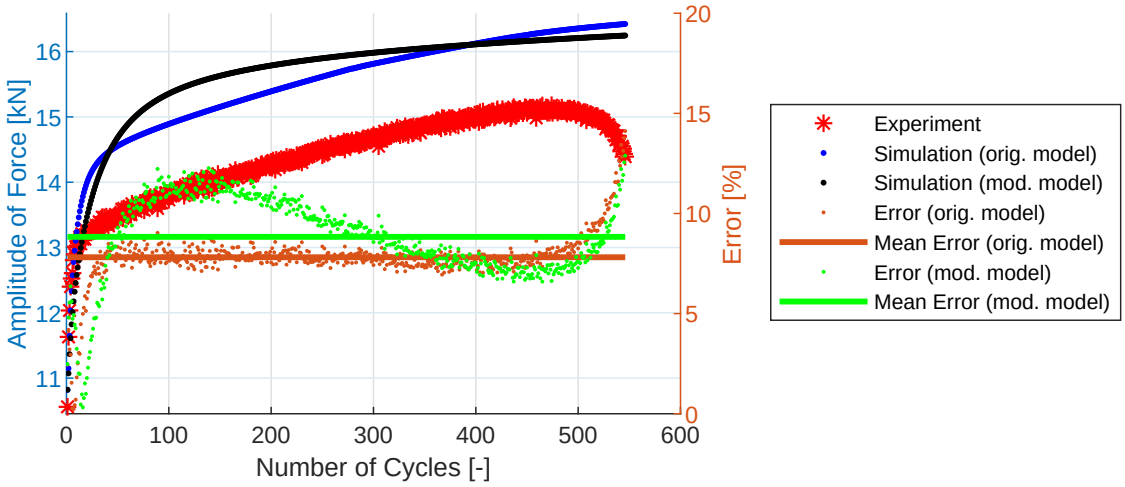

Figure B.9: Experiment vs. simulations, specimen E9-10. [A1]

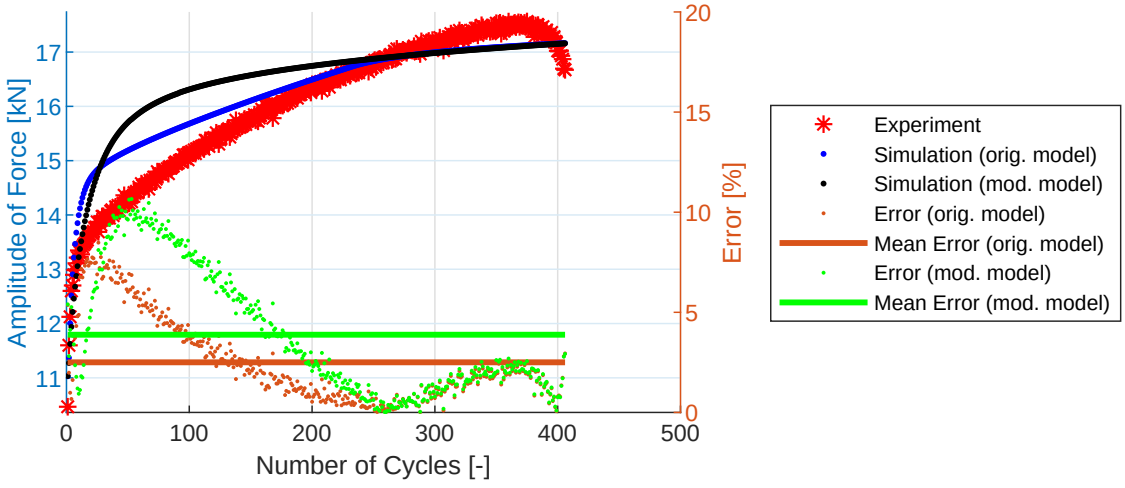

Figure B.10: Experiment vs. simulations, specimen E9-11. [A1]

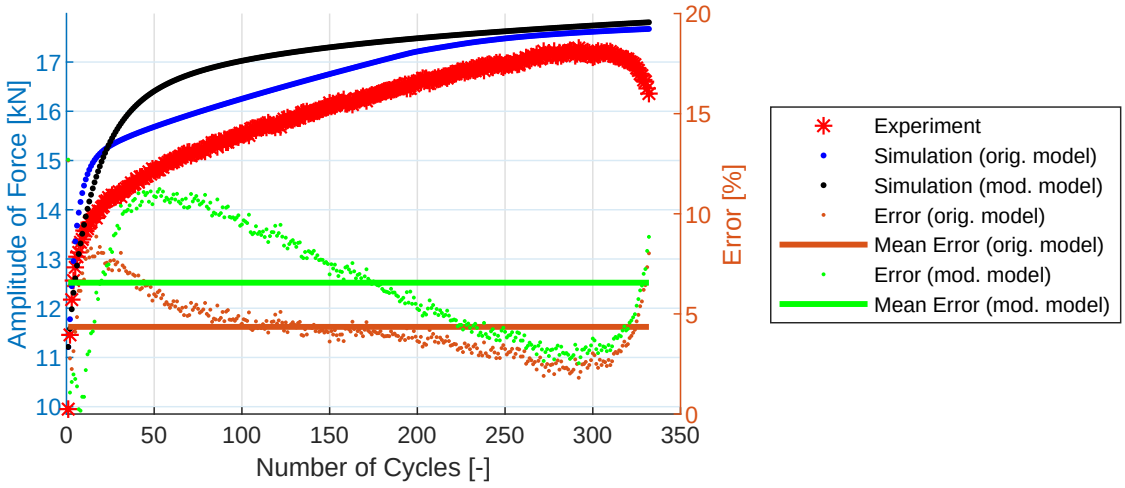

Figure B.11: Experiment vs. simulations, specimen E9-12. [A1]

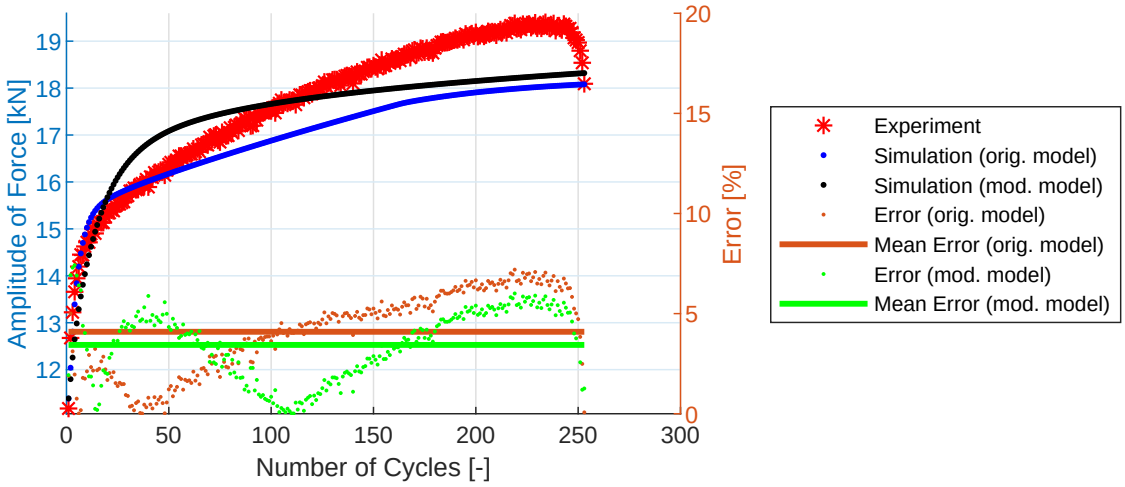

Figure B.12: Experiment vs. simulations, specimen E9-13. [A1]

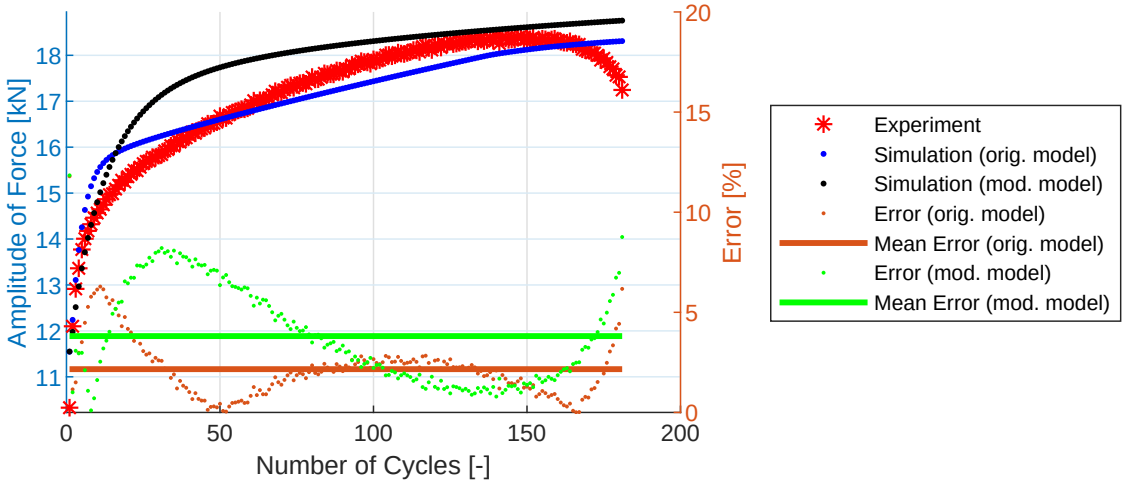

Figure B.13: Experiment vs. simulations, specimen E9-14. [A1]

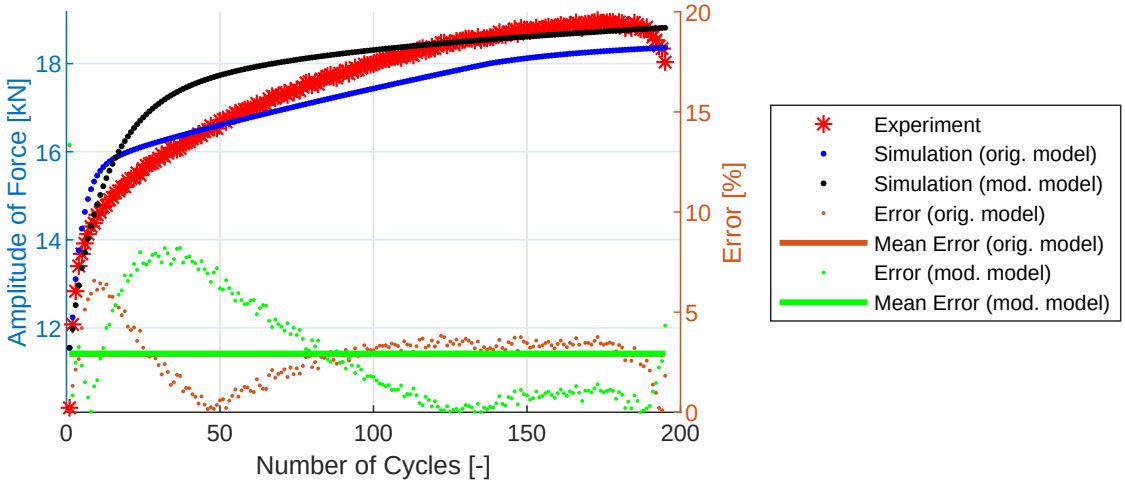

Figure B.14: Experiment vs. simulations, specimen E9-15. [A1]

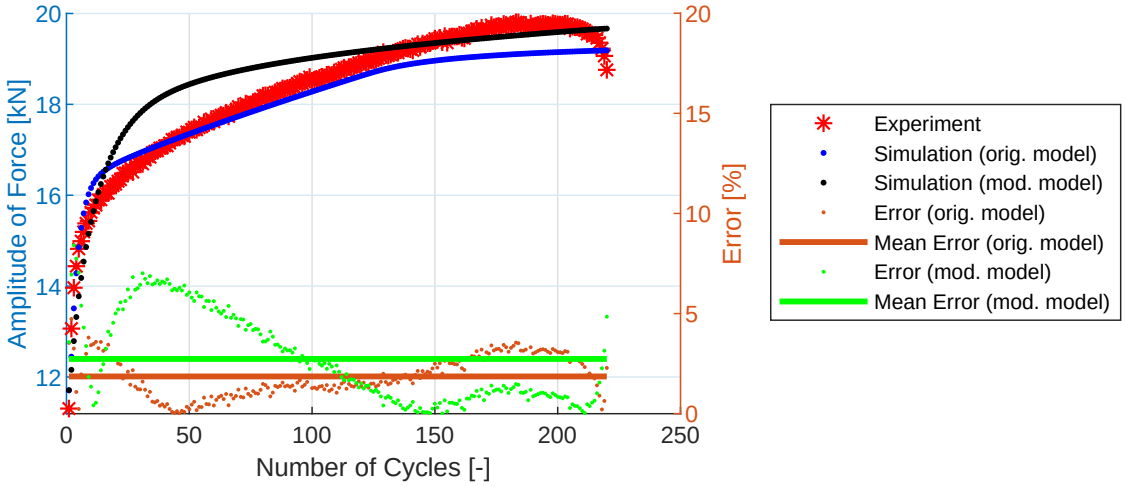

Figure B.15: Experiment vs. simulations, specimen E9-16. [A1]

B.2 NT Geometry

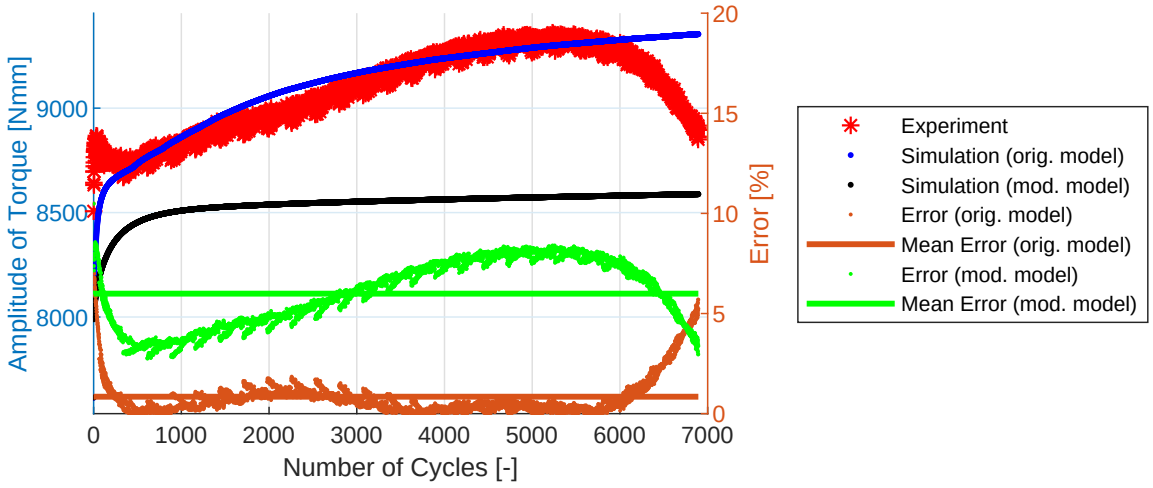

Figure B.16: Experiment vs. simulations, specimen NT-2.

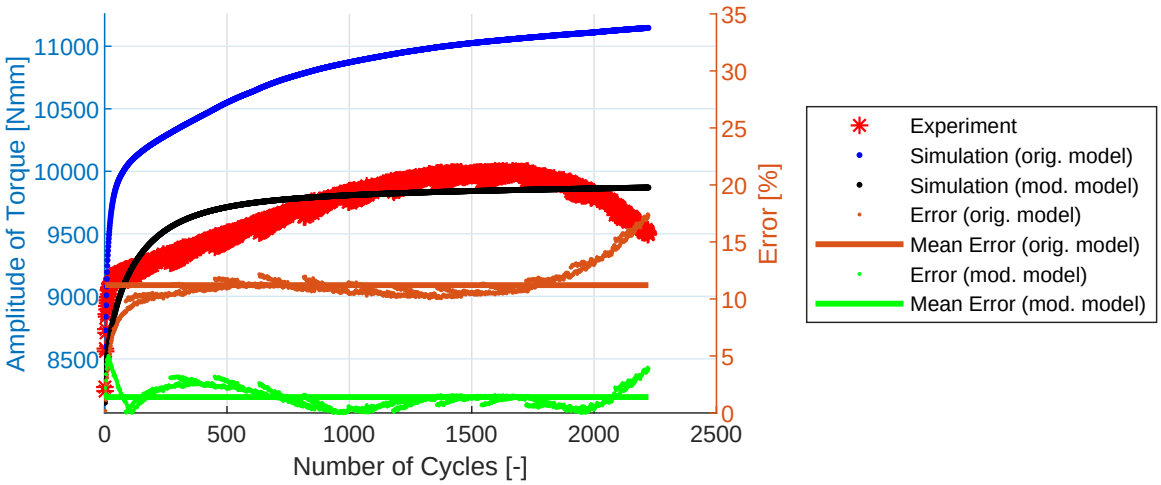

Figure B.17: Experiment vs. simulations, specimen NT-3.

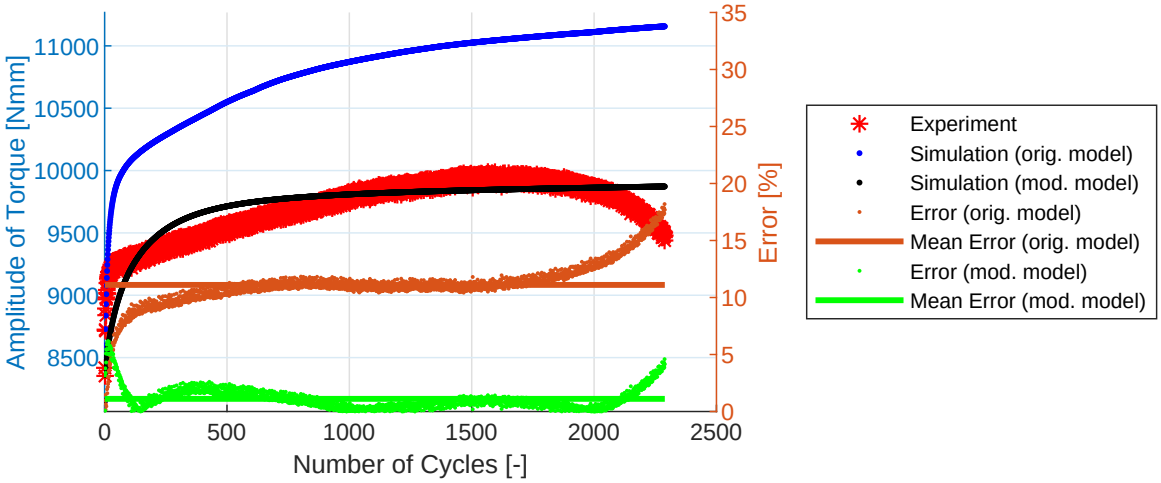

Figure B.18: Experiment vs. simulations, specimen NT-4.

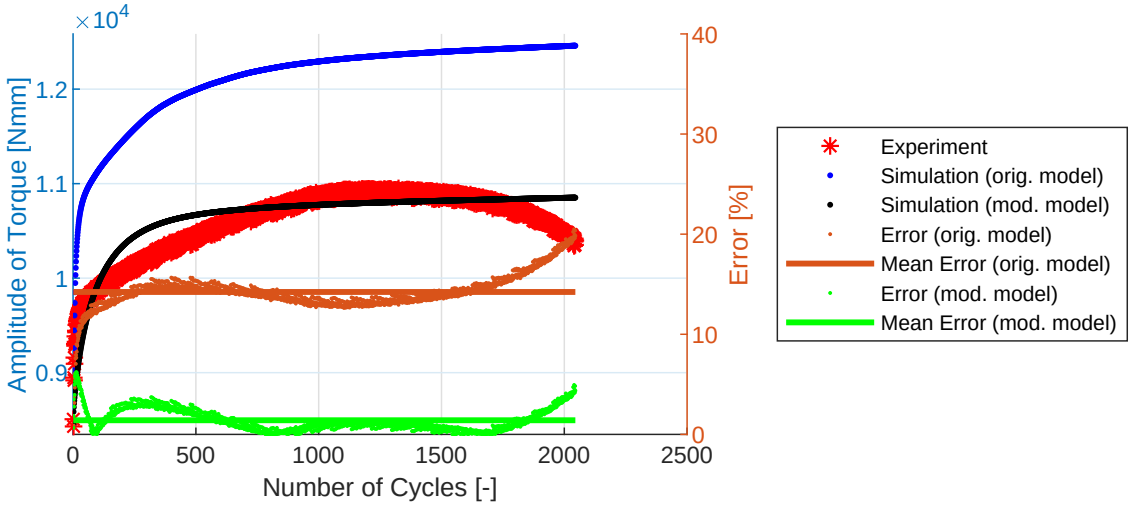

Figure B.19: Experiment vs. simulations, specimen NT-5.

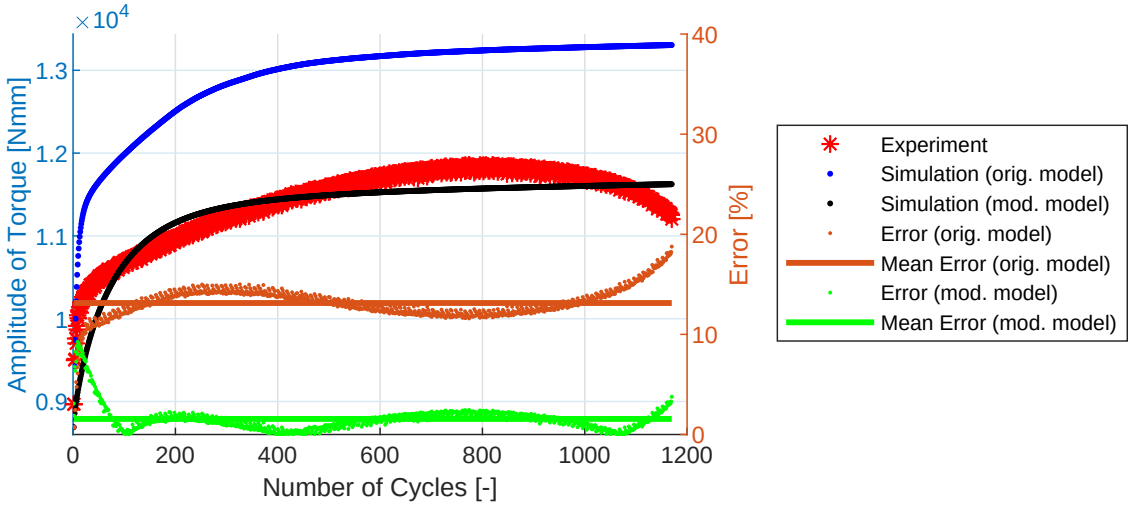

Figure B.20: Experiment vs. simulations, specimen NT-7.

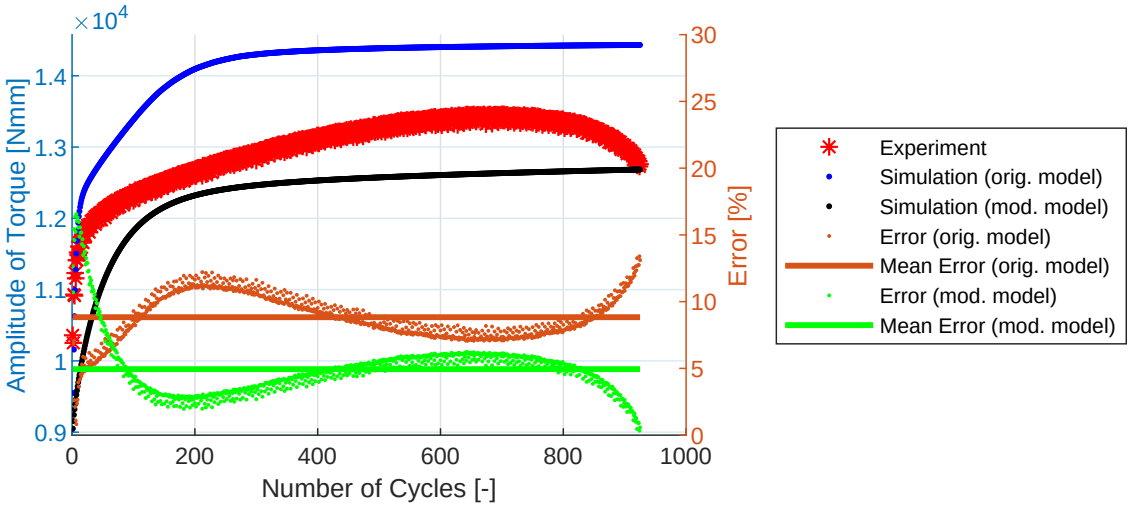

Figure B.21: Experiment vs. simulations, specimen NT-8.

B.3 R1.2 Geometry

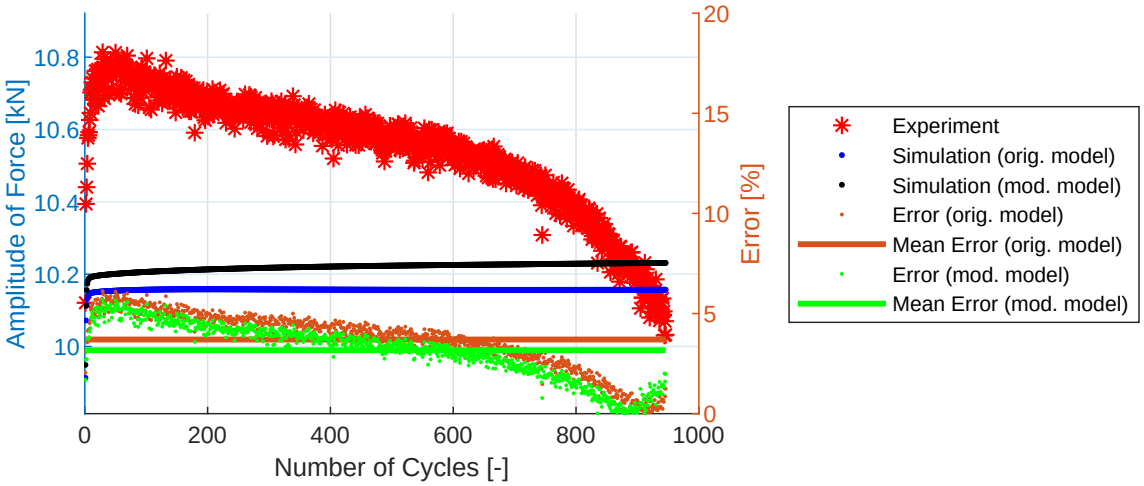

Figure B.22: Experiment vs. simulations, specimen R1.2-2.

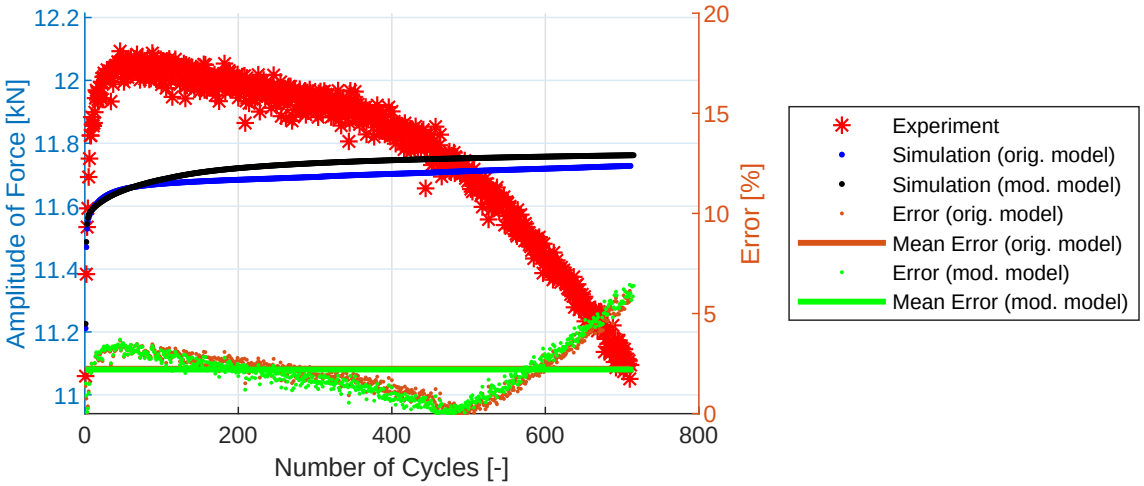

Figure B.23: Experiment vs. simulations, specimen R1.2-3.

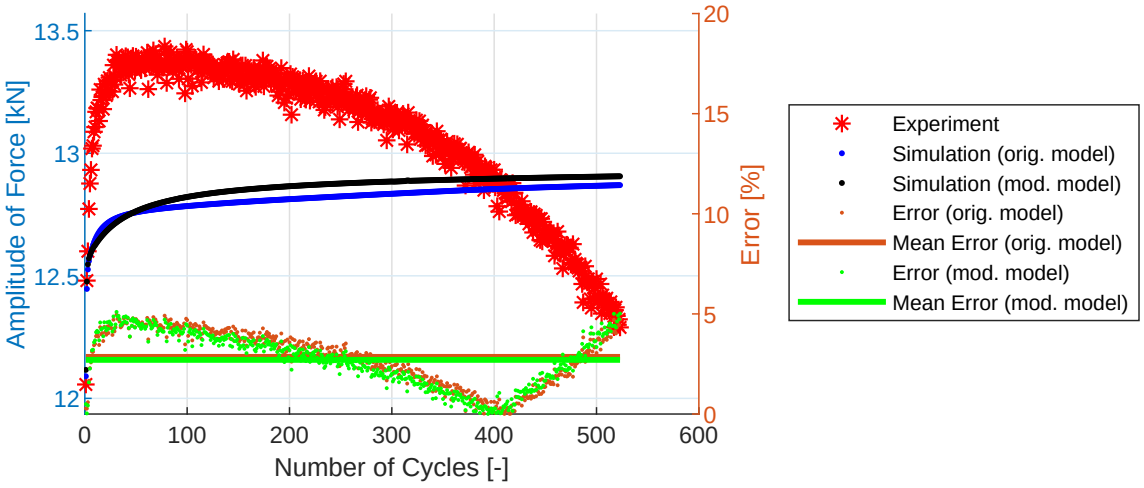

Figure B.24: Experiment vs. simulations, specimen R1.2-4.

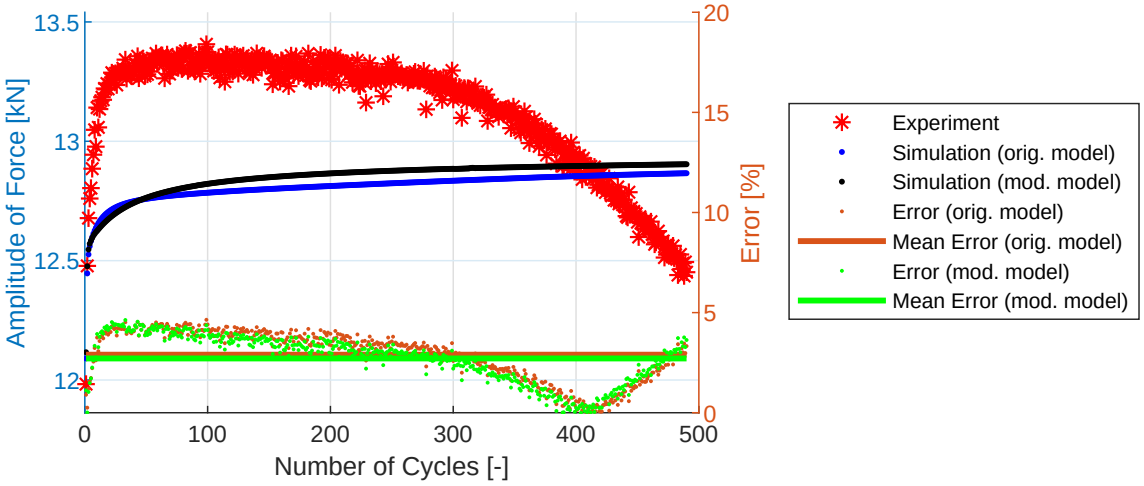

Figure B.25: Experiment vs. simulations, specimen R1.2-5.

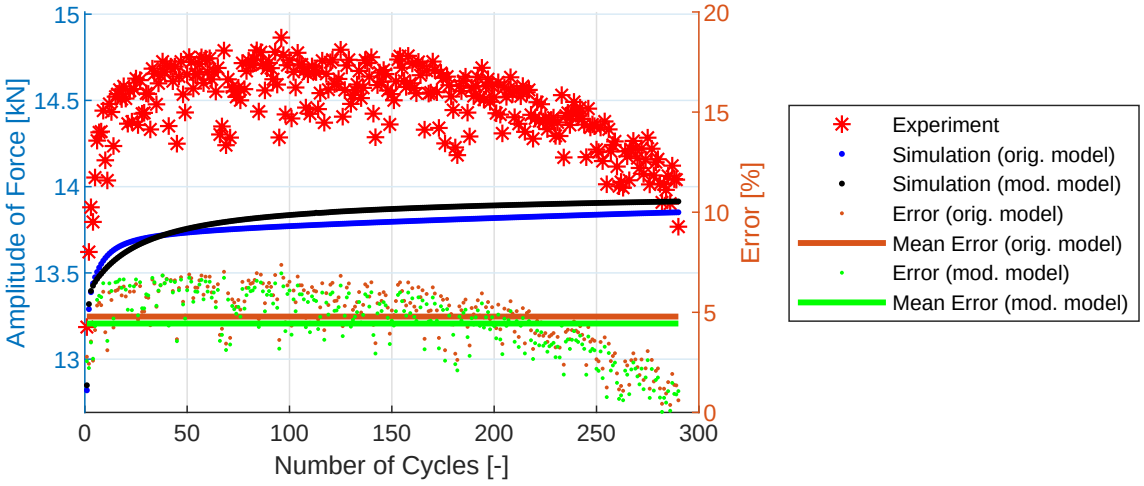

Figure B.26: Experiment vs. simulations, specimen R1.2-6.

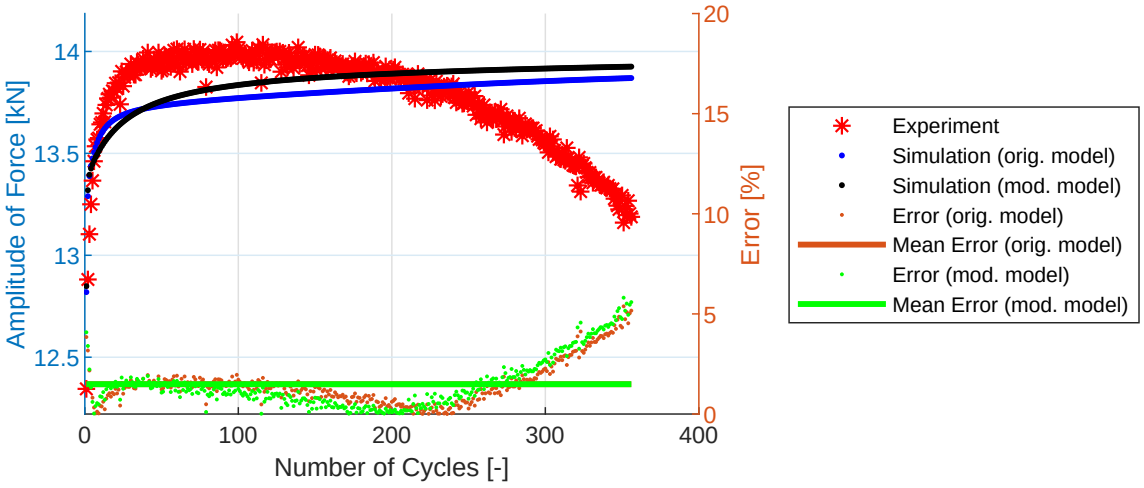

Figure B.27: Experiment vs. simulations, specimen R1.2-7.

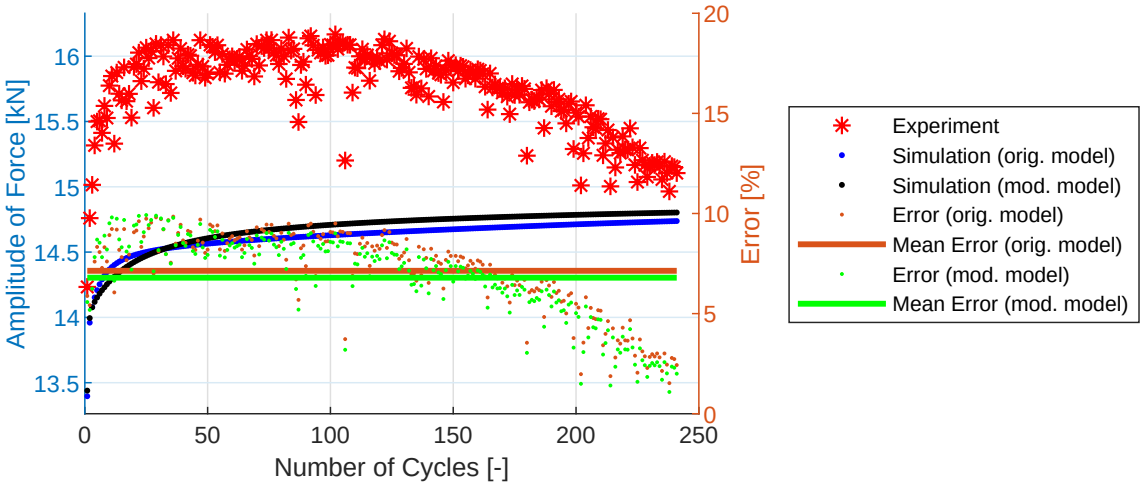

Figure B.28: Experiment vs. simulations, specimen R1.2-8.

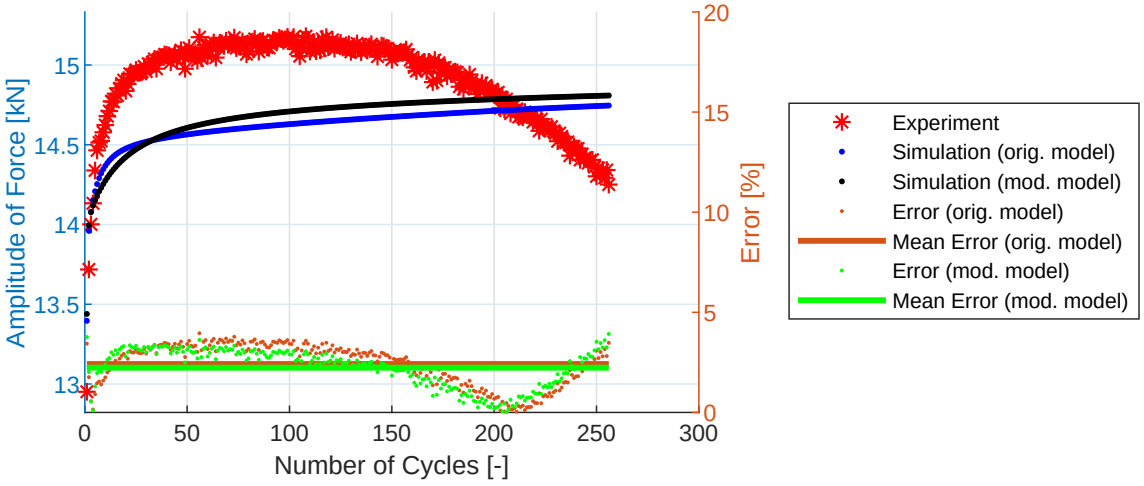

Figure B.29: Experiment vs. simulations, specimen R1.2-9.

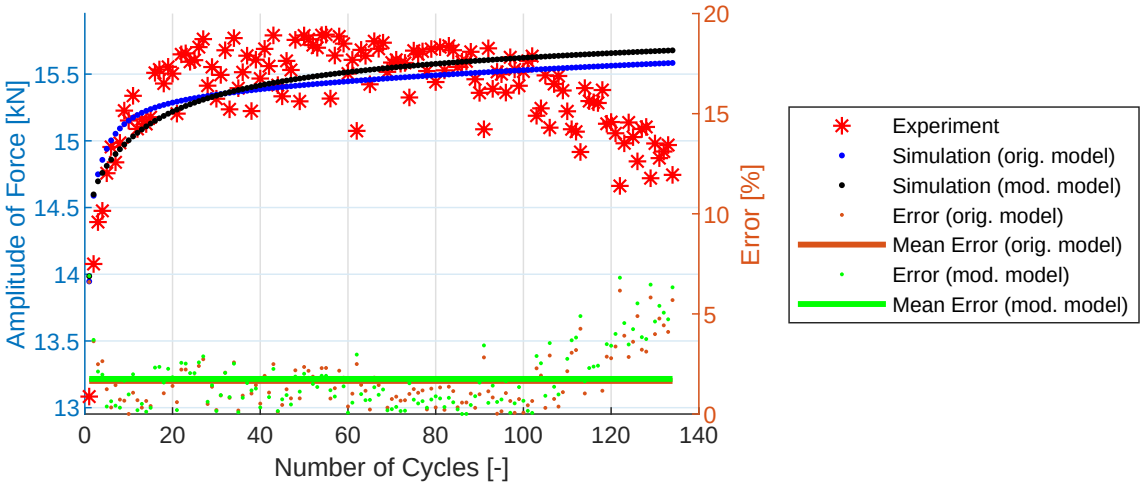

Figure B.30: Experiment vs. simulations, specimen R1.2-10.

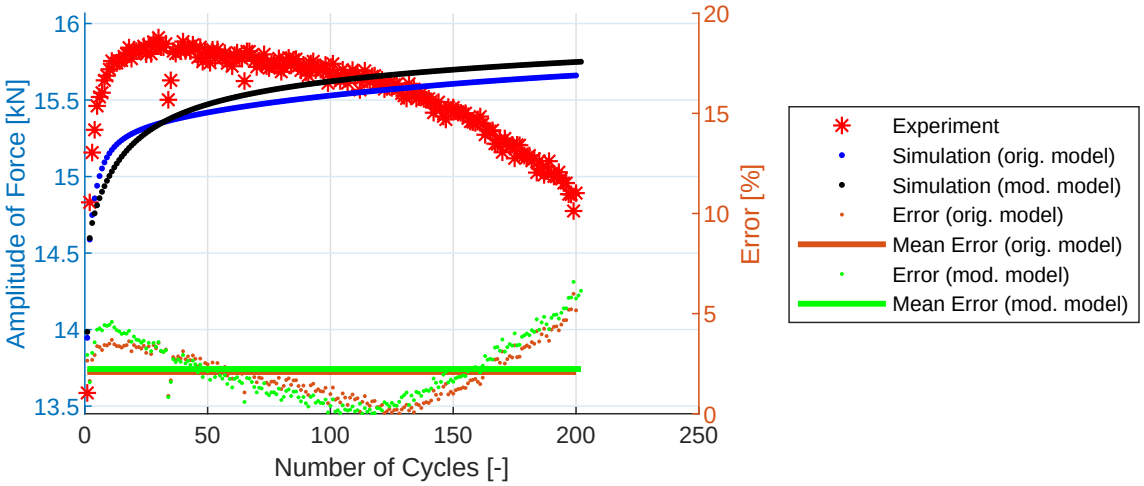

Figure B.31: Experiment vs. simulations, specimen R1.2-11.

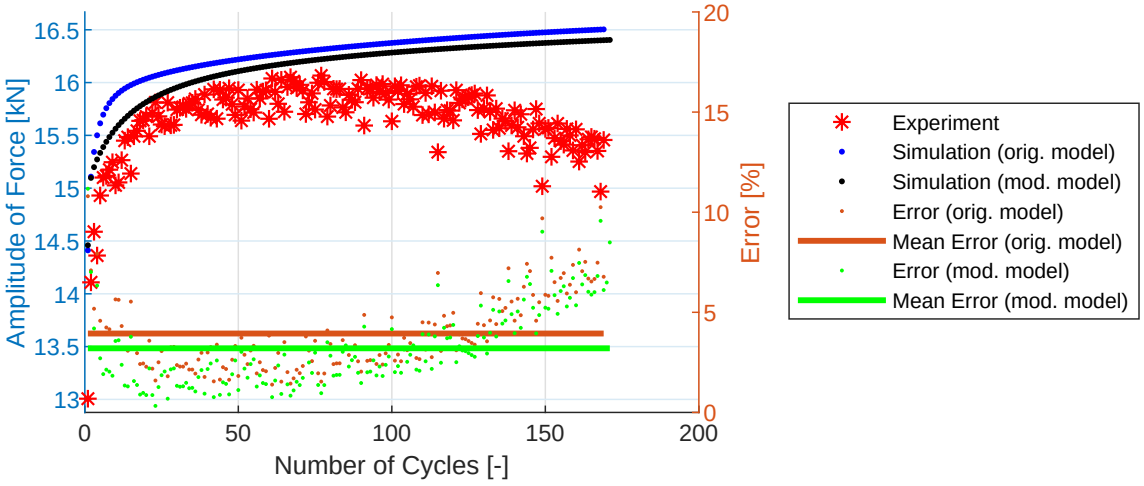

Figure B.32: Experiment vs. simulations, specimen R1.2-12.

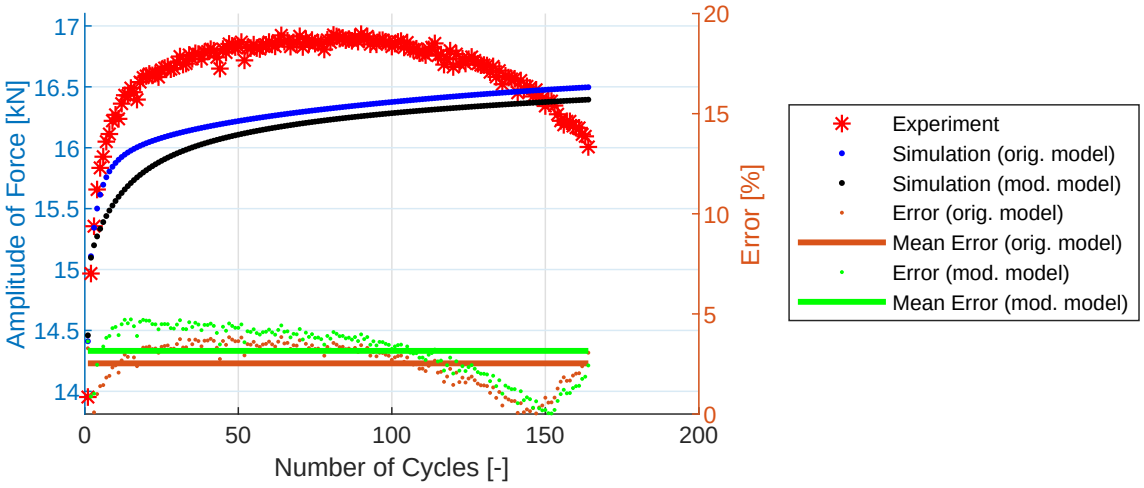

Figure B.33: Experiment vs. simulations, specimen R1.2-13.

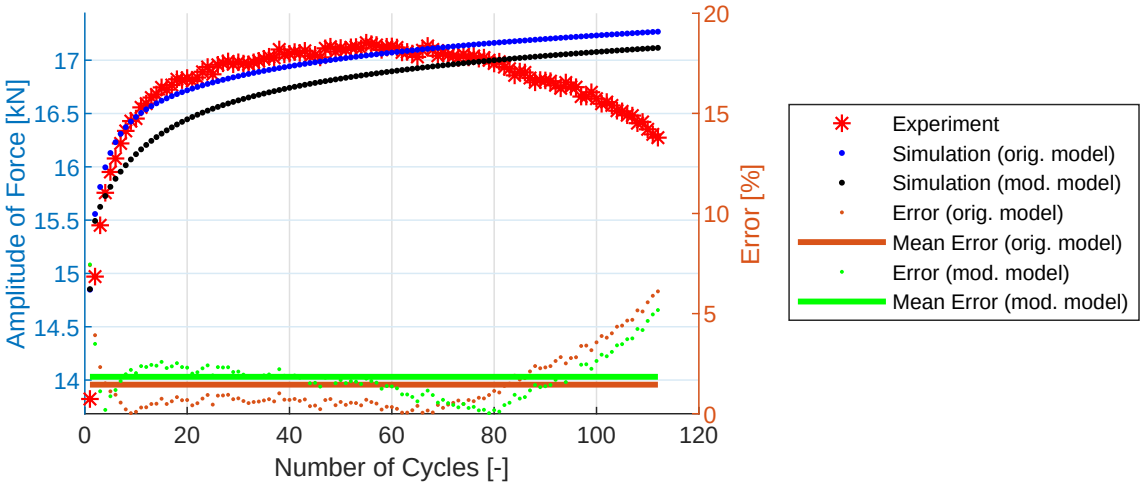

Figure B.34: Experiment vs. simulations, specimen R1.2-14.

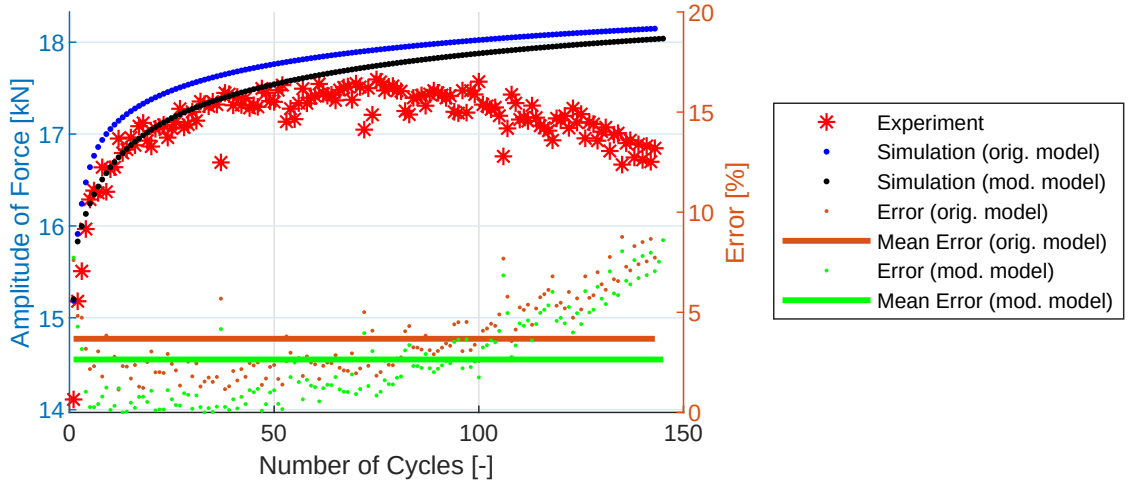

Figure B.35: Experiment vs. simulations, specimen R1.2-15.

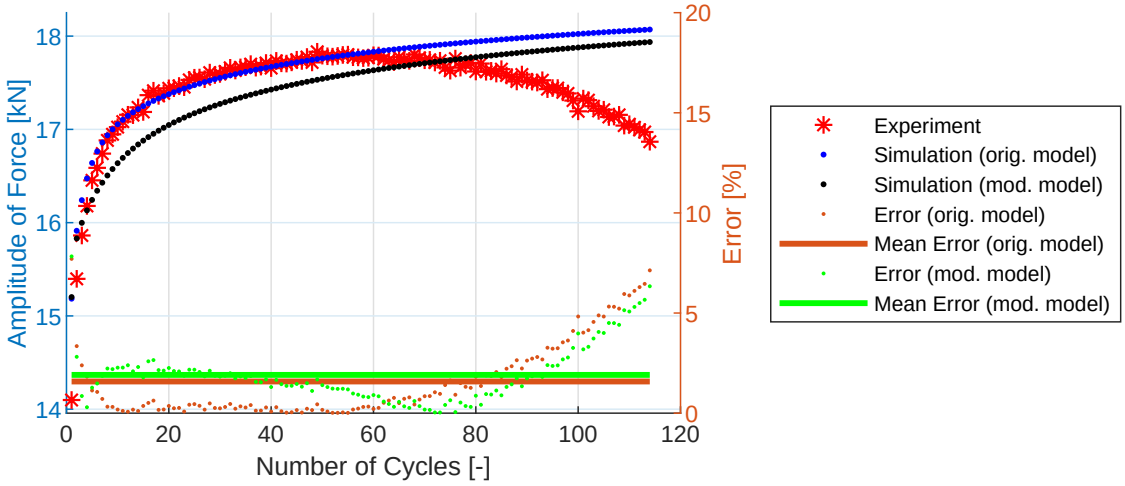

Figure B.36: Experiment vs. simulations, specimen R1.2-16.

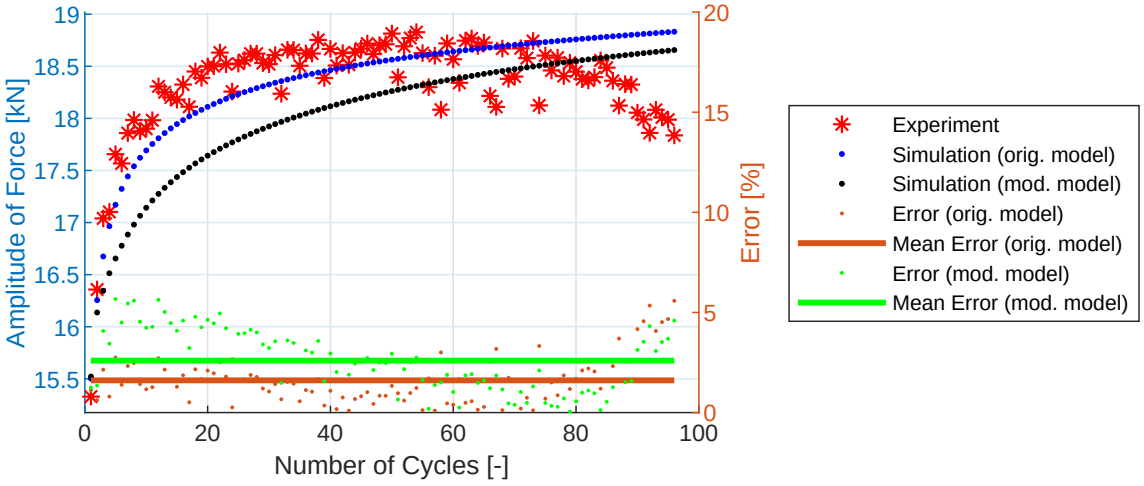

Figure B.37: Experiment vs. simulations, specimen R1.2-17.

B.4 R2.5 Geometry

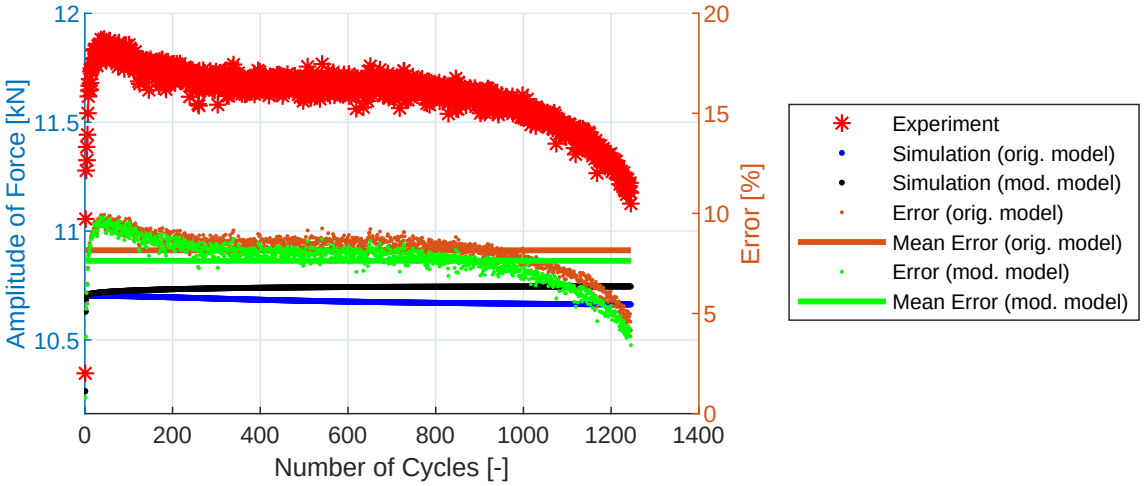

Figure B.38: Experiment vs. simulations, specimen R2.5-2.

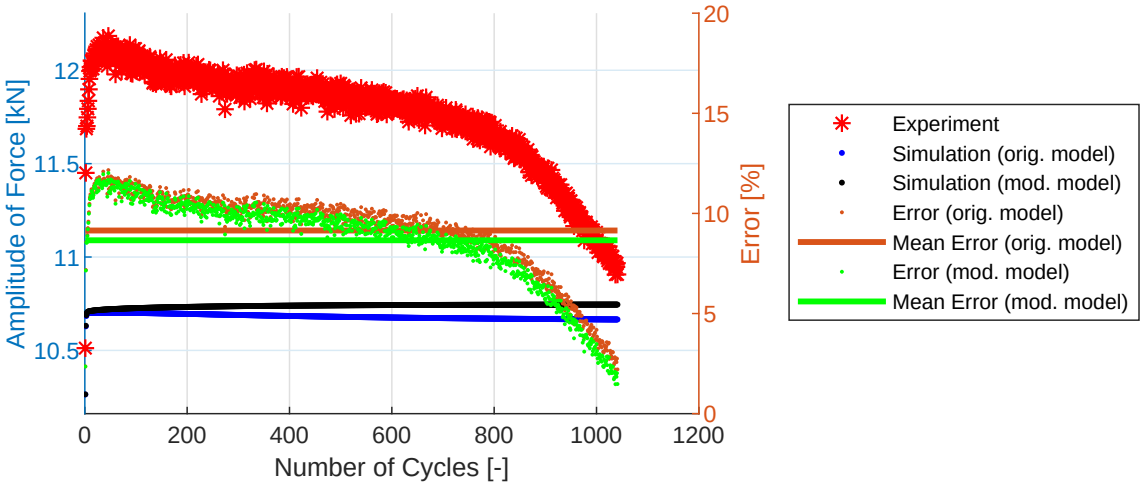

Figure B.39: Experiment vs. simulations, specimen R2.5-3.

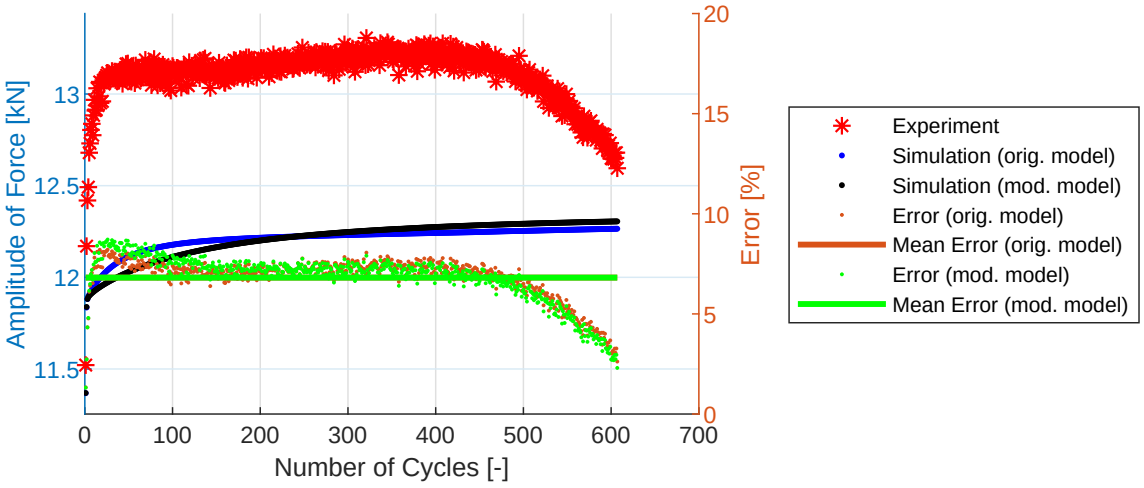

Figure B.40: Experiment vs. simulations, specimen R2.5-4.

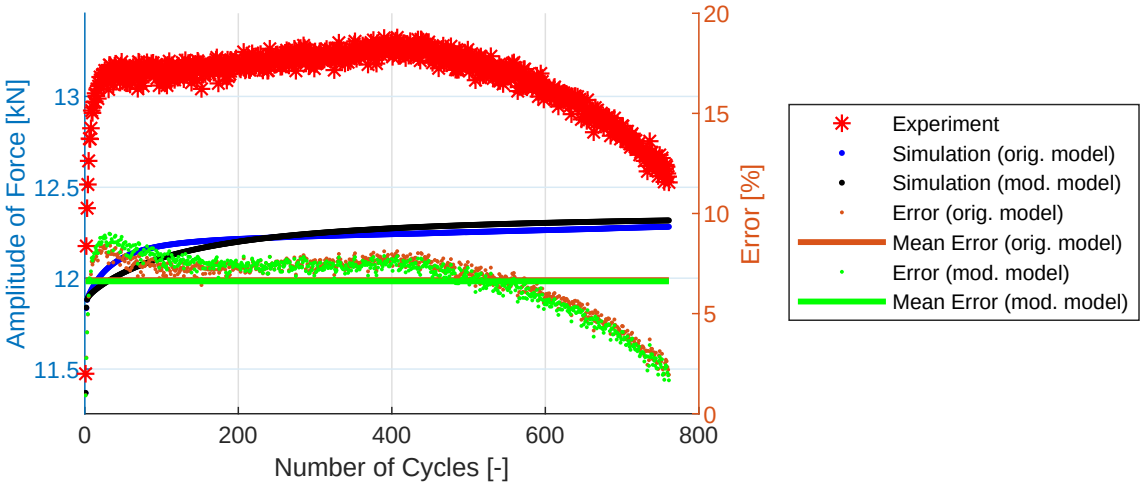

Figure B.41: Experiment vs. simulations, specimen R2.5-5.

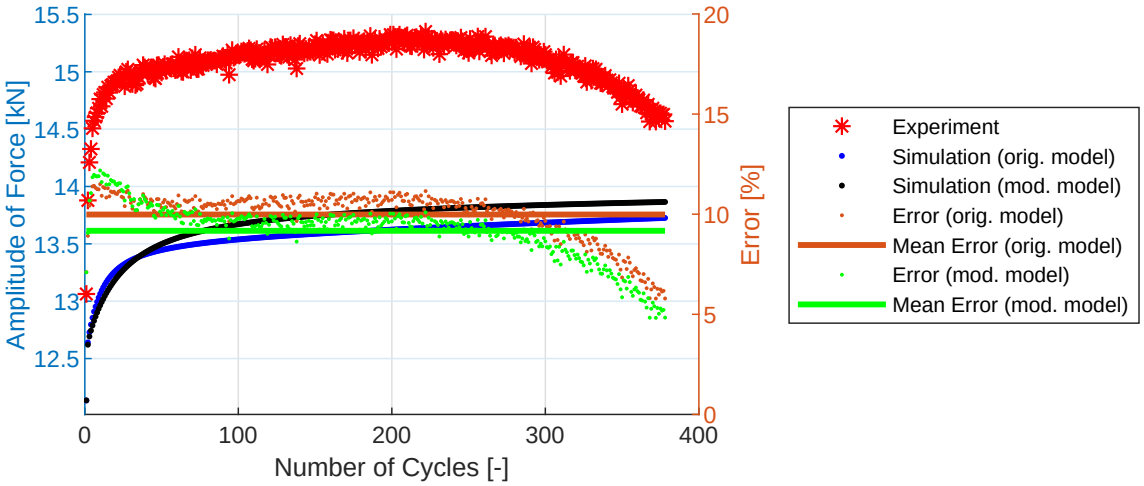

Figure B.42: Experiment vs. simulations, specimen R2.5-6.

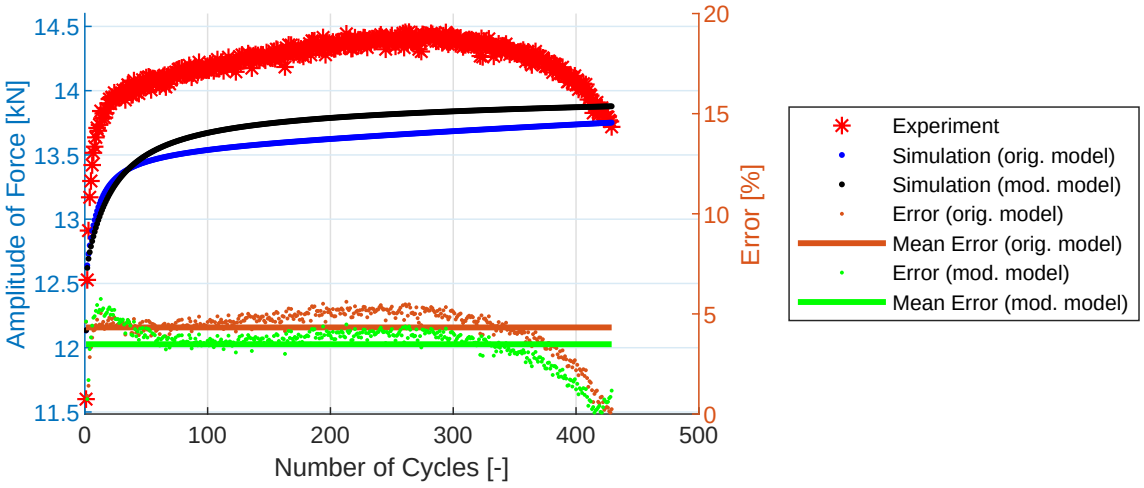

Figure B.43: Experiment vs. simulations, specimen R2.5-7.

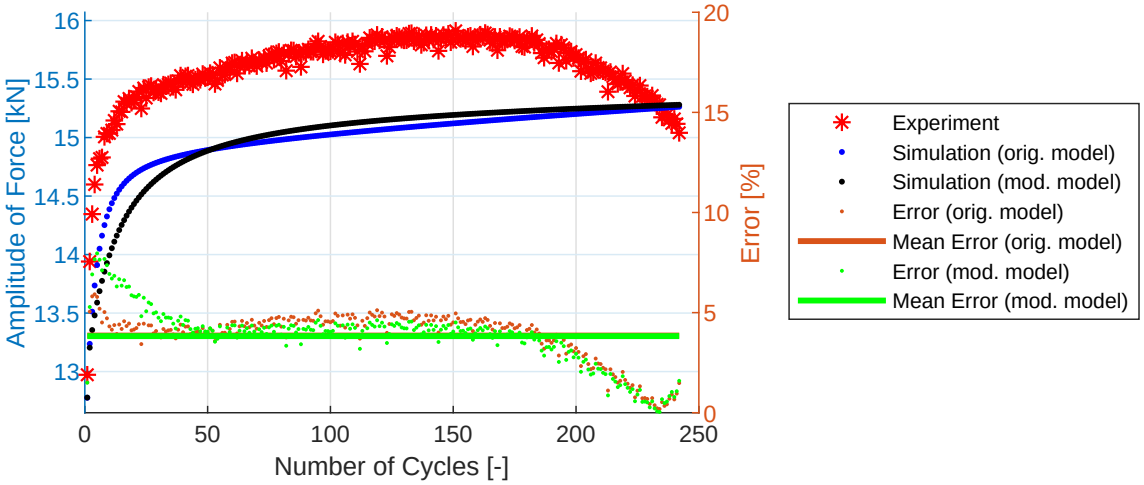

Figure B.44: Experiment vs. simulations, specimen R2.5-8.

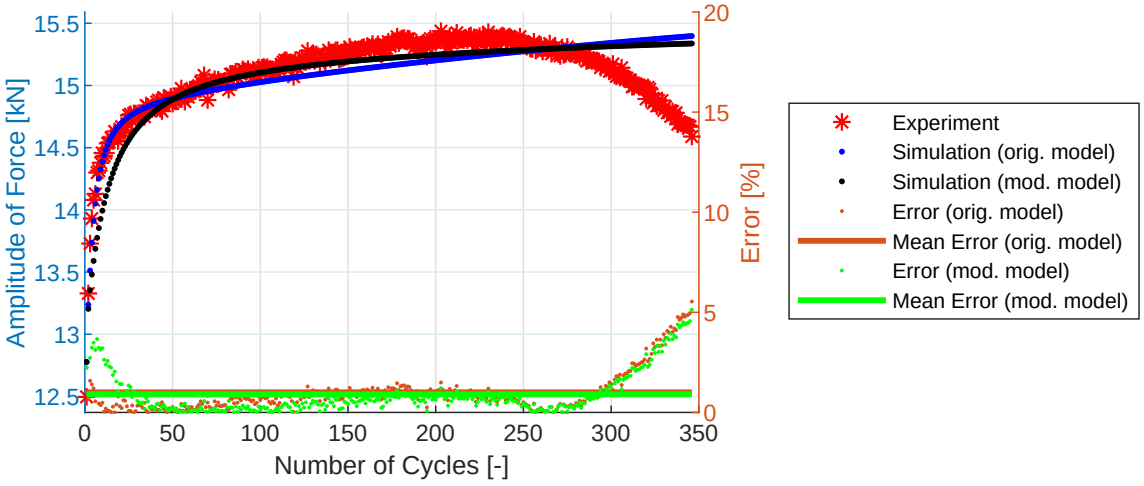

Figure B.45: Experiment vs. simulations, specimen R2.5-9.

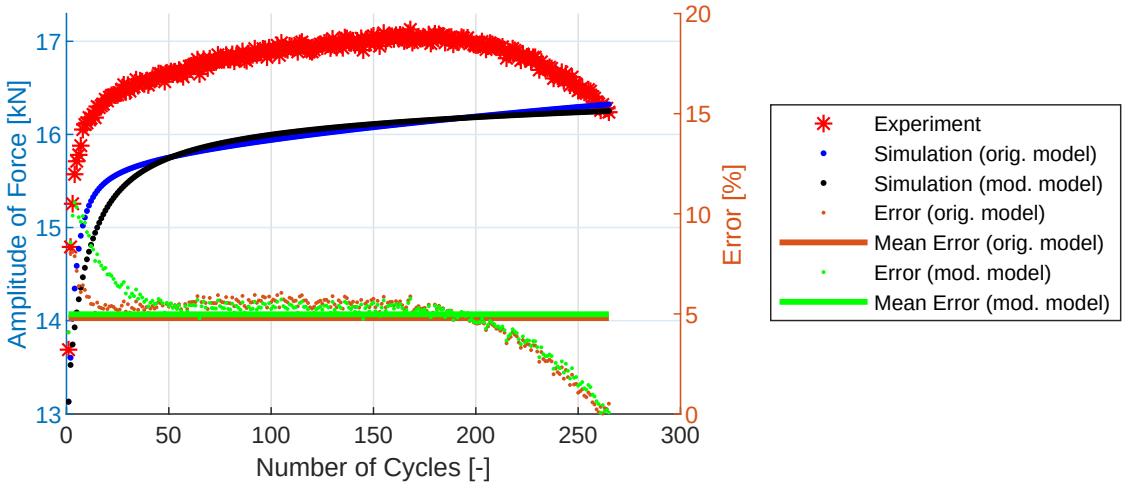

Figure B.46: Experiment vs. simulations, specimen R2.5-10.

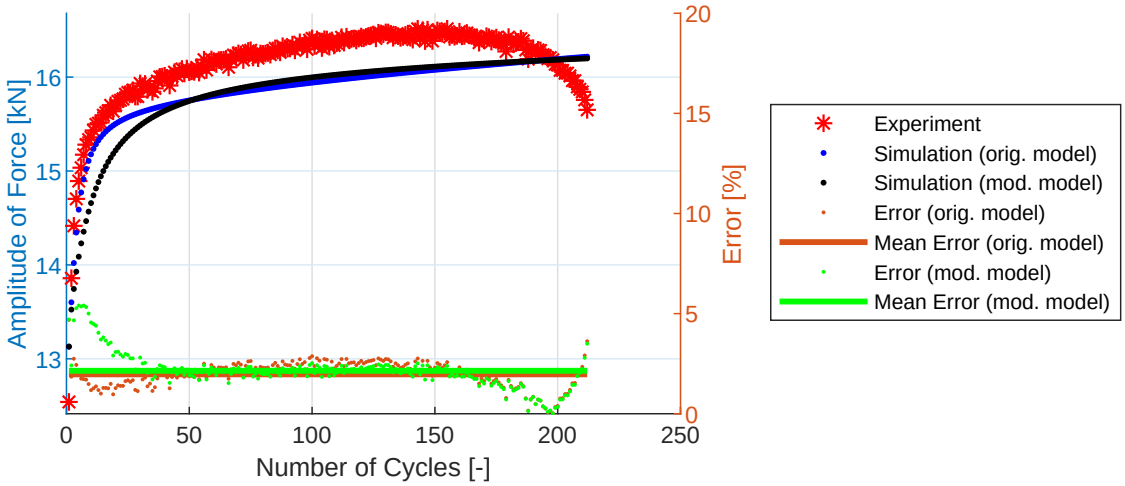

Figure B.47: Experiment vs. simulations, specimen R2.5-11.

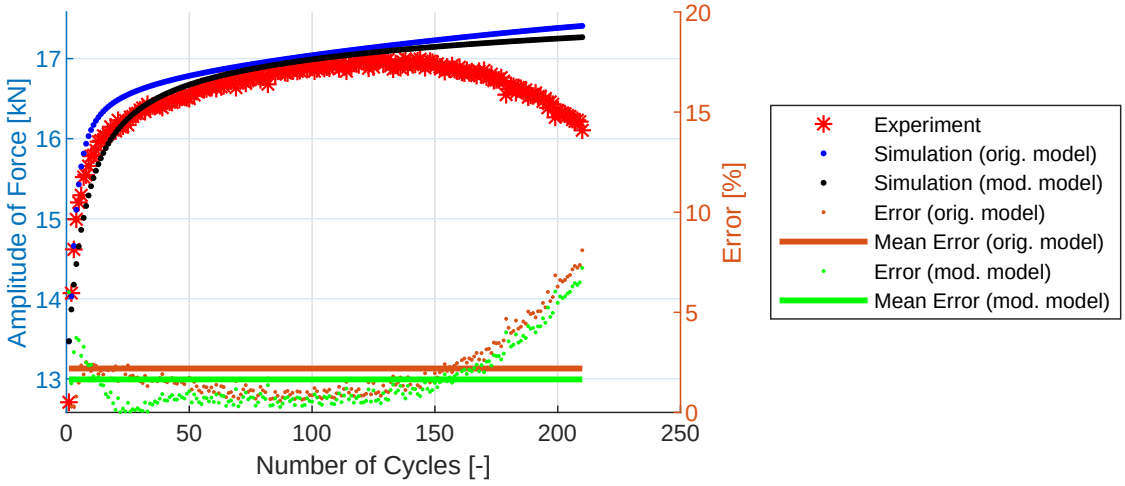

Figure B.48: Experiment vs. simulations, specimen R2.5-12.

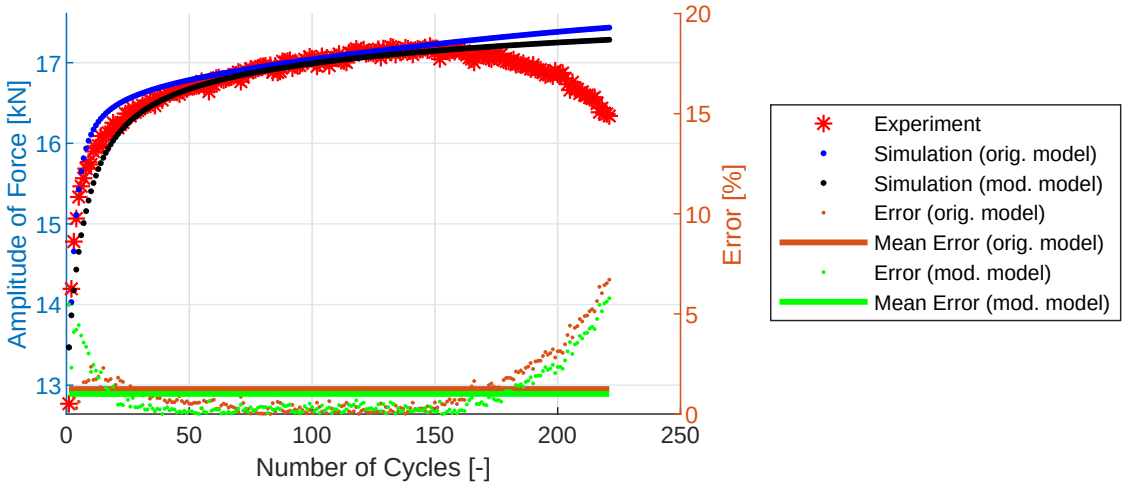

Figure B.49: Experiment vs. simulations, specimen R2.5-13.

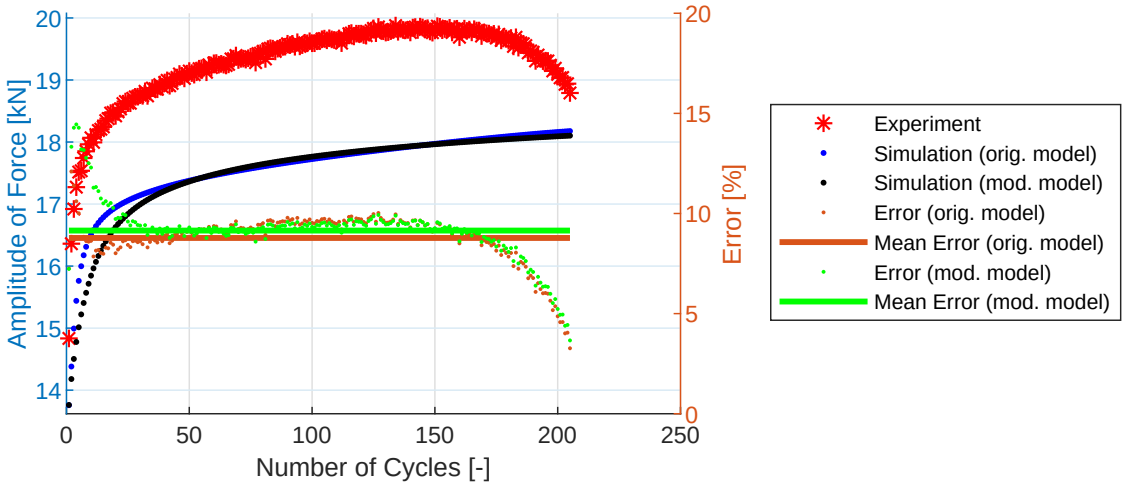

Figure B.50: Experiment vs. simulations, specimen R2.5-14.

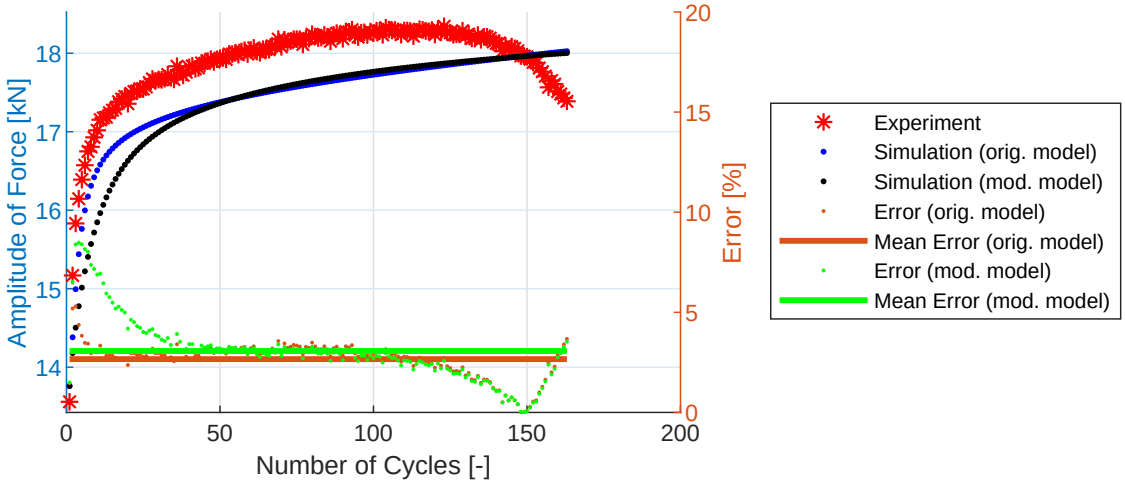

Figure B.51: Experiment vs. simulations, specimen R2.5-15.

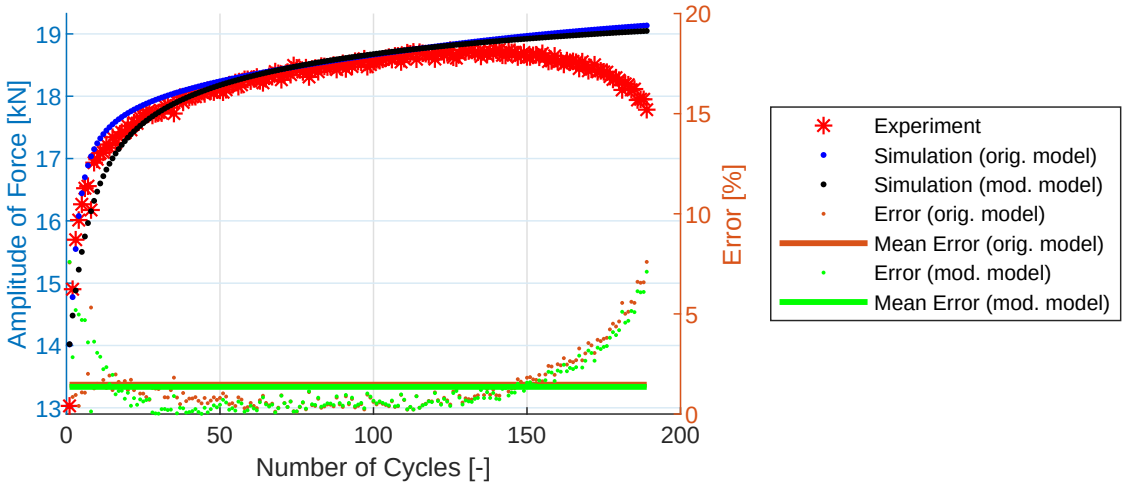

Figure B.52: Experiment vs. simulations, specimen R2.5-16.

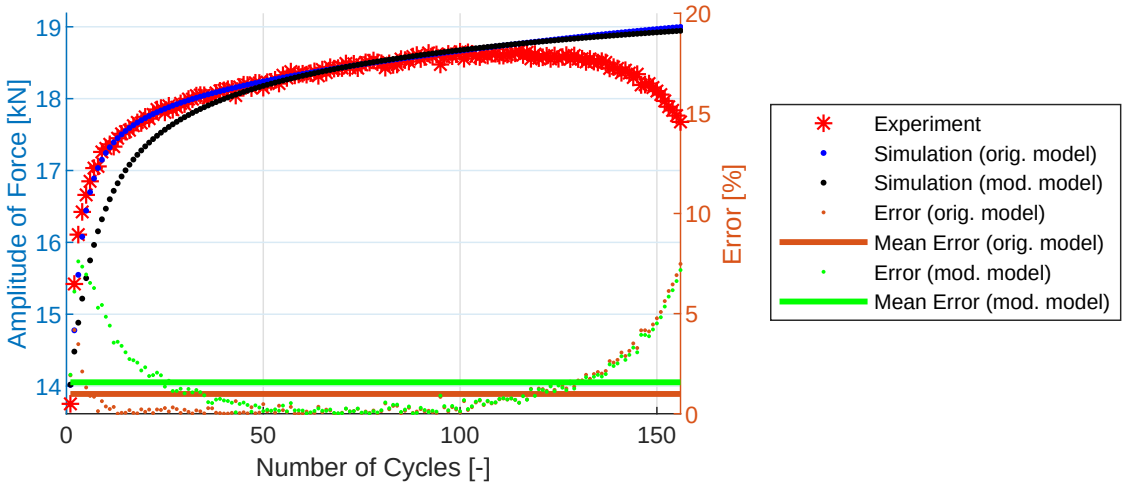

Figure B.53: Experiment vs. simulations, specimen R2.5-17.

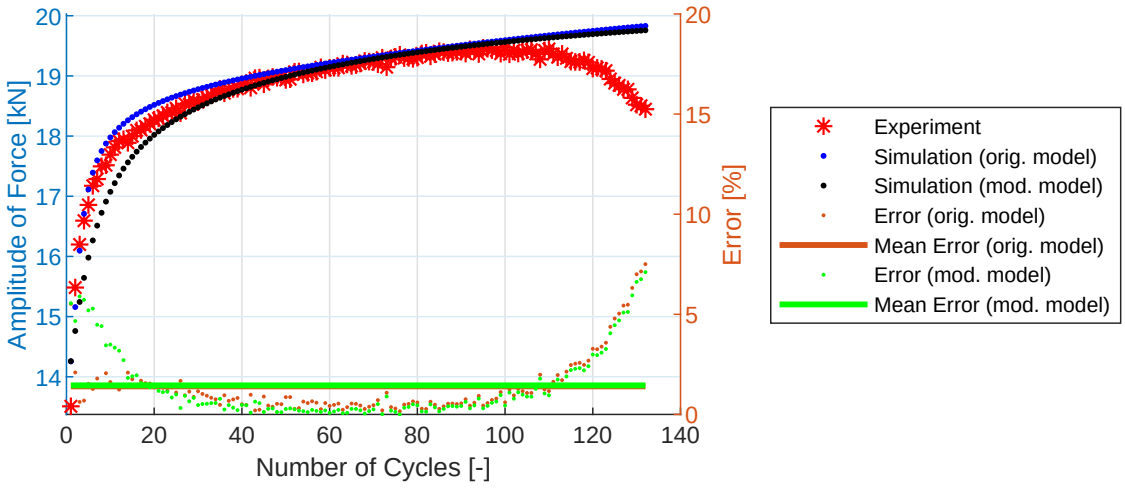

Figure B.54: Experiment vs. simulations, specimen R2.5-18.

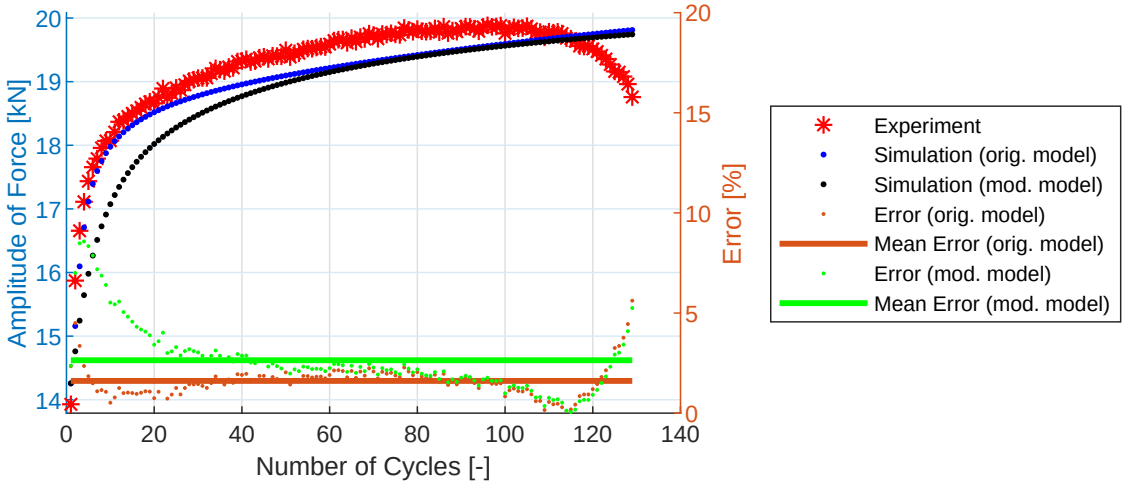

Figure B.55: Experiment vs. simulations, specimen R2.5-19.

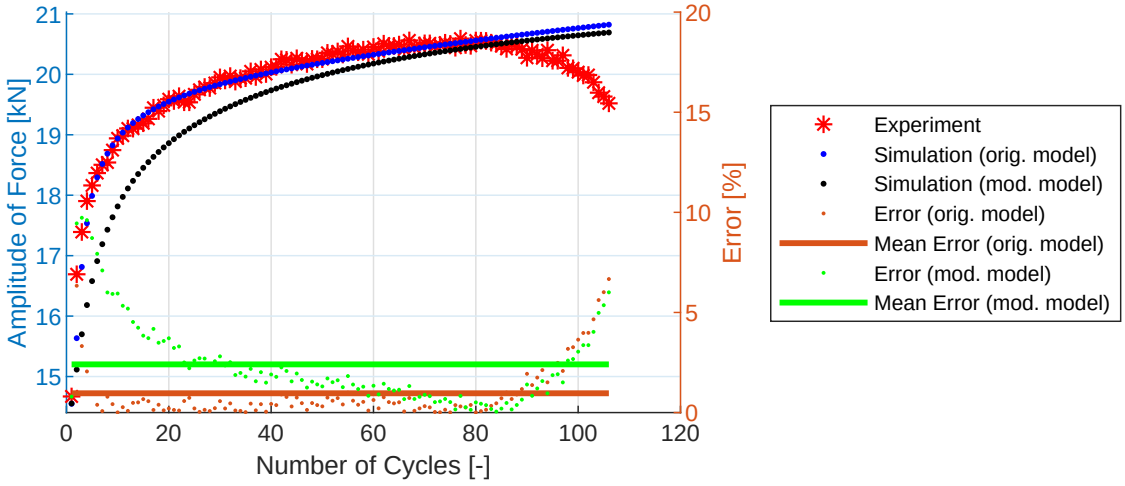

Figure B.56: Experiment vs. simulations, specimen R2.5-20.

B.5 R5 Geometry

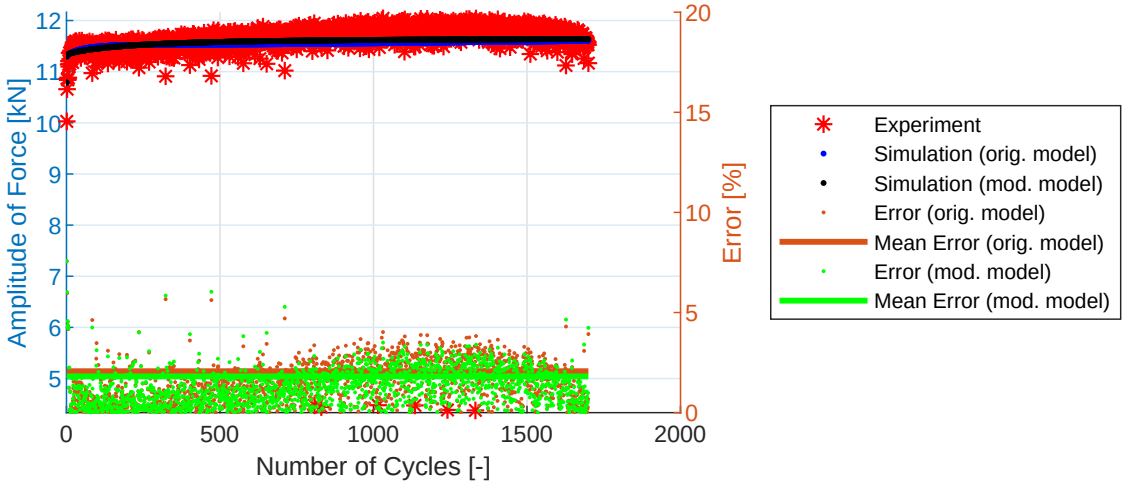

Figure B.57: Experiment vs. simulations, specimen R5-2.

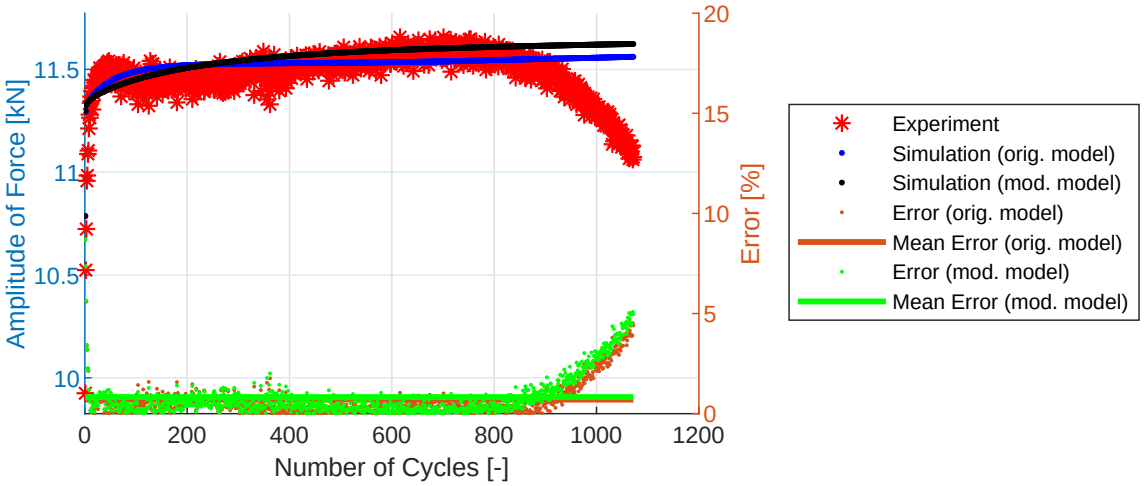

Figure B.58: Experiment vs. simulations, specimen R5-3.

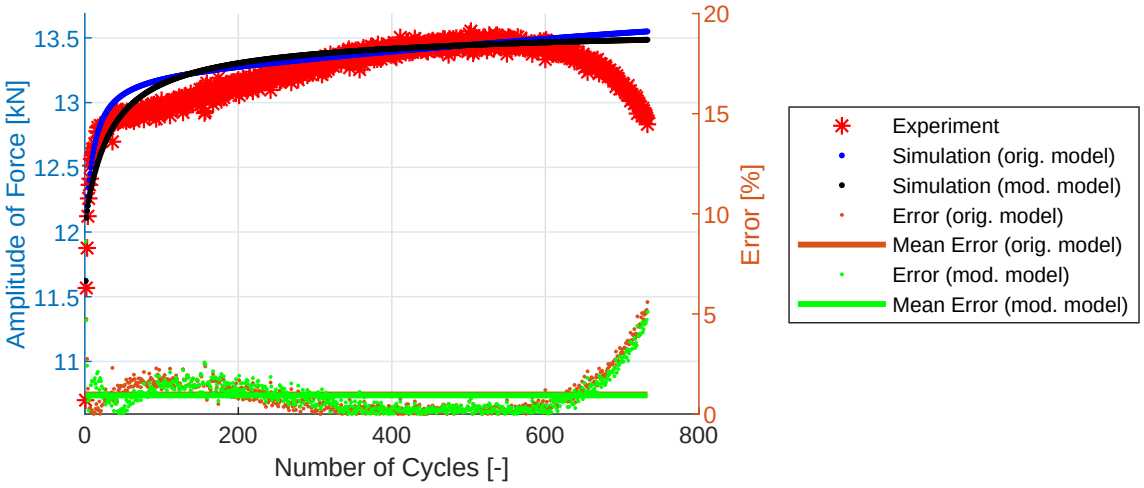

Figure B.59: Experiment vs. simulations, specimen R5-4.

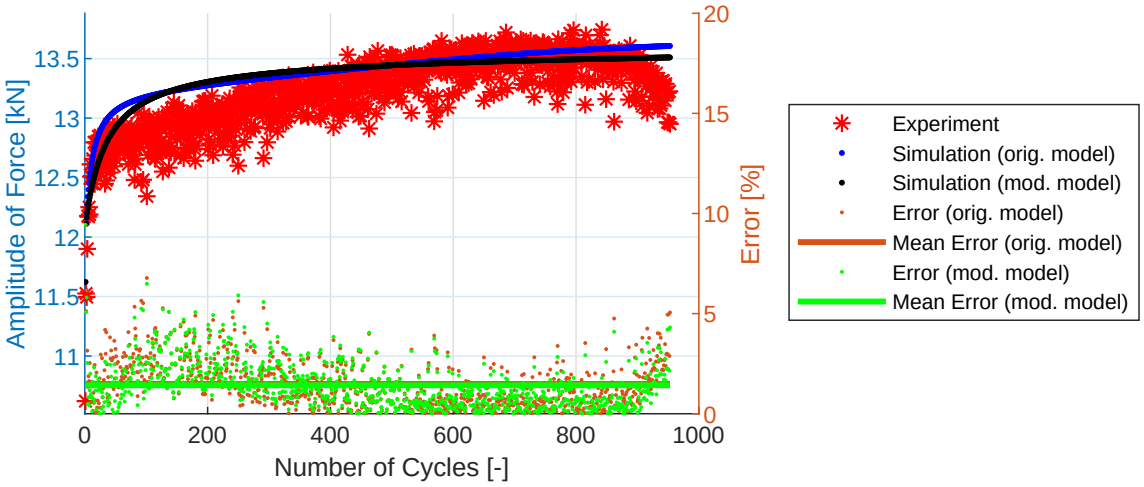

Figure B.60: Experiment vs. simulations, specimen R5-5.

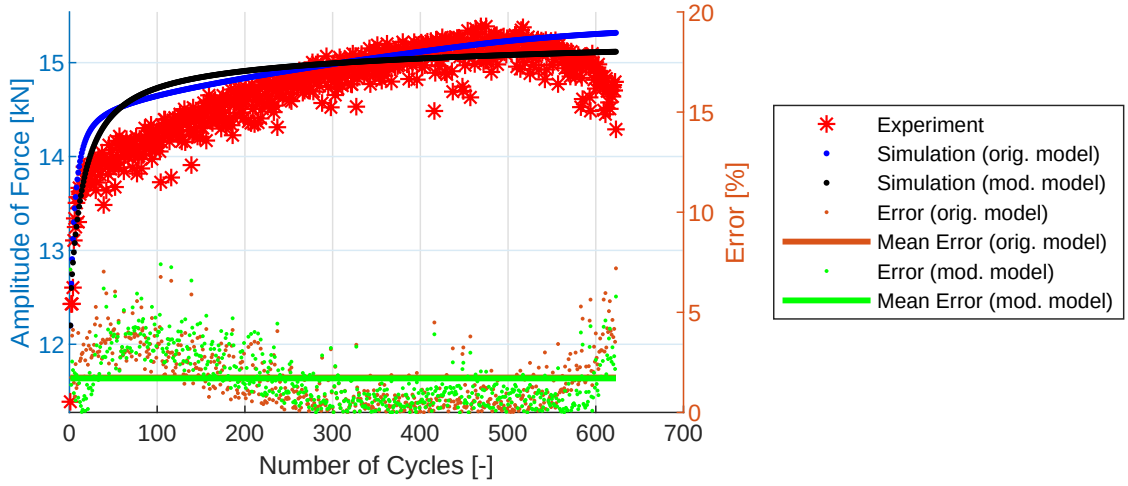

Figure B.61: Experiment vs. simulations, specimen R5-6.

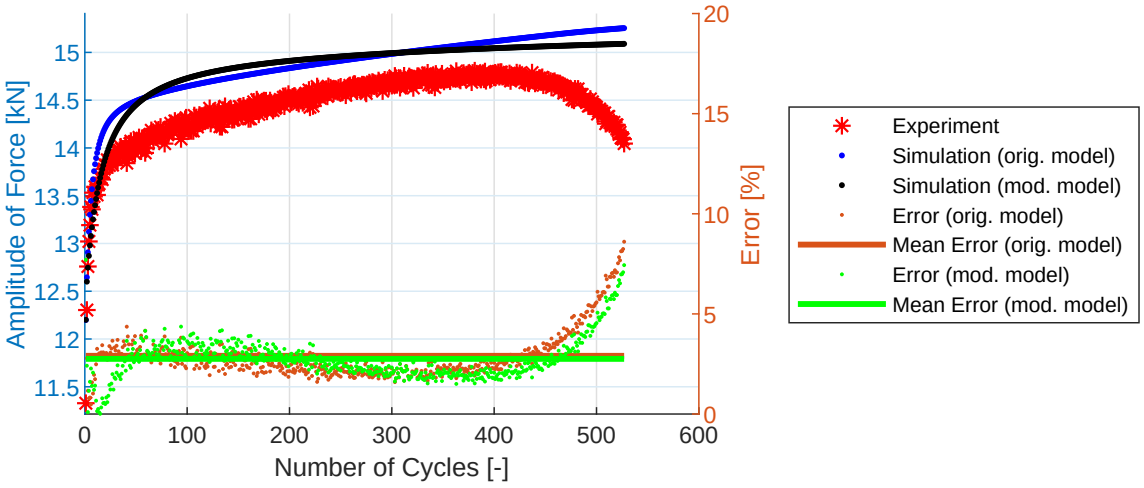

Figure B.62: Experiment vs. simulations, specimen R5-7.

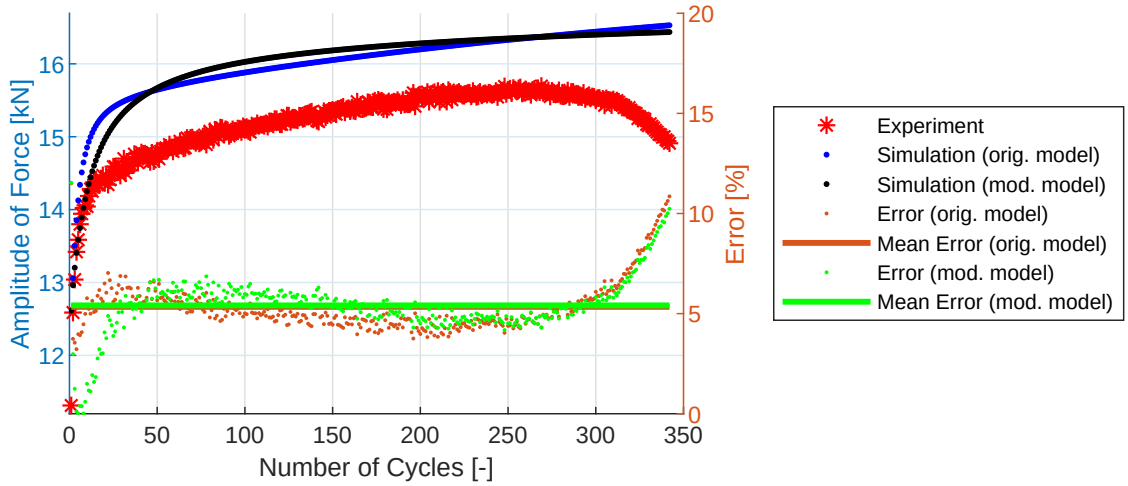

Figure B.63: Experiment vs. simulations, specimen R5-8.

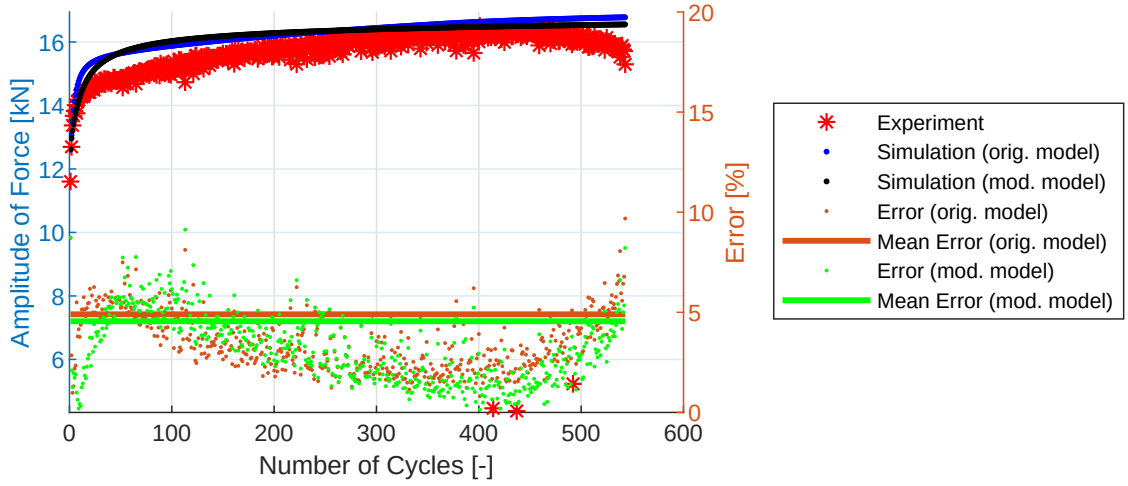

Figure B.64: Experiment vs. simulations, specimen R5-9.

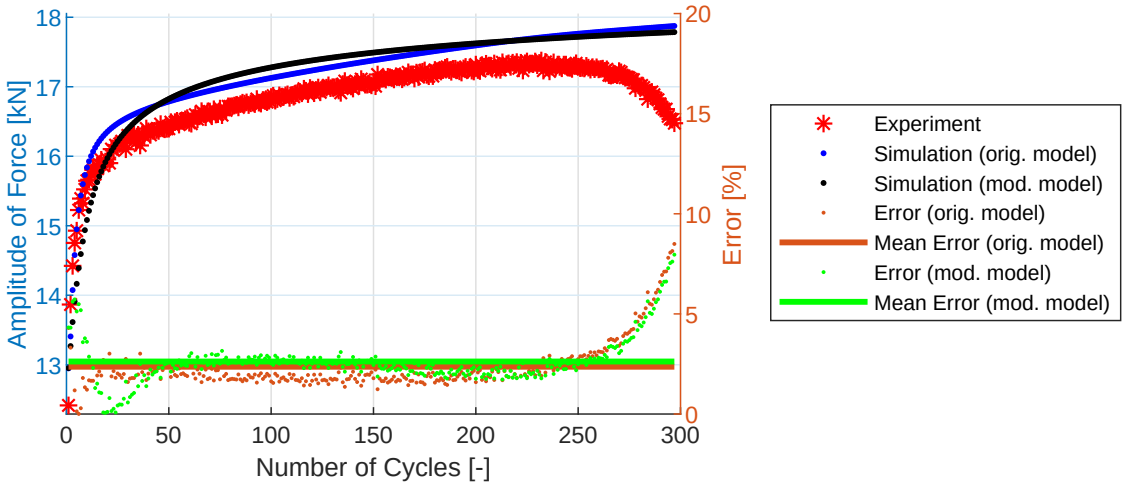

Figure B.65: Experiment vs. simulations, specimen R5-10.

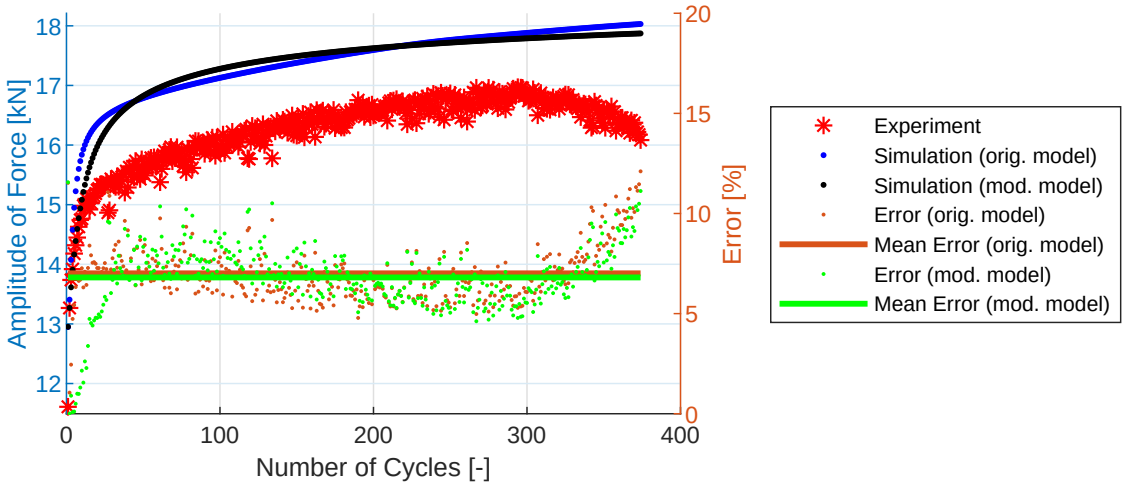

Figure B.66: Experiment vs. simulations, specimen R5-11.

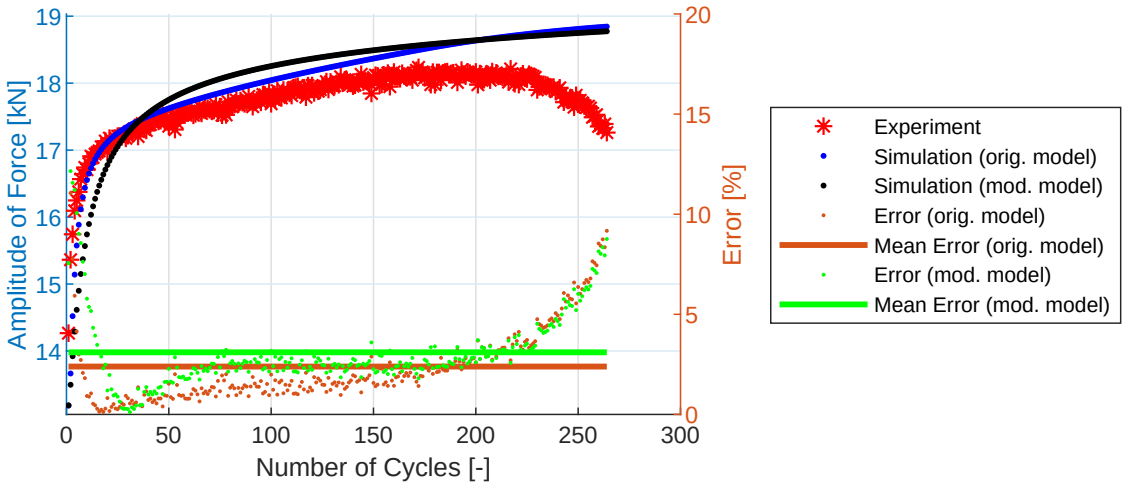

Figure B.67: Experiment vs. simulations, specimen R5-12.

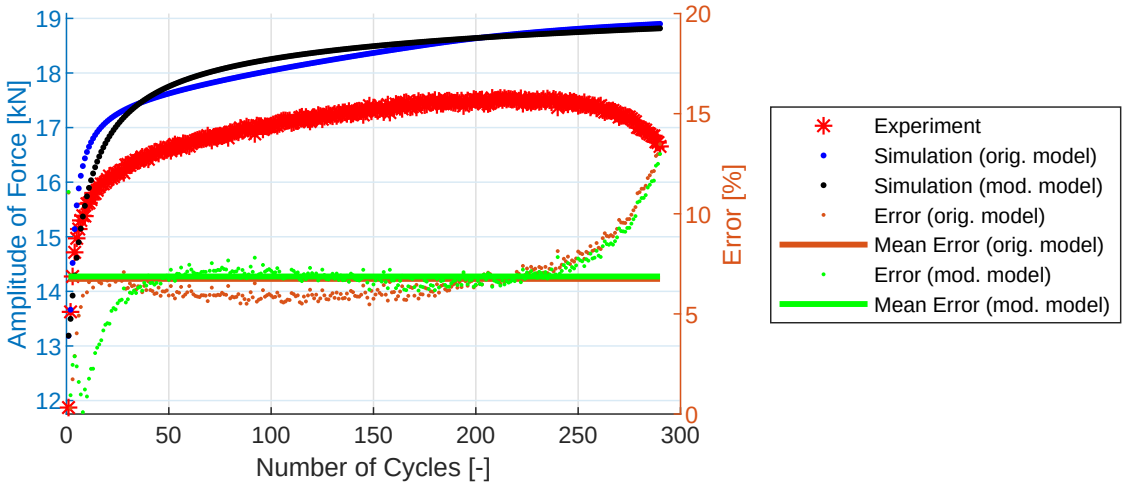

Figure B.68: Experiment vs. simulations, specimen R5-13.

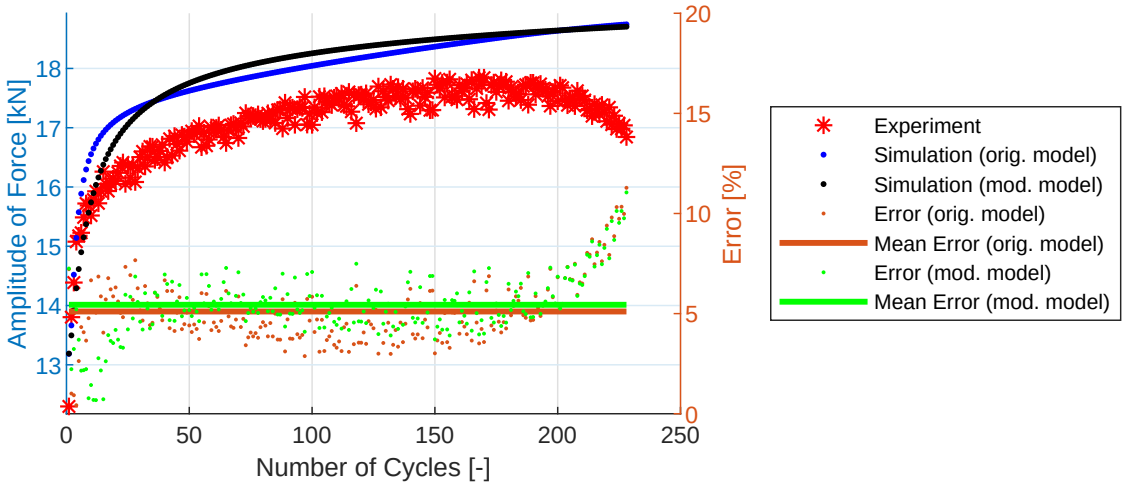

Figure B.69: Experiment vs. simulations, specimen R5-14.

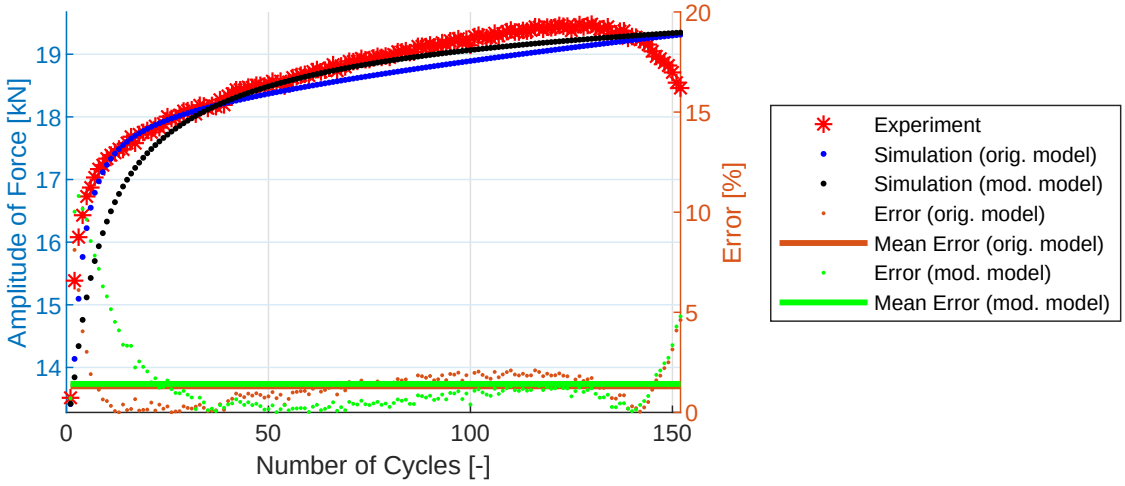

Figure B.70: Experiment vs. simulations, specimen R5-15.

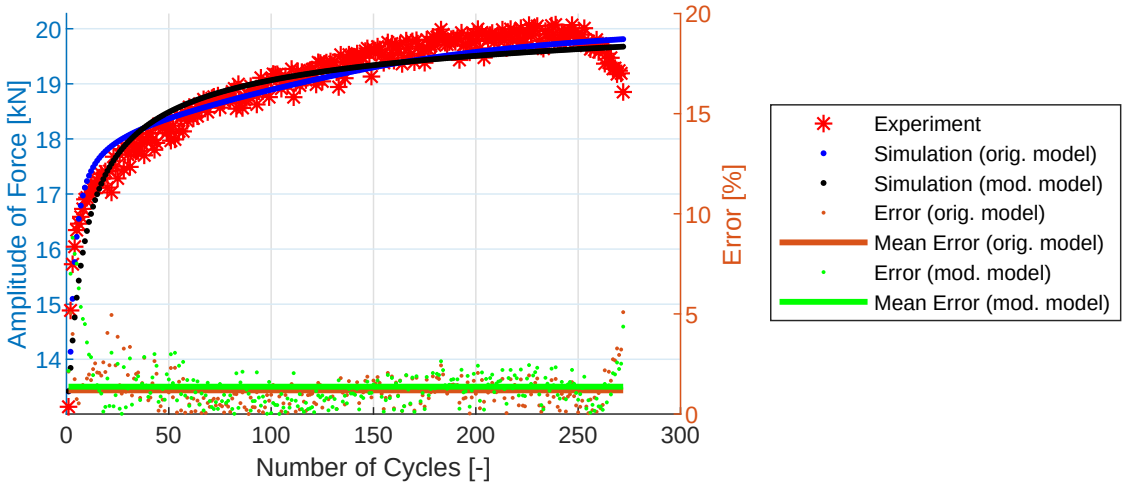

Figure B.71: Experiment vs. simulations, specimen R5-16.

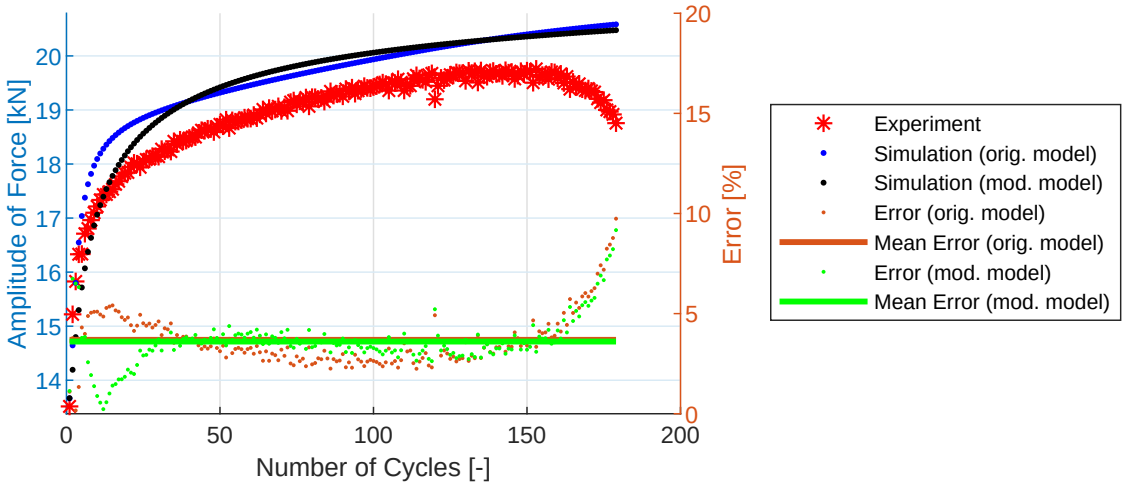

Figure B.72: Experiment vs. simulations, specimen R5-17.

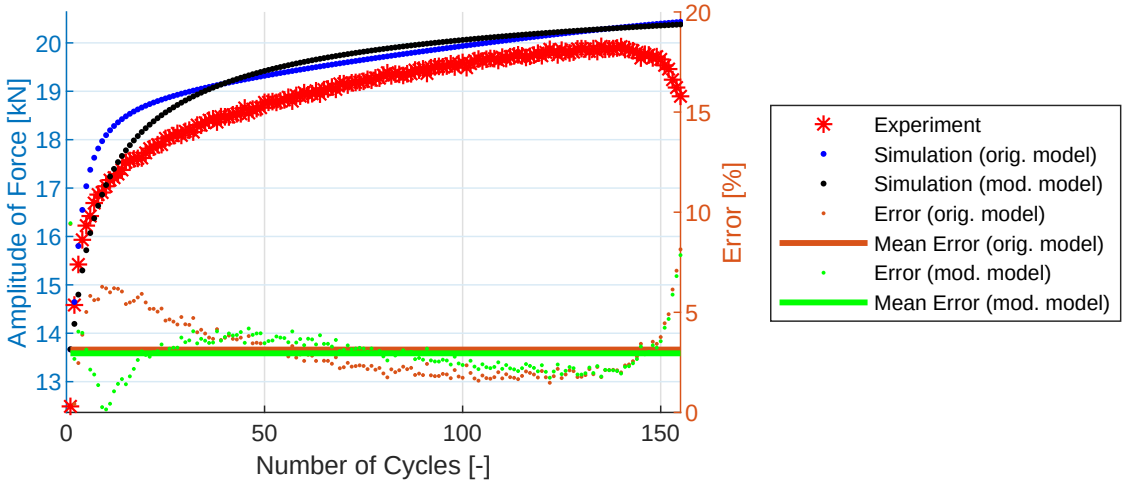

Figure B.73: Experiment vs. simulations, specimen R5-18.

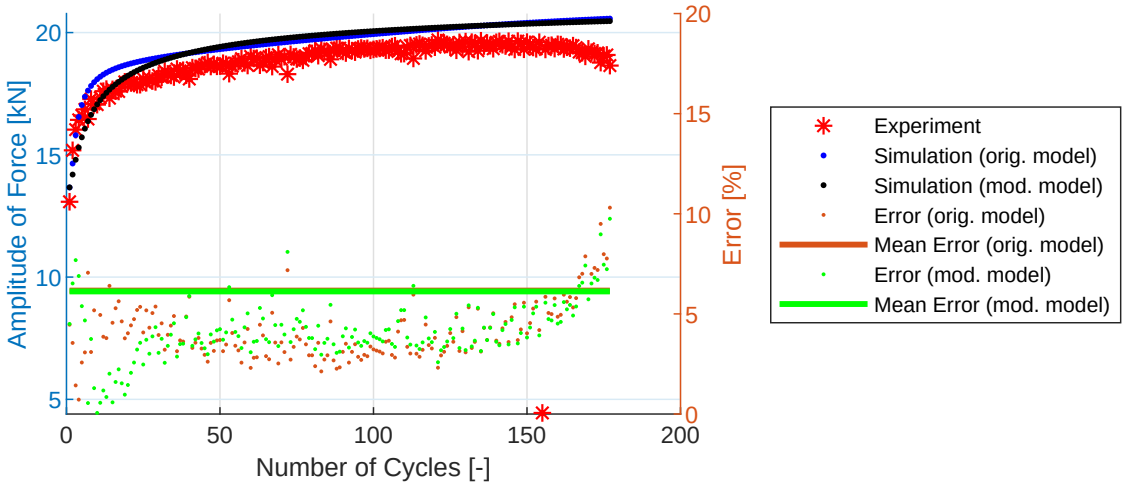

Figure B.74: Experiment vs. simulations, specimen R5-19.

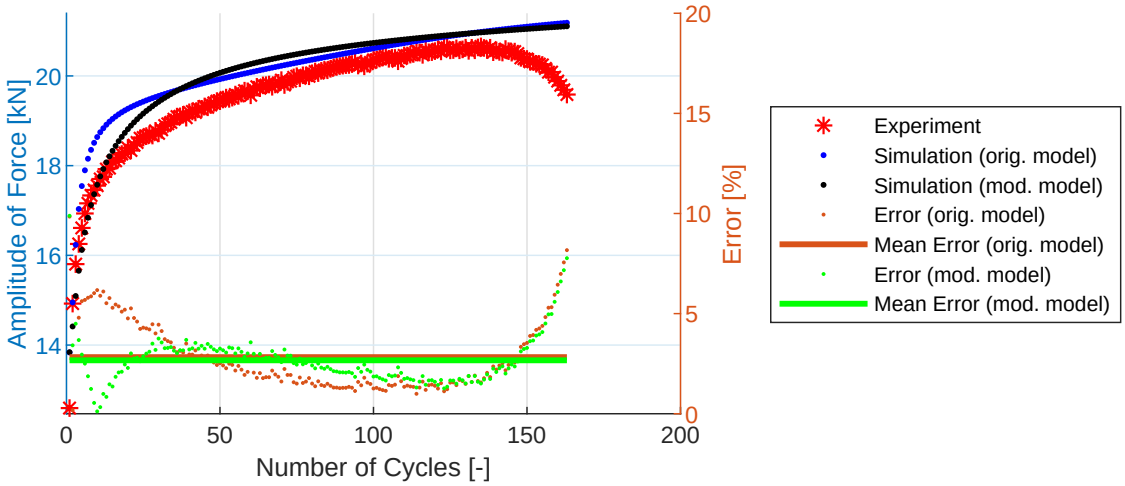

Figure B.75: Experiment vs. simulations, specimen R5-20.

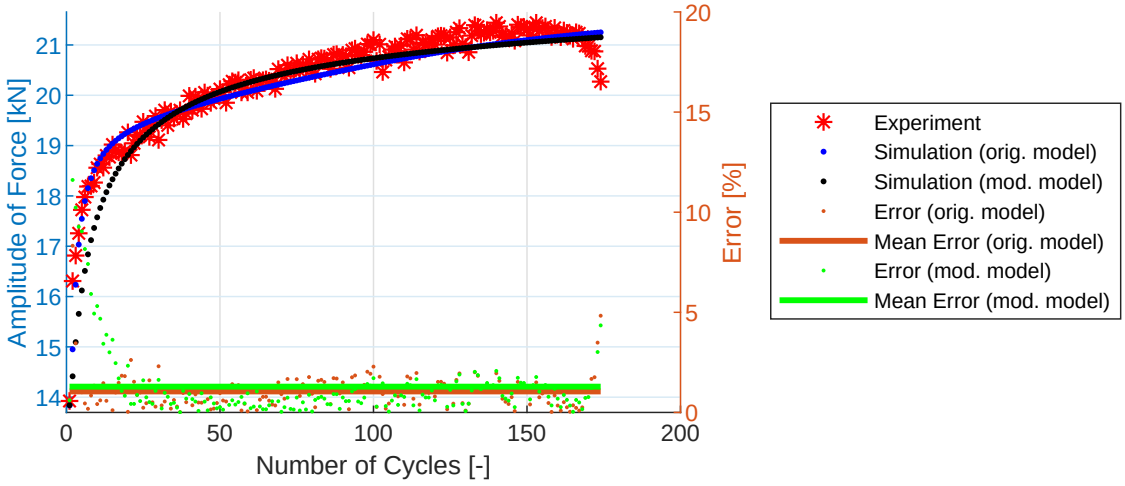

Figure B.76: Experiment vs. simulations, specimen R5-21.

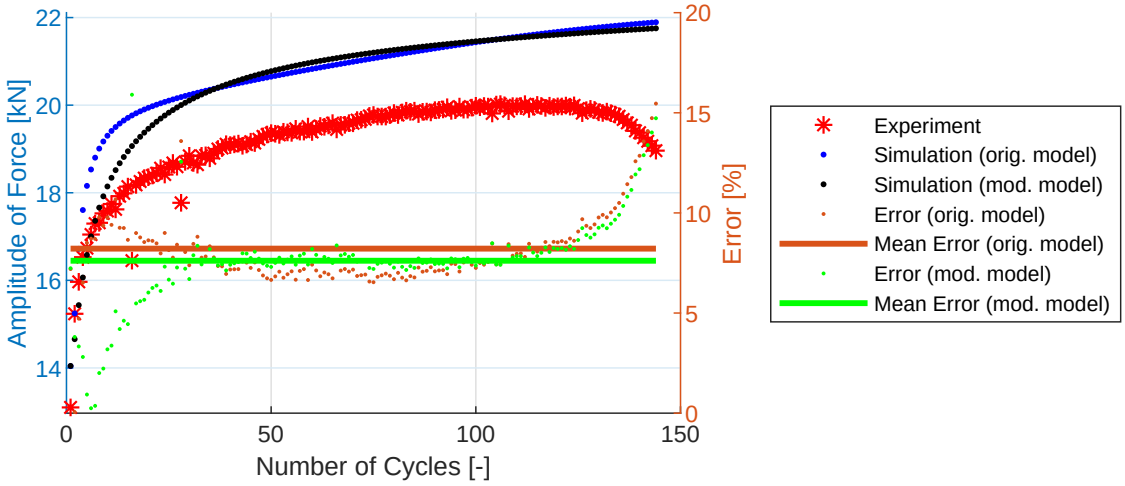

Figure B.77: Experiment vs. simulations, specimen R5-22.

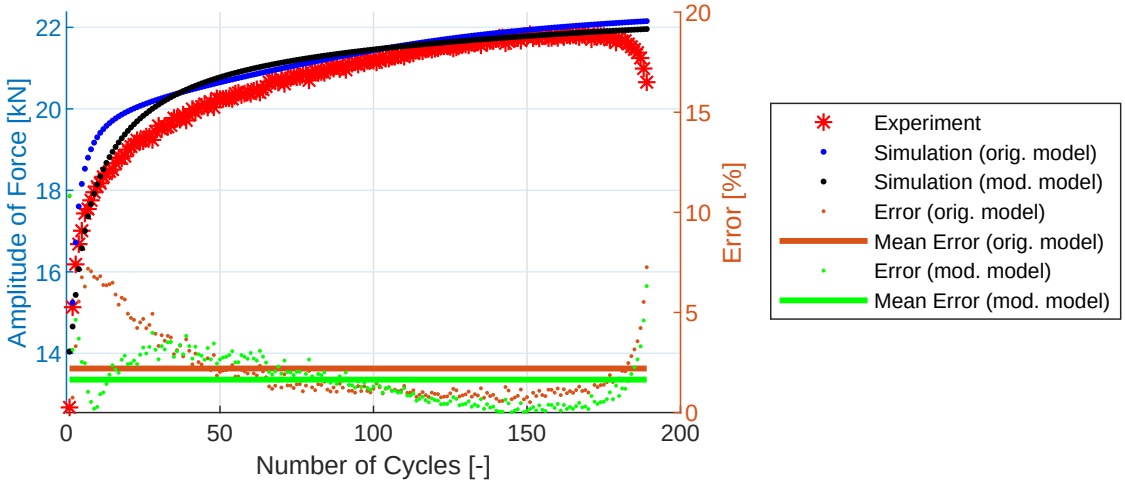

Figure B.78: Experiment vs. simulations, specimen R5-23.